Flow Visualization of Four-Inlet Ducted Rocket Engine Configurations

Christopher M. Brophy* and Clark W. Hawk†
Propulsion Research Center
Department of Mechanical and Aerospace Engineering
University of Alabama in Huntsville, Huntsville, AL 35899

ABSTRACT

A water flow visualization facility was constructed in order to investigate the mixing processes inside of four-inlet ducted rocket engines (DRE) with various flow rates and geometries. The observed flow fields were documented with video and conventional photography so that relationships between various geometric/flow parameters and the flow field behavior could be obtained. Flow visualization was achieved by seeding the flow field with polystyrene spheres and illuminating them with laser sheet lighting. Images revealed complex mixing patterns within the dome head region of the combustors which exhibited a strong dependence on dome height, momentum ratios, and inlet flow angles. For large inlet flow angles on the same-station combustors, it was shown that the geometries intrinsically direct a significant portion of the inlet flow towards the dome head region without the need for diverter devices. The resulting dome-region flow field contains two distinct recirculation patterns shown to be dependent on the momentum ratio and inlet flow inlet angle. These parameters also strongly affect the existence and strength of transport mechanisms between the fore and aft combustor segments. By designing a combustor accordingly, it may be possible to take advantage of one or both of the operating conditions resulting in a combustor with improved combustion properties.

Keywords: Water, Flow Visualization, Ducted Rocket Engine, Four Inlet, Side Dump Combustor, Momentum Ratio, Mass Ratio

*Graduate Research Assistant, Student Member AIAA
†Center Director and Professor, Senior Member AIAA

INTRODUCTION

Ducted rocket engine systems have recently received a revived interest due to their high specific impulse. throttlability. and suitability for long range applications. They obtain the high specific impulse by ducting the inlet flow in which they fly through inlet ducts and using it as the oxidizer which is mixed with a fuel rich gas from a gas generator. The mixture combusts and is then accelerated through a converging/diverging nozzle to generate thrust. A diagram showing the general layout of a DRE is shown in Figure 1. Much of the flow visualization work performed in the past has been with one and two-inlet geometries. These geometries offer an aerodynamic advantage since the inlet ducts may be tailored to generate lift for the vehicle but often require some type of inlet flow deflecting device to be installed in the ducts so that sufficient inlet flow enters the dome region of the combustor where the flameholding process typically occurs. These combustors have often been investigated using flow visualization with water for qualitative information and direct-connect hot-fire testing [Schadow and Chieze, 1981] for quantitative results.

The work described in this article has been performed on a facility constructed at The University of Alabama in Huntsville. This facility was used to study different mixing scenarios for four-inlet ducted rocket engine geometries through flow visualization with water flows simulating both the "fuel" flow and the "air inlet flow" flow. Four-inlet geometries offer advantages over the one and two-inlet geometries such as steer-to-turn capability and the tendency to passively divert necessary inlet flow into the dome region of the combustors for

flameholding requirements without the use of diverter devices commonly needed on other combustors. The effects of inlet flow angle, dump station, air/fuel mass ratios, air/fuel momentum ratios, dome height, and injector performance were investigated over a wide operational range. The wide range allowed the investigation of flame holding and performance potential of the various geometries over a large number of operating conditions.

FACILITY DESCRIPTION

The flow visualization facility (Figure 2) has overall dimensions of 6.1 meters by 4.6 meters. Not shown in the figure are the 3800 liter reservoir tank and the centrifugal pump located below the deck. The power plant for the facility is a 22.4 kW variable RPM centrifugal pump capable of delivering 3000 liters per minute at 207 kPa to the combustor model. This pump was dedicated to delivering high volume at low pressure and was used to supply water as the "air" source for the combustor. A supplemental 517 kPa water supply arm was used to deliver the water for the "fuel" source at up to 132 liters per minute. The amount of water delivered to the model was controlled both by the pump RPM and by throttling the supply arms with globe valves. A PC monitored Blancett 401 flowmeters used on each arm, two pressure transducers, and provided remote pump control if desired. The combustor models were placed inside a 0.92m x 1.00m x 0.60m viewing tank which contained water to minimize refraction effects.

The dome head (Figure 3) is a concave piston head with O-rings that contains the fuel injector and which allows positioning at any axial location in the front end of the combustors. The dome height is defined as the axial distance between the beginning of the inlet flow dump station and the perimeter of the dome head. A five orifice injector was used, one axial orifice and four off-axis orifices angle at 45 degrees to the combustor axis. See figure 3 for injector dimensions.

Visualization of the flow field was achieved by seeding the reservoir tank with 0.0254 cm (0.010") polystyrene spheres. The fuel jet was left unseeded. "Outgassing" of air in the "fuel" supply after experiencing the pressure drop across the injector resulted in a mist of tiny inlet flow bubbles which provided excellent visualization of the fuel flow. A 5 watt Argon Ion laser was used to illuminate the flow field. The laser output was first focused and then expanded through a cylindrical lens to produce a light sheet approximately 1.0 mm thick. The sheet was capable of being oriented either vertically or horizontally. The images observed were then captured on Hi8 video and by conventional photography. Figure 4 is a sample photograph of a 45 degree same-station combustor test and is the flow field depicted in Figure 12.

RESULTS AND DISCUSSION

Six combustors have been evaluated (Figure 5). Three of the combustors had the inlet flow inlets at the same axial station. The remaining three had one pinlet flow of inlet flow inlets staggered 1.5 inlet diameters downstream of the upstream pinlet flow. The three six-inch I.D. combustors of each group consisted of 45, 60, and 90 degree inlet flow inlet arm dump angles each with an internal diameter of 3.81 cm. All were investigated up to a Reynolds number of 5.5 x 10^5, but no Reynolds number effects were observed above Reynolds numbers of 1.5 x 10^4. The mass flow ratio ($\dot{m}_a / \dot{m}_f$) and momentum ratio ($\dot{m}_a v_a / \dot{m}_f v_f$) were varied between 10 to 60 and 0.43 to 2.58 respectively.

Dome Height

Dome height was the first parameter investigated. The first combustor tested was the 90 degree same-station combustor. A dome height of 0.25D (3.81 cm) resulted in symmetric, stable

recirculation regions for the 90° same-station combustor over a wide range of momentum ratios and appeared to be the preferred height for that combustor and the fuel injector used based on the size and strength of the recirculation zones. The preferred height was determined after testing each dome height setting over the range of momentum ratios specified earlier. Figure 6 shows the operating zones for momentum ratio versus dome height. The preferred dome height was then chosen as the height which minimized the fluctuating behavior between the impinging and passive recirculation regimes (to be discussed next). Dome heights greater than 0.27D resulted in the fuel jets impinged on the combustor wall and not the incoming inlet flow columns. The preferred dome height for the 60° same-station combustor was determined to be ≈0.083D (1.27 cm) by the same manner. An acceptable dome height for the 45° combustor was not found, so a dome height of 0 cm was used in order to provide the strongest recirculation possible. The alternating-station combustors did have problems with two of the fuel jets impinging on the wall because the same fuel injector was used on all models. This situation is discussed further in the alternating-combustor section.

Same-Station Combustors

The 90 degree same-station combustor was investigated first with a low "fuel" flow rate. The flow field contained symmetric counter-rotating zones on both sides of the inlet flow inlet station for plane A-A. The recirculation zones increased in strength as the "inlet flow" flow rate increase, but the downstream zone appeared to fluctuate in size and shape. Figure 7 shows the orientation of the sheet lighting relative to the combustor. Figure 8 shows the pairing of two counter-rotating regions found between each of the inlet arms for plane B-B. These regions appeared to be tube-like and were seen to contain substantial amounts of "fuel". The endpoints of the tube could not be

isolated. but appeared to begin in the dome head region and terminate approximately 1.0 inlet diameter downstream from the inlet flow inlet station. The structures seen in the flow field did not appear to develop further for Reynolds numbers above 5.5×10^4, but fluctuations in size and shape were observed.

The low "fuel" flow rate resulted in a momentum ratio of 2.39. For the high momentum ratios, the fuel jet was seen to "bend back" and follow the governing "inlet flow" flow (Figure 9). This was termed a "passive" flameholding scenario. There was no significant change in this flow field until a momentum ratio between 1.90 and 1.61 was reached. In this range, the fuel jet(s) fluctuated between the "passive" scenario and a straight fuel jet, termed "impinging" (Figure 10), which impinged on the incoming "inlet flow" column. Below a momentum ratio of 1.61, the fuel jet would partially penetrate the inlet flow column and then bifurcate into two branches. One would be deflected towards the wall and the other towards the stagnation point of the four jets. The result was two recirculation zones split and driven by the fuel jet.

The 60 degree combustor was investigated at a dome height setting of 0.083D and over the same momentum ratio range. The recirculation regimes observed near the dome head on the 90 degree combustor also occurred in the 60 degree combustor but were seen to transition at a higher momentum ratio. The "passive" regime (Figure 11) existed down to a momentum ratio of 2.05, fluctuated in the range between 2.05 and 1.72, and became "impinging" below 1.72 (Figure 12). The critical momentum ratio values are defined as the value at which the fuel jet transitions from passive to impinging. This was taken as the center value in the fluctuating region. The critical momentum ratios for the 60 and 90 degree combustors are shown to be similar when the only lateral momentum component of the "inlet flows" were compared.

The downstream recirculation regions and reattachment lengths remained relatively constant over the momentum ratio range investigated. but did reduce in size once the center fuel jet penetrated the stagnation point of the four inlet flow columns. The transport "tubes" existing in between the "inlet flow" inlet arms appeared to be weaker and shorter in length than observed in the 90 degree combustor. No fuel accumulation in the dome head region was observed for this combustor, indicating that the transport mechanisms were indeed functioning.

The 45 degree same-station combustor exhibited the weakest recirculation zones. This was likely due to the reduced amount of inlet flow momentum normal to the combustor axis which was seen to produce much of the mixing and transport that occurs between the "fuel" and "air inlet flow" jets. The center fuel jet was seen to penetrate the "inlet flow" jets easily while the fuel from the four off-axis jets seemed to accumulate in the dome head region. The flow field did not change significantly over the entire momentum ratio range (Figure 13). The transport "tube" mechanisms existing in between the inlet arms for the 60 and 90 degree combustors could not be located for the 45 degree combustor.

Alternating-Station Combustors

The stagger-station combustors generated a very different flow field compared to the same-station models. The investigation began with the 90 degree combustor. The "inlet flow" and "fuel" flow rates were varied as in the same-station combustor runs. The dome heights were fixed at 0.2D so that two of the fuel jets would impinge on two of the "inlet flow" columns effectively. The result was that the other two fuel jets would impinge directly onto the wall of the combustor. Since this behavior would increase wall erosion greatly, it was seen that an alternate injector would have to be fabricated for further investigation of the alternating-station

combustors. The impingement point of the two upstream inlet flow columns resulted in a "fanning" effect. A portion of this fanning of the upstream jets would then divert the downstream jets further downstream. The fanning effect witnessed on all alternating-station combustors. Since two of the "fuel" jets impinged on the model wall for these configurations and the level of mixing appeared low. further testing was not performed.

The low level of mixing and "fuel" transport with these configurations was believed to be due to the absence of the transport tube mechanisms seen in the same-station combustors.

CONCLUSIONS

The flow fields observed in the four-inlet geometries have the intrinsic characteristic of diverting a substantial amount of the inlet flow into the dome region of the combustors resulting in two recirculation regions. Characteristics of the recirculation patterns and geometrical limitations resulted in preferred dome heights of 0.25D, 0.083D, and 0 for the 90, 60 , and 45 degree same-station combustors respectively.

The 90° same-station combustor contained strong and stable recirculation zones both upstream and downstream of the inlet flow inlet locations. The upstream recirculation zone interacted with the off-axis fuel jets in two distinct patterns. It was seen that above a critical momentum ratio, the fuel jet "bent backwards" and followed a pattern dictated by the "inlet flow" flow resulting in one primary recirculation zone per jet. Once the momentum ratio was lowered below a critical momentum ratio, the same fuel jet impinged and penetrated the incoming inlet flow column resulting in two counter-rotating recirculation zones located on either side of the fuel jets. In between each of the "inlet flow" inlet columns existed two counter-rotating tubes aligned with the

combustor axis. These tubes were believed to be the primary transport mechanisms responsible for transferring the dome region products to the aft combustor chamber.

The 60 degree same-station combustor contained similar flow structures as seen in the 90 degree same-station combustor. but they were observed to be less organized and weaker in strength. The dome height for the 60 degree combustor was reduced to 0.083D in order to maintain strong recirculation zones in the dome head region. The axially aligned transfer tubes were not easily located. but effects of the transfer mechanisms were seen.

None of the 45 degree same-station combustors generated a favorable flow field. The shallow inlet flow-inlet angle resulted in directing most of the "inlet flow" momentum downstream, thereby greatly reducing the amount of mixing which occurred. This produced a fuel-rich dome head region. After viewing the three same-station combustors, it was concluded that the strength and organization of the recirculation regions and tubes were highly dependent upon the amount of momentum directed normal to the combustor axis. Therefore it is recommended that only inlet flow inlet angles of 60 degrees or greater be given further consideration.

Although actual combustor performance cannot be determined from flow visualization studies, it is likely that the conclusions reached from the observed flow fields will be applicable in designing a combustor with favorable combustion characteristics.

ACKNOWLEDGEMENTS

NOMENCLATURE

D   = combustor model diameter

$\overline{U}$ = mean combustor flow velocity

h   = dome height

x   = axial location along combustor

$\dot{m}_a$ = mass flow of air

$\dot{m}_f$ = mass flow of fuel

$\dot{m}_a v_a$ = momentum of air

$\dot{m}_f v_f$ = momentum of fuel

Re_D = Reynolds number, UD/υ

υ = Kinematic viscosity

REFERENCES

Chittilapilly, L.T., Venkateswaran, S., 1990. Flow Measurements in a Model Ramjet Secondary Combustion Chamber, *Journal of Propulsion*, Vol. 6, No. 6, pp. 727-731.

Hsieh, W.H., Yang, V., 1989. Measurement of flowfield in a simulated solid-propellant ducted rocket combustor using laser Doppler velocimetry, *25th Joint Propulsion Conference*, AIAA Paper No. 89-2789.

Kennedy, J.B., 1974. Ramburner Flow Visualization Studies, *11th JANNEF Meeting*, CPIA Publication Number 261, pp. 415-440.

Reuter, D.M., Hegde, U.G., and Zinn, B.T., 1990. Flowfield Measurment in an Unstable Ramjet Burner, *Journal of Propulsion*, Vol. 6, No. 6, pp. 680-685.

Schadow. K.C.. Chieze. D.J., 1981. Water Tunnel and Windowed Combustion as Tools For

Ducted Rocket   Development. Vol. 2. *JANNEF Propulsion Mtg*, pp. 101-115.

Schetz. J.A., Hewitt, P.W., and Thomas. R., 1983. Swirl Combustor Flow Visualization Studies

in a Water Tunnel, *Journal of Spacecraft*, Vol. 20, No. 6, pp. 574-582.

Universal Energy Systems. Inc., 1983. Multi-Ducted Inlet Combustor Research and

Development, *Interim Report for Period September 1982 - August 1983*, AFWAL-TR-83-2081.

Vanka. S.P., Craig, R.R., and Stull, F.D., 1984. Mixing, Chemical Reaction, and Flow Field
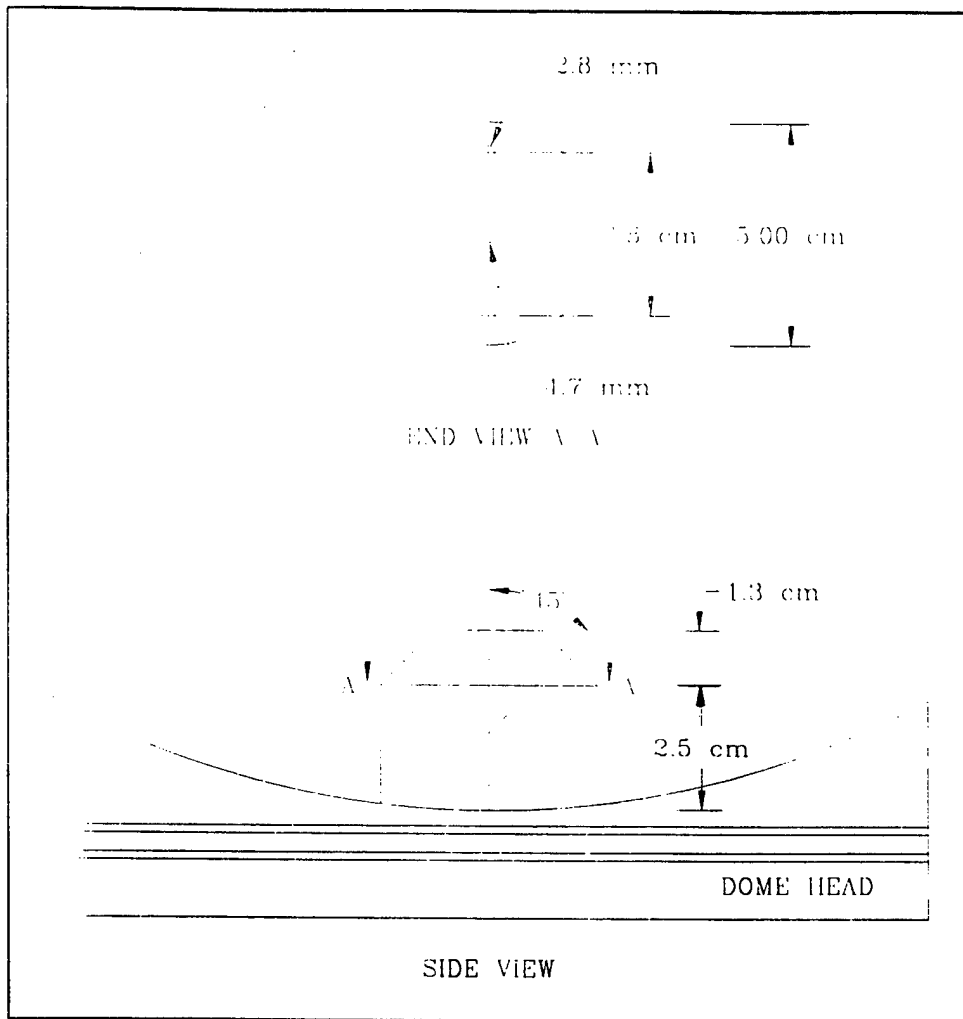
Development in Ducted Rockets, *Progress Report*

Winter. E.F. , 1951. Flow Visualisation Techniques Applied to Combustion Problems, *Journal of*

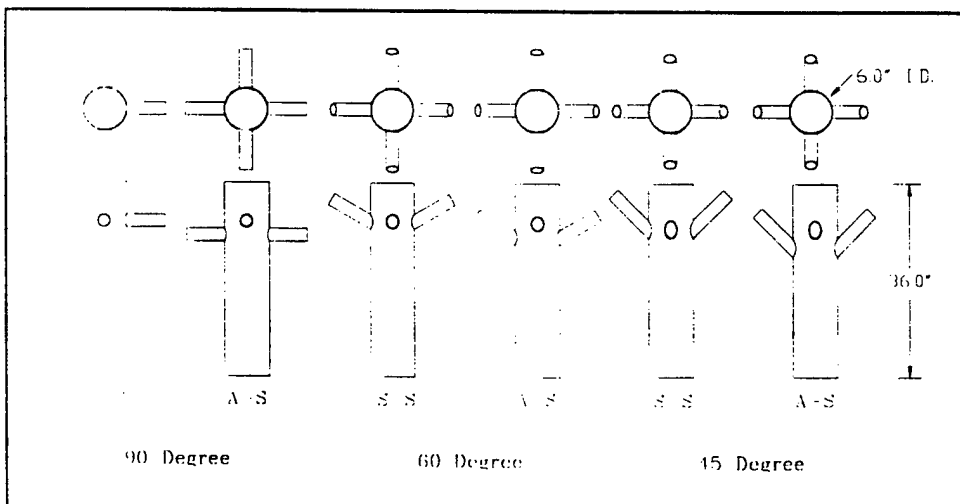*the Royal Aeronautical Society*, Vol. 62, pp. 268-276.
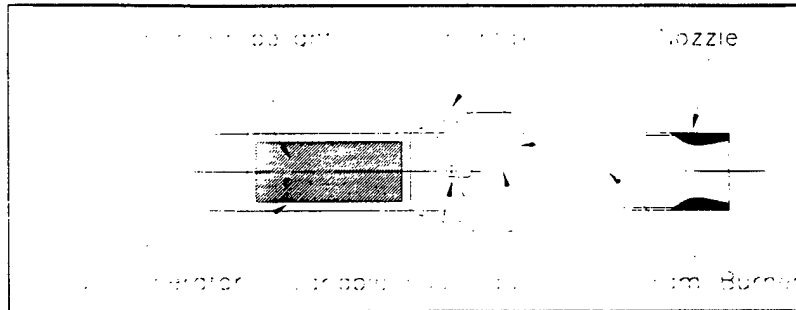
Figure 1: A ducted rocket engine schematic
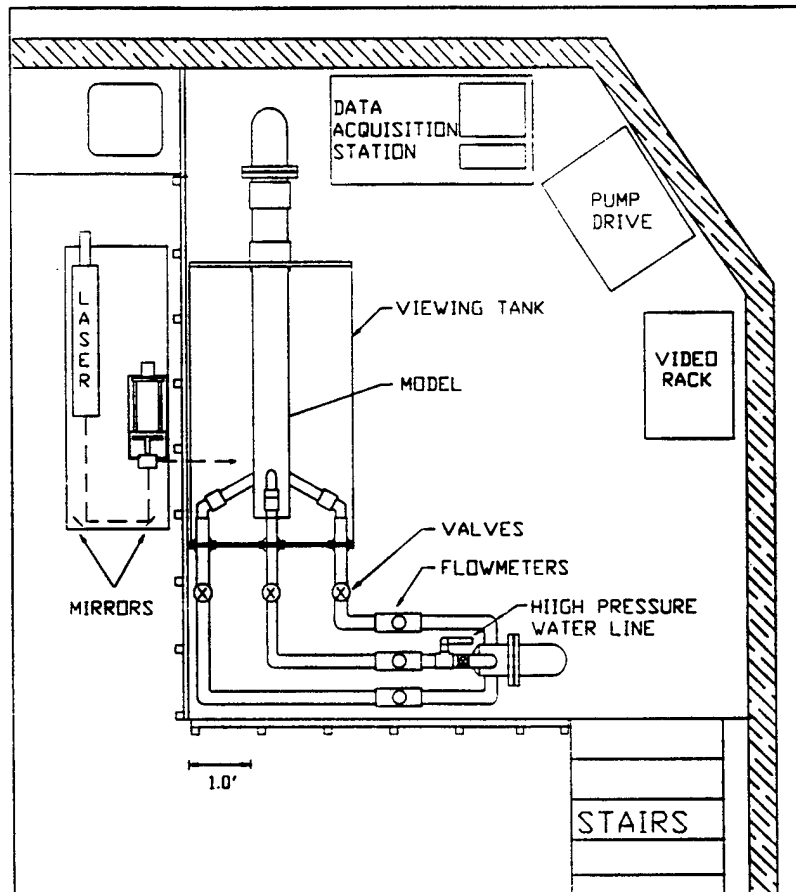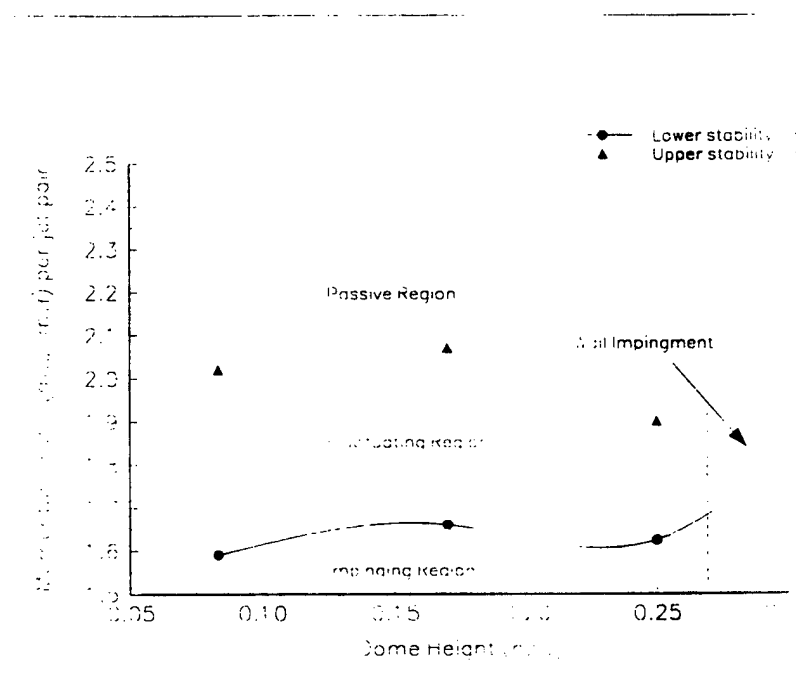

Figure 2: Flow Visualization Facility
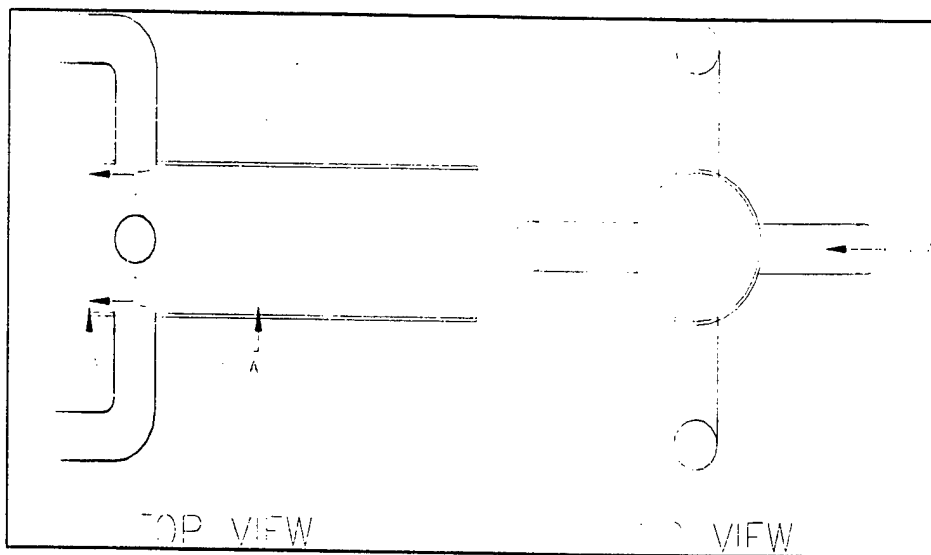
Figure 3: "Fuel" injector used in study

Figure 4: Model Combustors Used
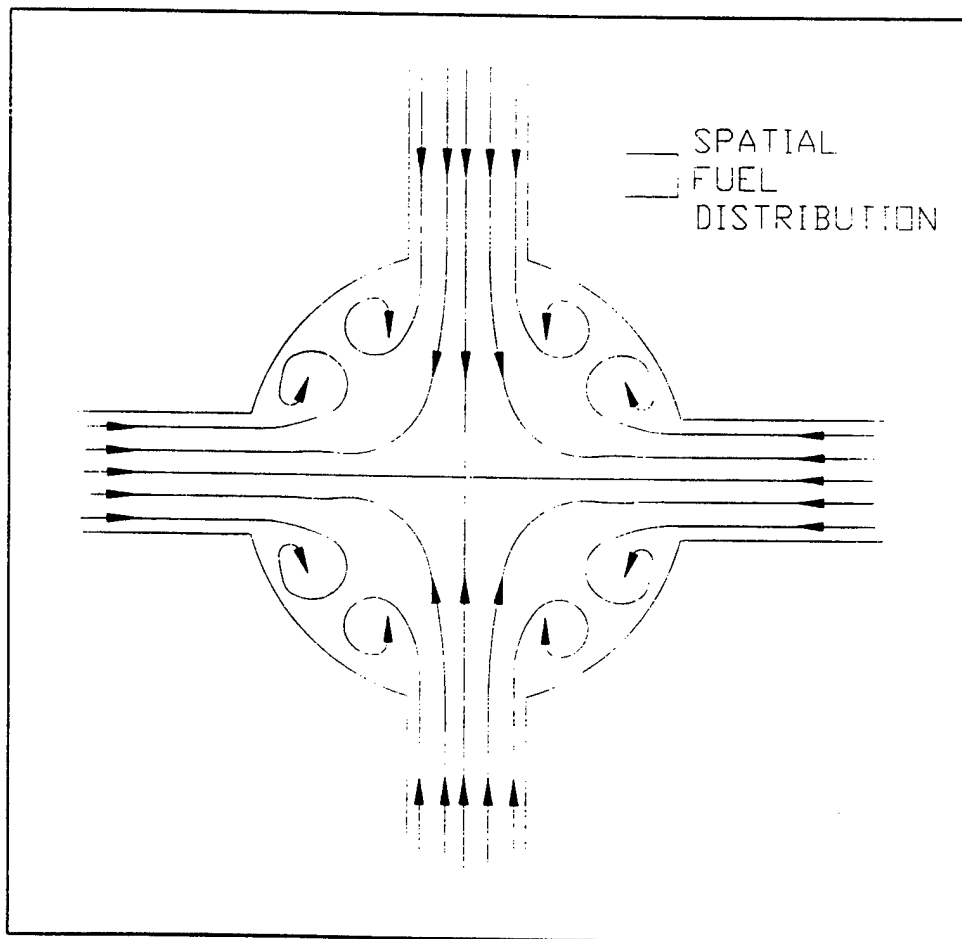
will be scanned.

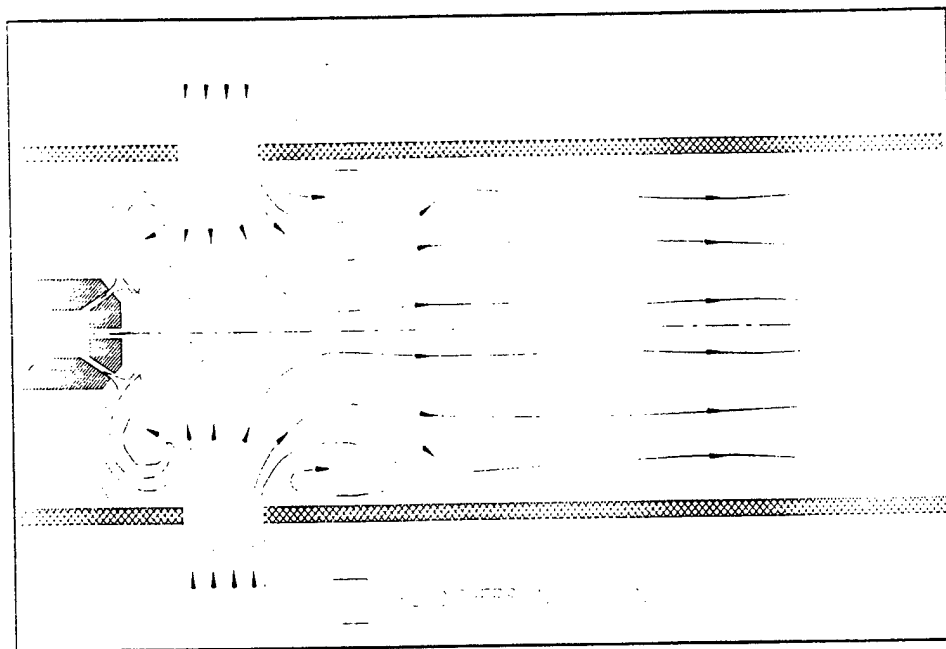**Figure 5: 45 Degree Same-Station combustor test**

Figure 6: Recirculation regimes for 90 degree Same-Station combustor

Figure 7: Laser Sheet Orientation

SPATIAL
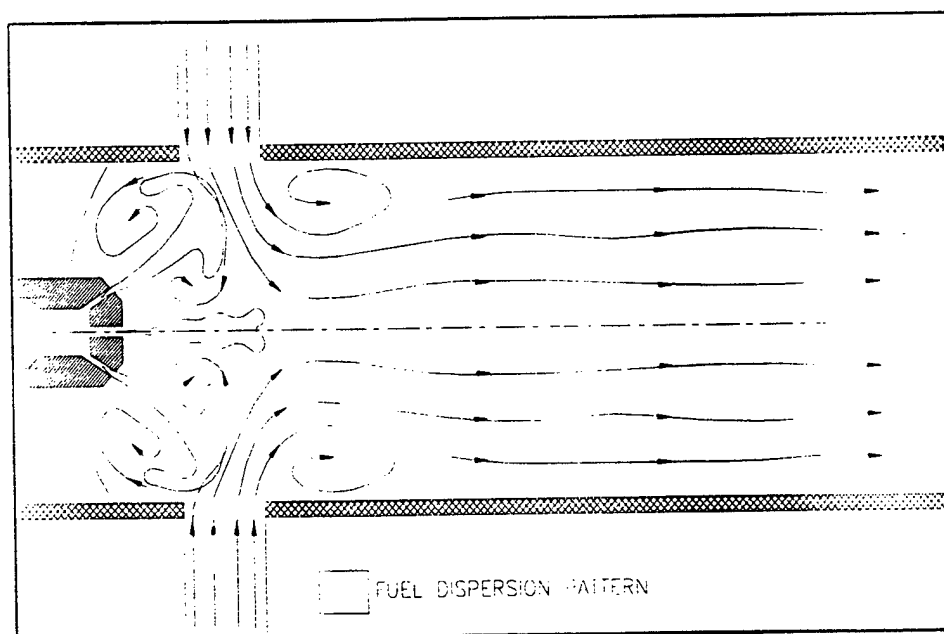FUEL
DISTRIBUTION

Figure 8: View B-B of 90° same-station combustor

Figure 9: View A-A of 90° same-station combustor

FUEL DISPERSION PATTERN

Figure 10: View A-A of 90° same-station combustor
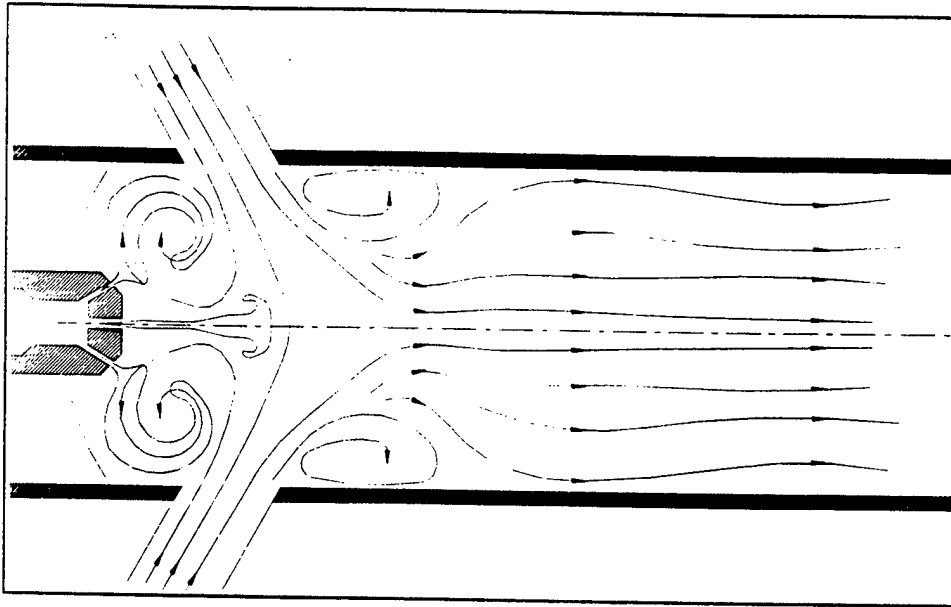
Figure 11: Observed streamlines in 60° combustor.

=FUEL DISPERSION PATTERN
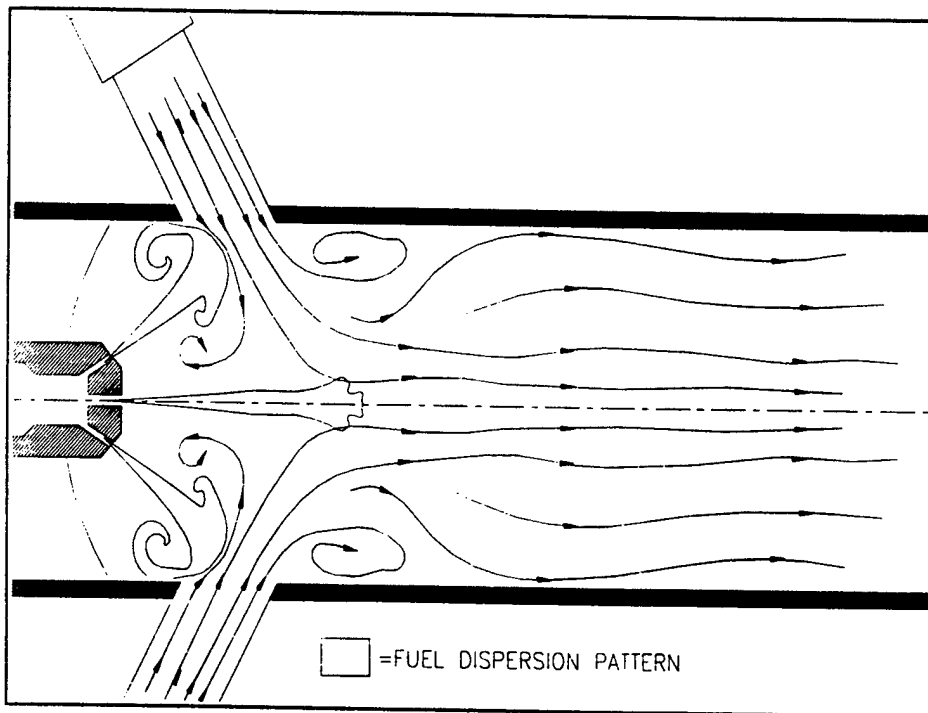
Figure 12: View A-A of 60° same-station combustor
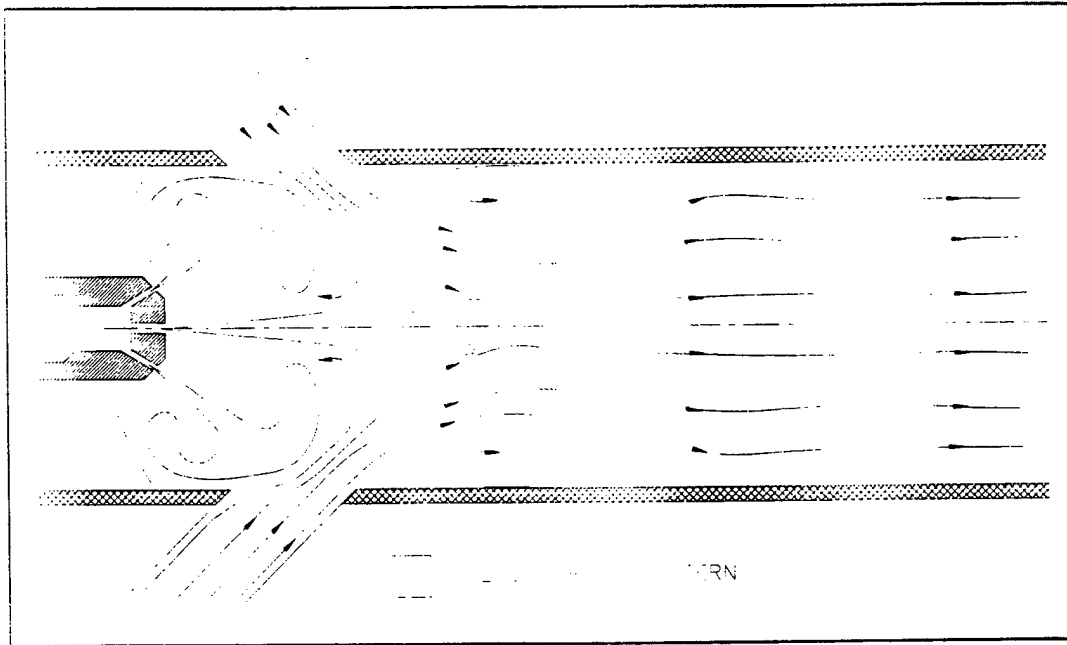
Figure 13: View A-A of 45° same-station combustor

AN INVESTIGATION OF FOUR-INLET DUCTED ROCKET ENGINE FLAMEHOLDER FUEL DISTRIBUTIONS

by

Christopher M. Brophy and Clark W. Hawk
Propulsion Research Center
Department of Mechanical and Aerospace Engineering
RI Building, E-27
University of Alabama in Huntsville
Huntsville, Alabama 35899
phone: (205) 890-7200
fax: (205) 890-7205

February 14, 1998

AN INVESTIGATION OF FOUR-INLET DUCTED ROCKET ENGINE FLAMEHOLDER FUEL DISTRIBUTIONS

Christopher M. Brophy[*] and Clark W. Hawk[†]

Propulsion Research Center
Department of Mechanical and Aerospace Engineering
University of Alabama in Huntsville, Huntsville, AL 35899

Abstract

Fuel concentrations existing in the flameholding region of a four-inlet ducted rocket engine with a five-orifice showerhead fuel injector are presented for a range of flow rates and fuel injector orientations. Methane was used as the fuel simulant and vibrational-Raman spectroscopy was used to image the methane distribution in the dome head region of an optically accessible four-inlet combustor. A fuel injector orientation which produced a fuel distribution and internal flowfield desensitized to the air/fuel momentum ratio was found.

Observations made during the gas-gas mixing study agreed well with conclusions from previous water flow visualization studies which investigated the internal flow fields of similar fuel injector orientations and combustor geometries.

Nomenclature

|	
D	Internal Diameter of Combustor
L	Length of Main Combustor
f	Fuel Mass Fraction
m_a	Air Mass Flow Rate
m_f	Air Mass Flow Rate
v_a	Air Injection Velocity
v_f	Fuel Injection Velocity
θ	Air Inlet Arm Angle

---

[*] Graduate Research Assistant
   Currently at the Naval Postgraduate School as a NRC Postdoctoral Associate
[†] Center Director and Professor

Introduction

Ducted rocket engine (DRE) systems have recently received a revived interest due to their high specific impulse, throttlability, and suitability for long range applications. They obtain high specific impulse by inducting the air through which they fly through inlet ducts and using it as the oxidizer which is mixed with liquid fuel or fuel rich gas from a gas generator. The mixture combusts and is then accelerated through a converging/diverging nozzle to generate thrust. A diagram showing the general layout of a DRE is shown in Figure 1. Much of the work performed in the past has been concentrated on one- and two-inlet geometries. These geometries offer an aerodynamic advantage since the inlet ducts may be tailored to generate lift for the vehicle but often require some type of inlet flow deflecting device to be installed in the ducts so that sufficient inlet flow enters the dome region of the combustor where the flameholding process typically occurs. The complex internal flow fields of these combustors have often been investigated using both flow visualization with water for qualitative information [Kennedy, 1974] and direct-connect hot-fire testing for quantitative results [Schadow, et al. 1981].

Four-inlet geometries offer advantages over the one and two-inlet geometries such as steer-to-turn capability where the vehicle may turn in any direction while keeping at least two air inlet arms exposed to the windward side in order to maintain combustor pressure. One- and two-inlet geometries must bank-to-turn in order to accomplish the same task. The four-inlet geometry also presents the potential to passively divert sufficient inlet flow into the dome region of the combustors to satisfy flameholding requirements without the use of active diverter devices commonly needed on other combustors, thereby potentially increasing the total pressure recovery and improving performance.
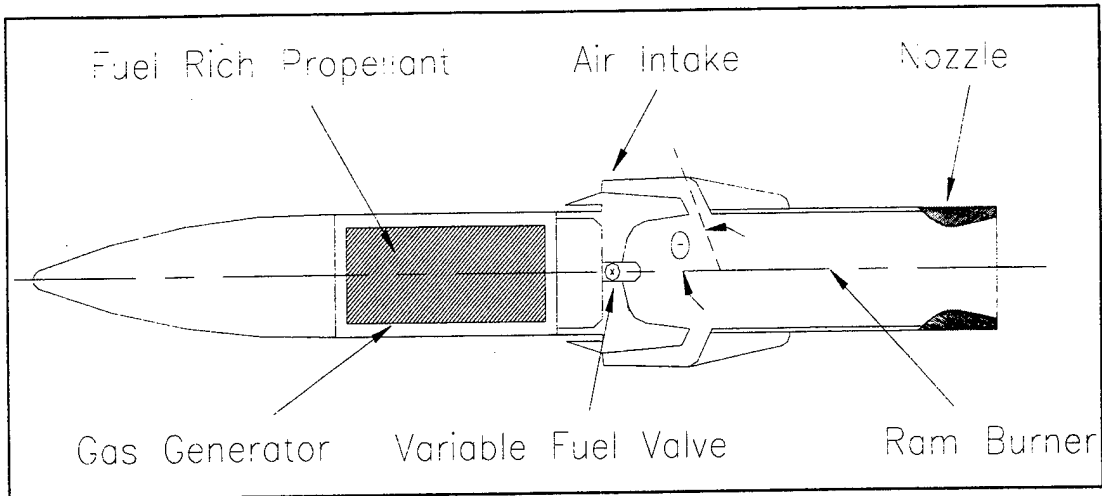
Figure 1: A Solid-Fuel Ducted Rocket Engine Schematic
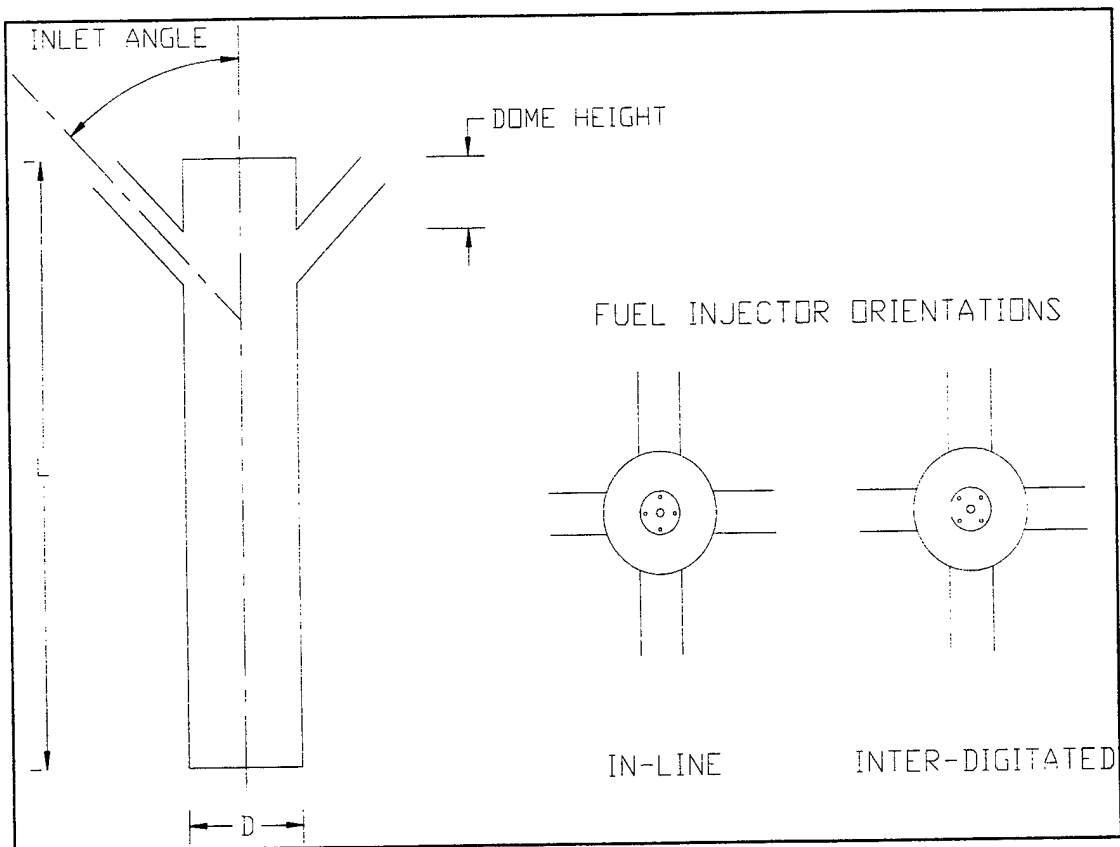
**Figure 2:** Ducted Rocket Engine Geometry Definitions

4

Ducted rocket geometries have been successfully developed and flown demonstrating their excellent long-range intercept performance [Meinkohn and Bagmen, 1982]. Although some data exist for a selected four-inlet geometry [Zetterstrom and Sjoblom, 1985], additional information is needed for systems with conventional, showerhead-type, fuel injectors. Information such as flameholder fuel distribution, fuel residence time, and flow pattern characteristics for this fuel injection scenario are needed to facilitate further development of these systems. The work performed in this study increases the level of understanding of the dome head flowfields and fuel distribution existing in four-inlet DRE's with showherhead fuel injectors.The geometrical definitions used in this paper for the four-inlet DRE system are defined in Figure 2.

Experimental Setup

The cold gas and reacting flow experiments were performed on a direct-connect blow down facility located at the Propulsion Directorate of the U.S. Army Missile Command. The experimental layout is shown in Figure 3. The facility utilizes a 500 cubic feet air storage system at a maximum pressure of 2500 psi for supply air which can be delivered at flow rates up to 10 lbm/sec. The large air capacity affords long run times exceeding 6 minutes in duration, even at the largest flow rate.

The vitiating heater uses gaseous hydrogen as a fuel and can provide inlet temperatures up to 1500 °R at the maximum air flow rate. The replenishment oxygen is added upstream of the vitiating heater in order to promote more complete combustion in the vitiator.

A high pressure air ejector is used to provide subatmospheric exhaust pressure conditions. The high pressure air ejector allows nozzle base pressures as low as 4 psia. The resulting flight simulation envelope includes Mach numbers from 1.9 to 3.1 at sea level increasing to a range of 2.55 to 3.7 at a maximum simulated altitude of 65,000 feet [Blevins, et al. 1995].
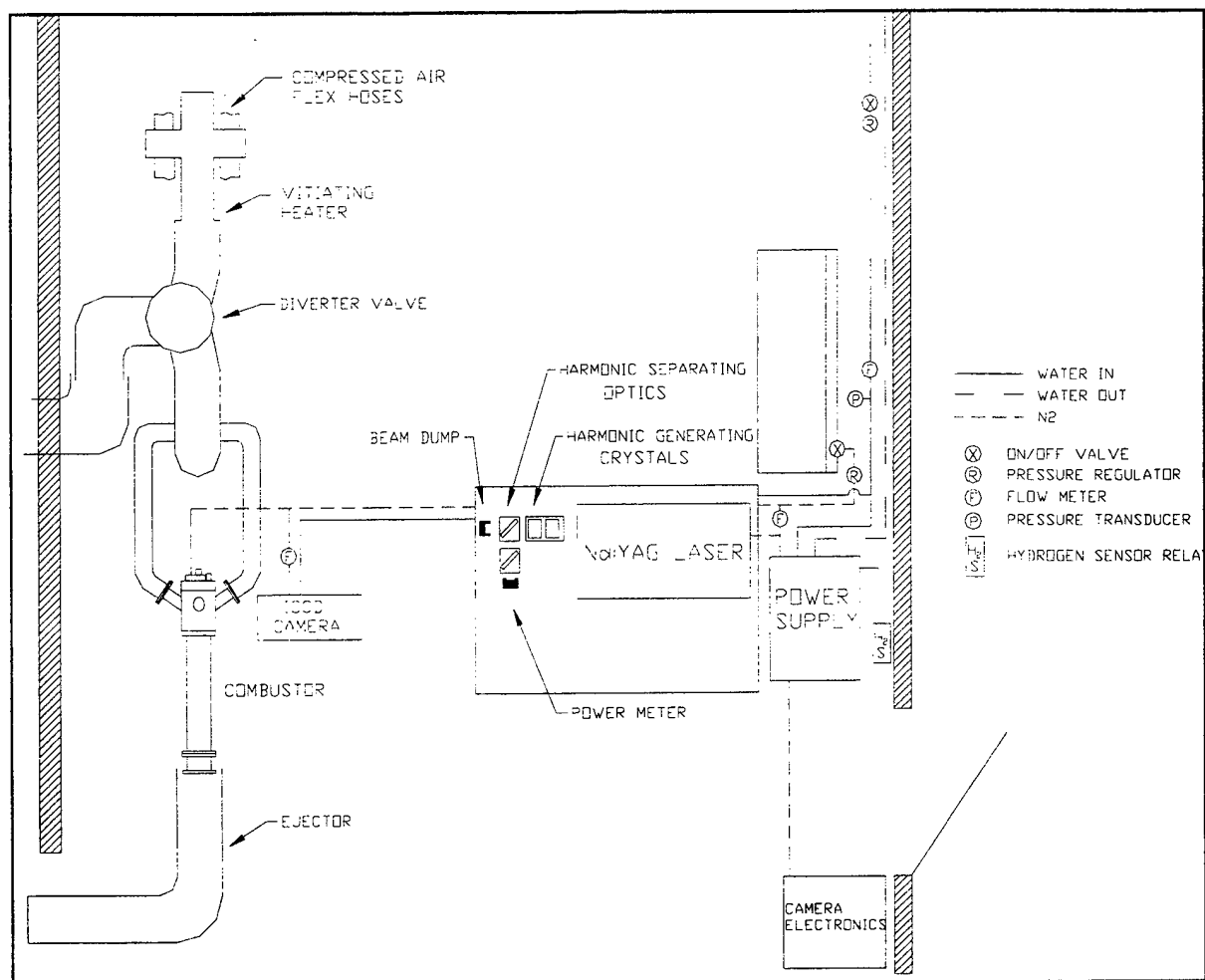
Figure 3: Direct-Connect Facility at the U.S. Army Missile Command
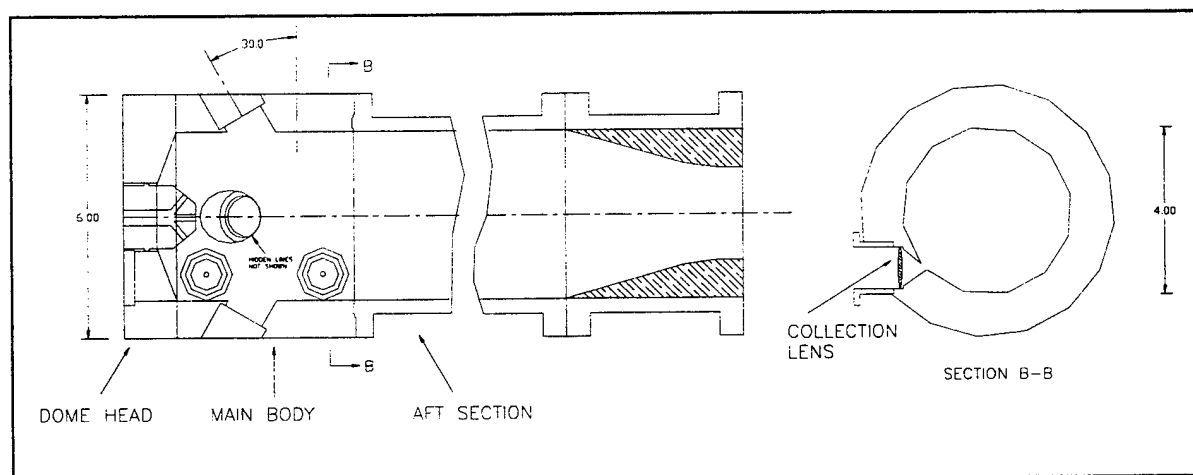
Figure 4: Optical Combustor Schematic

The facility was supported and monitored by a Keithley 12-bit A/D data acquisition system which monitored and array of Validyne and Omega pressure transducers and 6 oven-referenced Omega thermocouples.

The methane delivery rates were obtained by monitoring the static pressure differential existing across mass metering venturies fabricated and calibrated by Fox Metering Systems. Methane static pressure and temperature measurements were made across the venturi bank and immediately prior to methane injection to allow precise mass flow rate measurements.

Optically Accessible Combustor

The heart of the optical diagnostics hardware was the optically accessible combustor. A schematic of the combustor is shown in Figure 4. The combustor was composed of three segments; the dome head, the main body, and the aft section. All the combustor segments were made of 317L stainless steel except the inlet arms, which were made of 304L stainless steel. The dome head had a center hole cut in it with an accompanying #26 O-ring groove for the fuel injector. A MS33649 standard hydrogen torch port was cut adjacent to the hole and was used for the ignition torch. The dome head also contained a 1.5mm by 30mm slit through which the laser sheet was directed. A fused silica window was placed into the cutout recession which had grooves cut into the base through which nitrogen was purged. The nitrogen purge was used to keep the window clean and was fed through a pressure sealing face which bolted to the dome head and holds the fuel injector and window in place.

The main body had an internal diameter of 101.6 mm and a wall thickness of 25.4 mm. It contained four air-inlet arms with an internal diameter of 25.4 mm and a wall thickness of 3.175 mm that had been welded in place. It bolted to the dome head by eight Allen bolts and formed a pressure seal through a combination o-ring/ceramic gasket seal. The ceramic gasket had an I.D. of 101.6 mm and an O.D. of 121.3 mm and protected an O-ring seal with a 3.1 mm thickness and an inner diameter of 121.6 mm. The main body contained two pinhole camera cavities, of which one

housed the primary collection optics. The primary collection lens was a biconvex fused silica lens with a focal length of 17.0 mm at λ=400 nm and had a anti-reflective coating optimized for a wavelength of 400 nm.

The cavity was capped with a 25.4 cm viewport window which had a thickness of 10 mm. Nitrogen was purged directly below the window and was allowed to flow around the biconvex lens in order to keep it cool and clean. Care was taken to generate a uniform Nitrogen flowfield around the lens in order to inhibit any form of circulation to occur.

The aft section of the combustor had a wall thickness of 6.3 mm and was bolted to the main body in a similar fashion as the dome head. It contained two static pressure transducers located within 50 mm of either end of the section. Thermocouples were also placed on this section to monitor the combustor surface temperature. Flow exited the aft section through a graphite sonic nozzle.

The fuel injectors used with the combustor were geometrically similar to the one used for the water flow visualization study [Brophy and Hawk, 1996]. They were both five-orifice injectors made of 304 stainless steel with one axial orifice and four off-axis at 45 degrees to the combustor axis and equally spaced at 90 degrees. The orifices of the injectors were scaled so that the momentum ratio range investigated in the water flow visualization study could be properly matched in the cold gas and reacting flow studies.

Optical Illumination and Collection Optics

The laser source used in the tests was a Quantel Nd:YAG system. Using a pair of INRAD mixing crystals, 230 mJ at the third harmonic (355nm), was deliverable to the combustor at a repitition rate of 5 Hz and a pulse width of approximately 10 ns. All of the mixing crystals, harmonic separators, and sheet lighting lenses were coated with anti-reflective coatings in order to provide greater than 99% transmission at the optimized wavelength.

A number of check-out tests were performed with the combustor located in a laboratory on the UAH campus. The tests were performed to investigate the Raman imaging quality. The laser output was formed into a sheet with a height of about 25 mm and an approximate thickness of 0.5 mm at the imaged location through the use of one plano-convex spherical lens and two cylindrical lenses. The sheet was directed into the combustor through the dome head and illuminated the center plane of one of the off-axis fuel jets.

A Princeton Instruments ICCD 576s Intensified CCD (ICCD) camera was used to collect the CH_4 Vibrational Raman image signal at a wavelength of 396 nm. The camera was controlled by a Princeton Instruments ST130 controller and a Princeton Instruments PG 200 programmable pulser. The image from the primary collection lens was turned 90° after passing through the window by a fused silica prism. The image was then filtered so only the selected wavelengths were transmitted to the camera. An ORIEL filter centered at 396nm was used for the study and was 50.8 mm in diameter. The filter was a 3 cavity design and had a FWHM of 10 nm which was required to minimize the attenuation of off-axis rays collected in the image. The filter was attached to the end of a 105mm f 2.8 NIKON focusing lens attached to the ICCD. The imaged area was approximately 30 mm in diameter.

Results

The knowledge gained from the water flow visualization work was used to direct the cold flow tests performed. The reader is directed to Brophy and Hawk [1995,1996] for additional information on the water-flow visualization results.

The images presented in this work are for a 60 degree four-inlet same-station combustor with a dome height of 0.22D. The "same-station" description implies that all of the air inlet arms are located at the same axial location. Figure 5 shows a 90 degree same-station combustor and depicts the location of the imaged area. The imaged location is the same for the 60 degree combustor.
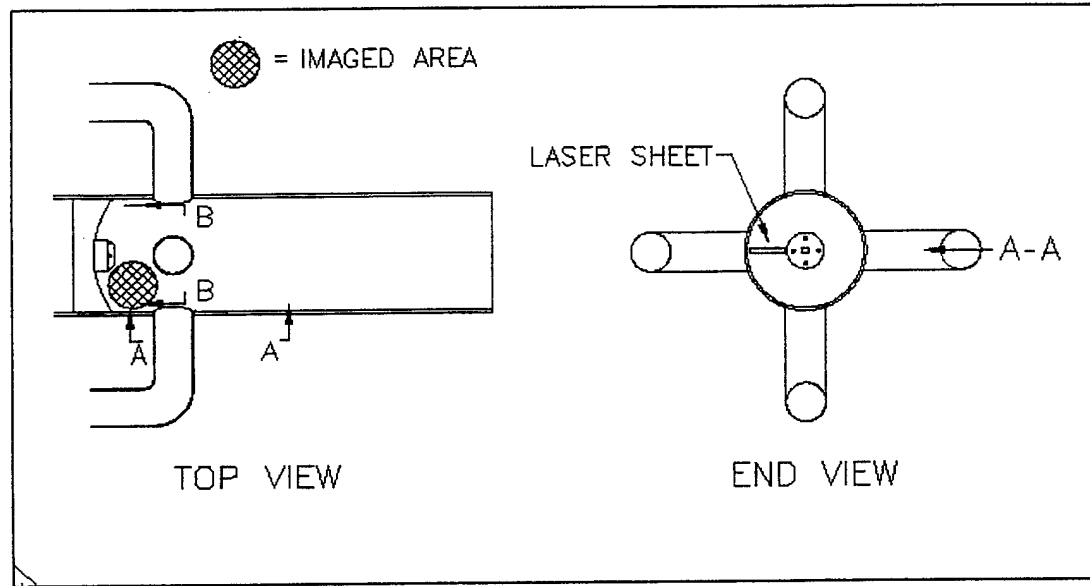
Figure 5: Imaged Area Location and Sheet Lighting Orientation

Cold Flow Experiments

The cold flow experiments investigated the mixing of vitiated air and gaseous methane (CH_4) over similar momentum ratios and fuel injector orientations as in the water visualization study. A total of fourteen tests were run with the optically accessible combustor which had 60° air inlet arms, a dome height of 0.22D, and a five orifice fuel injector modeled after the water flow visualization injector. Two injectors with different orifice sizes were fabricated for the combustor in order to maintain subsonic injection and still cover the momentum range investigated in the water flow visualization study. The conditions simulated and flow rate settings for each run are listed in Table 1. The term ϕ describes the overall equivalence ratio of the combustor and is defined as:

$$\phi = \frac{F/A}{(F/A)_{ST}} \tag{1}$$

All combustor configurations had sonic graphite nozzles installed with various area ratios to obtain the targeted chamber pressures. Thrust and chamber pressure measurements were made for

each configuration as well as inlet total pressure, inlet static pressure, and inlet static temperature for the vitiated air. Fuel flow was controlled by a dome loaded regulator which supplied methane service pressures from 350 to 1000 psi to a bank of three mass metering venturies. Any combination of venturies could be opened or closed which provided a wide range of fuel delivery rates. Two fuel injectors were fabricated in order to properly cover the desired mass flow and momentum ratio ranges. Both injectors were modeled after the water flow visualization fuel injector and had one center fuel jet and four equally spaced off-axis fuel jets angled at 45°. The "high velocity" fuel injector had a center fuel orifice diameter of 5.32 mm and four off-axis holes with diameters of 3.1 mm. The "low velocity" fuel injector had a center fuel orifice diameter of 10.65 mm and four off-axis holes with diameters of 6.53 mm.

The calibration of the Raman signal was performed by first sealing and evacuating the combustor to 1kPa and then pressurizing it with methane to a pressure of 200.0kPa. Laser shots were directed through the quartz window in the dome head and into the combustor as thin laser sheets. Image intensities were obtained as a function of pressure thereby obtaining a molar concentration versus image intensity calibration. Since the methane distribution could be assumed to be uniform, the images were spatially corrected for the sheet light intensity distribution, pincushioning effects, and attenuations associated with filtering off-axis rays.

Most of the images obtained from the cold gas study are an accumulation of 20 to 30 sequential laser shots which were acquired over a 5 to 6 second time period. This was needed in order to obtain signal to noise ratios of acceptable levels (>10). The ICCD camera was synchronized to the laser Q-switch output and was gated for a shutter speed of 40ns. The camera was also set to collect a specified pixel definition which only included the imaged area. This reduced the scanning time and allowed the camera to collect an image for every laser pulse when the laser was set to a repetition rate of 5 Hz. The pixel resolution at the center of the images was 0.17mm x 0.17mm x 0.5mm and decreased at the perimeter to 0.47mm x 0.47mm x 0.5mm due to the pincushioning effect. The presence of concentric circles near the perimeter of the cold

Table 1: Cold Gas/Reacting Flow Test Conditions and Settings

Test No.	Fuel Injector Orientation	Chamber Pressure (Gage)	$\dot{m}_a$ (kg/s)	$\dot{m}_f$ (kg/s)	$\dfrac{\dot{m}_a v_a}{\dot{m}_f v_f}$	ϕ	Fuel Type
1	In-Line	174.3 kPa	1.72	0.100	18.17	1.0	CH_4
2	In-Line	257.7 kPa	2.41	0.1823	11.31	1.31	CH_4
3	In-Line	254.9 kPa	2.39	0.111	29.98`	0.8	CH_4
4	In-Line	174.3 kPa	1.72	0.060	18.73	0.6	CH_4
5	In-Line	174.3 kPa	1.72	0.03	50.00	0.3	CH_4
6	Interdigitated	174.3 kPa	1.72	0.030	50.00	0.3	CH_4
7	Interdigitated	174.3 kPa	1.72	0.080	28.00	0.8	CH_4
8	Interdigitated	174.3 kPa	1.72	0.120	12.64	1.2	CH_4
9	In-Line	174.3 kPa	1.72	0.100	18.17	1.0	CH_4
10	In-Line	174.3 kPa	1.72	0.080	28.00	0.8	CH_4
11	In-Line	174.3 kPa	1.72	0.120	12.64	1.2	CH_4
12	Interdigitated	398.3kPa*	1.65	0.107	11.43	1.2	CH_4+H_2

*With combustion

flow images is a result of the post-processing of the images to correct for the pincushioning effect.

Of the 12 successful tests listed in Table 1, four produced images which clearly depict flowfield structure and fuel concentration levels for the cold flow tests. A "ghost" image of the combustor geometry is shown with the images presented to provide a point of reference. The fuel concentration levels are represented by the grey-scale legend to the right of the images which asscociates an f-parameter value to each portion of the imaged area. The f-parameter is also known as the stoichiometric mixture fraction parameter and is defined as

$$ f = \frac{\dfrac{F}{A}}{\dfrac{F}{A} + \dfrac{F}{A}\Big|_{ST}} \tag{2} $$

where $\dfrac{F}{A}$ is the local fuel to air ratio and $\dfrac{F}{A}\bigg|_{ST}$ is the stoichiometric fuel to air ratio. The term f is convenient since it can only vary from 0 to 1. When f is between 0 and 0.5, fuel lean conditions exist and a value between 0.5 and 1 therefore corresponds to fuel rich conditions. A value of 0.5 corresponds to a local equivalence ratio of 1. The flammability limits for methane and air at STP conditions are between equivalence ratios of 0.53 and 1.6. These values correspond to f parameter values of 0.36 to 0.615 respectively and are labeled on the figures for convenience.

The following sections will refer to two different recirculation regimes observed for the in-line fuel injector orientation. Both of the recirculation regimes were observed and labeled during the previous water flow visualization portion of this work. They were termed passive and impinging. The passive regime was found to exist at high air/fuel momentum ratios when the off-axis fuel jets were observed to "bend back" and passively follow the incoming air stream. The impinging regime was seen to occur at low air/fuel momentum ratios where the off-axis fuel jets dominated the flowfield and impinged on the incoming air stream. The passive and impinging regimes are depicted in Figures 6 and 7 respectively.

High Air/Fuel Momentum Runs

The best image of a high air/fuel momentum ratio condition is from Run 3 and is shown in Figure 8. This run had an air/fuel momentum ratio of 29.98 and Figure 8 reveals evidence of the passive recirculation condition. Evidence of the incoming air jet can be seen in the lower right corner of Figure 8. The strong fuel-deflecting power of the high momentum air is seen to force the fuel to follow the large recirculation zone in the dome head. The disappearance of fuel from the right side of the imaged area is believed to be due to deflection of the fuel jet out of the illumination plane by the incoming air column.
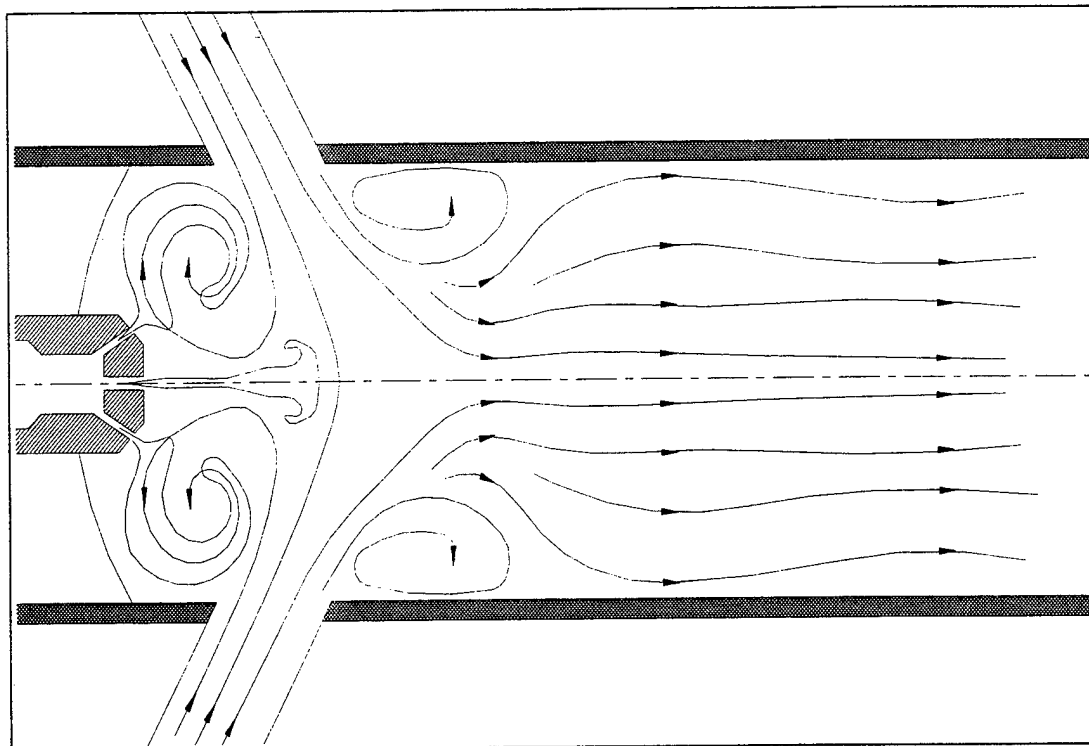
Figure 6: Passive Recirculation Regime

☐ =FUEL DISPERSION PATTERN
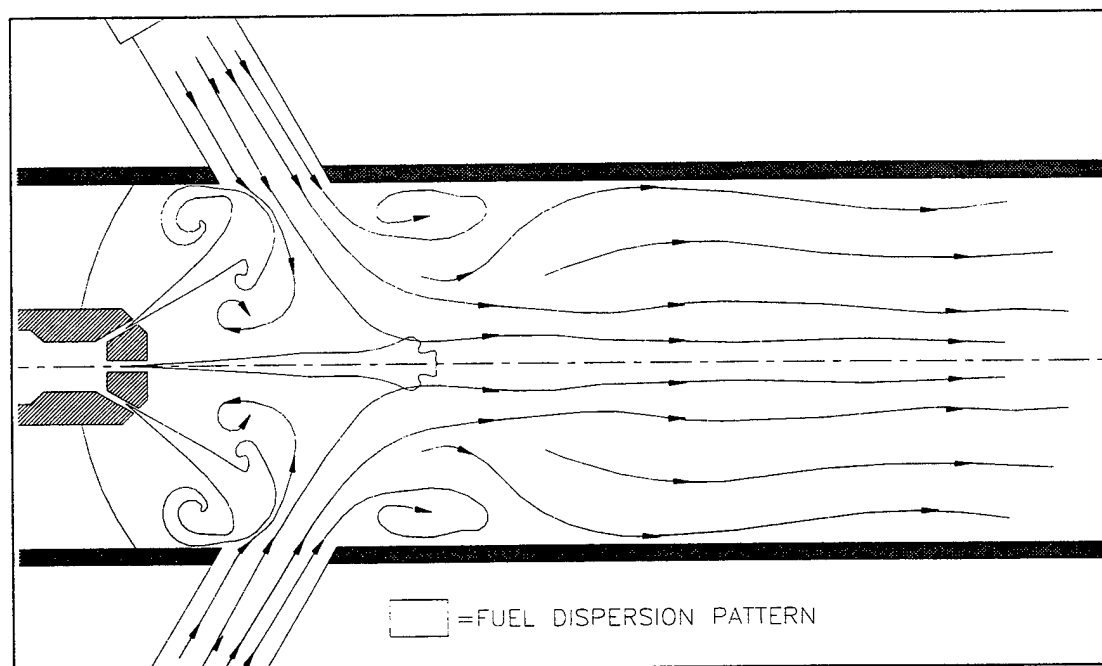
Figure 7: Impinging Recirculation Regime

14

The higher air flow rate runs, 2 and 3, resulted in higher overall combustor pressures and therefore yielded higher S/N ratios. The lower combustor pressure runs ($\approx$174 kPa) appeared to reveal similar flow field features and methane concentration levels, but at lower S/N ratios. Signal to Noise levels for the low equivalence ratio runs (ϕ<0.4) bordered on acceptable at times, obviously due to the overall reduced fuel levels present.
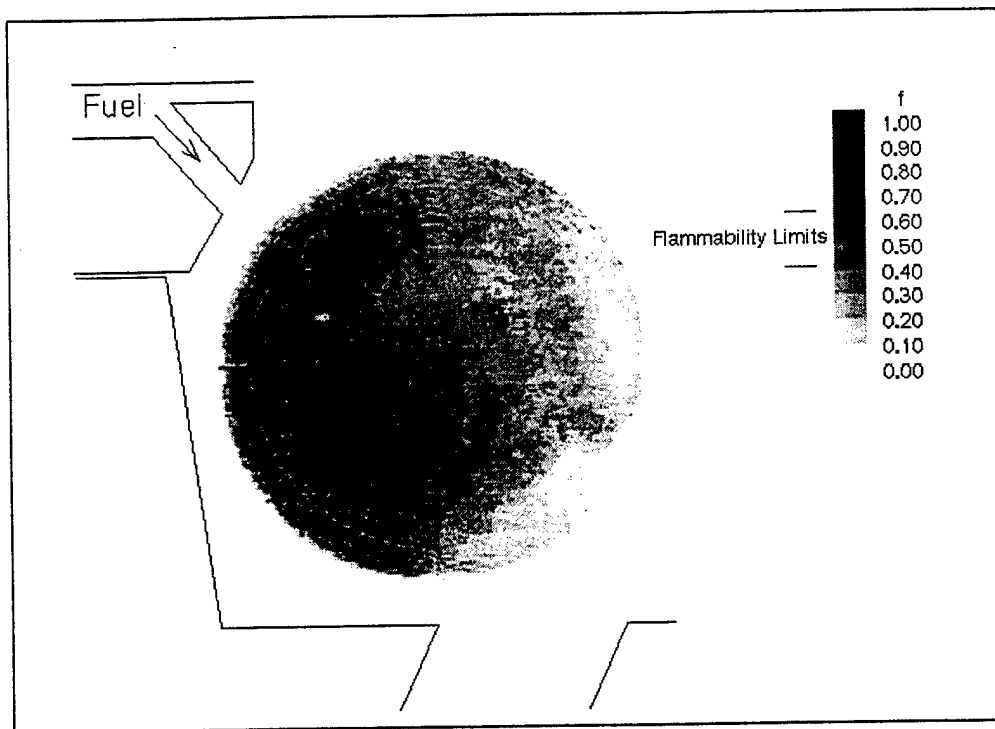
Low Air/Fuel Momentum Runs

Run 2 provided a good image of the impinging fuel jet regime shown in Figure 9. The image clearly shows the fuel jet reaching the air inlet jet. Evidence of the center fuel jet can be seen at the top of the image. This run had an air/fuel momentum ratio of 11.31 and generated very fuel-rich conditions in the dome head region.

Similar pressure and overall equivalence ratio effects on signal quality were seen for the low air/fuel momentum ratio runs as in the high momentum runs.

Fuel Injector Orientation Effects

Figures 10 and 11 display images of the same plane as the previous images, but for these images the fuel injector was rotated 45° and placed in the interdigitated orientation. It was seen that much less fuel accumulated on plane A-A compared to the in-line fuel injector orientation. Figure 10 shows the fuel concentration levels for a low air/fuel momentum ratio condition in Run 8. Figure 11 shows a similar flowfield for a higher momentum ratio condition in Run 7. Only a slight increase in fuel concentration for the fuel rich runs was seen over the fuel lean condtions. This reveals that the interdigitated fuel injector orientation desensitizes the dome head flow field to the overall fuel flow rate and momentum.

Figure 8: High Air/Fuel Momentum Ratio Image of Run 3. In-Line Fuel Injector.
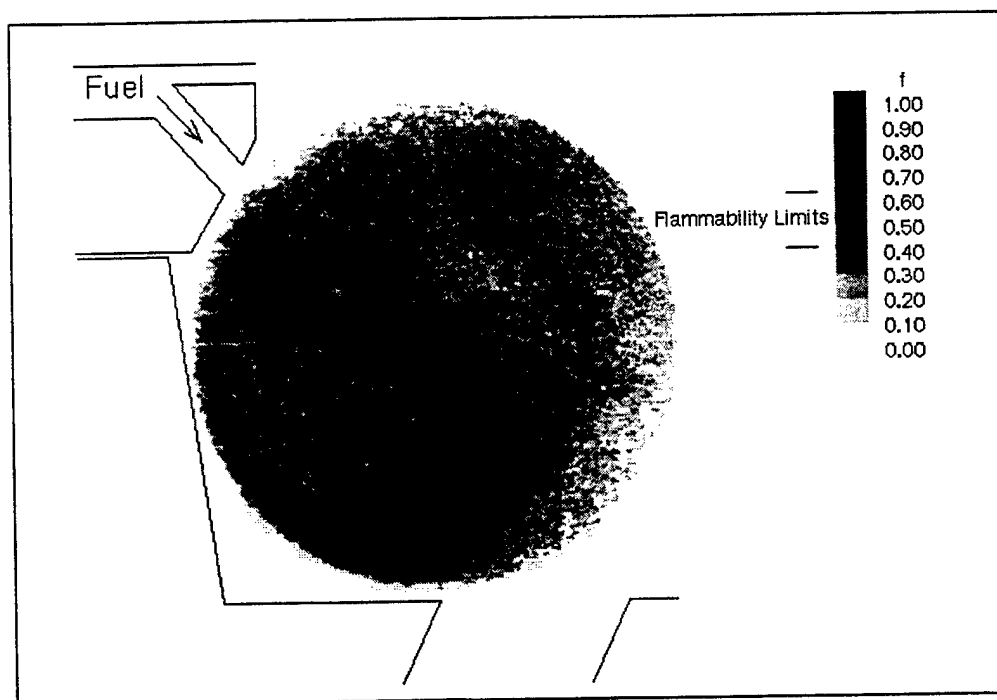
Figure 9: Low Air/Fuel Momentum Ratio Image of Run 2. In-Line Fuel Injector.
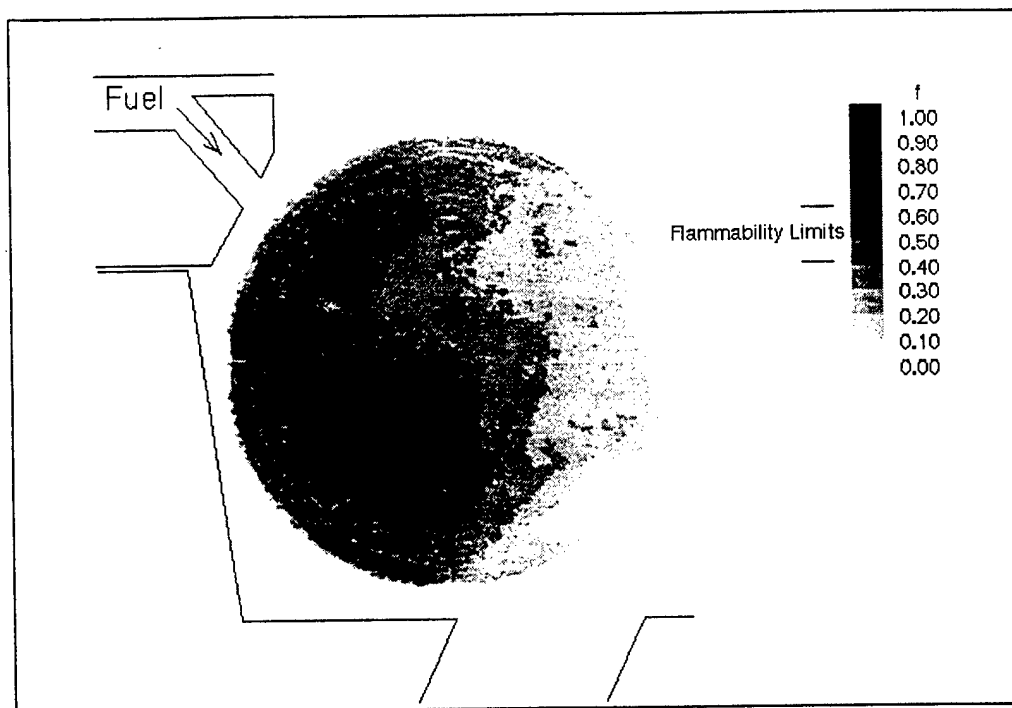
Figure 10: Low Air/Fuel Momentum Ratio of Run 8. Interdigitated Fuel Injector.

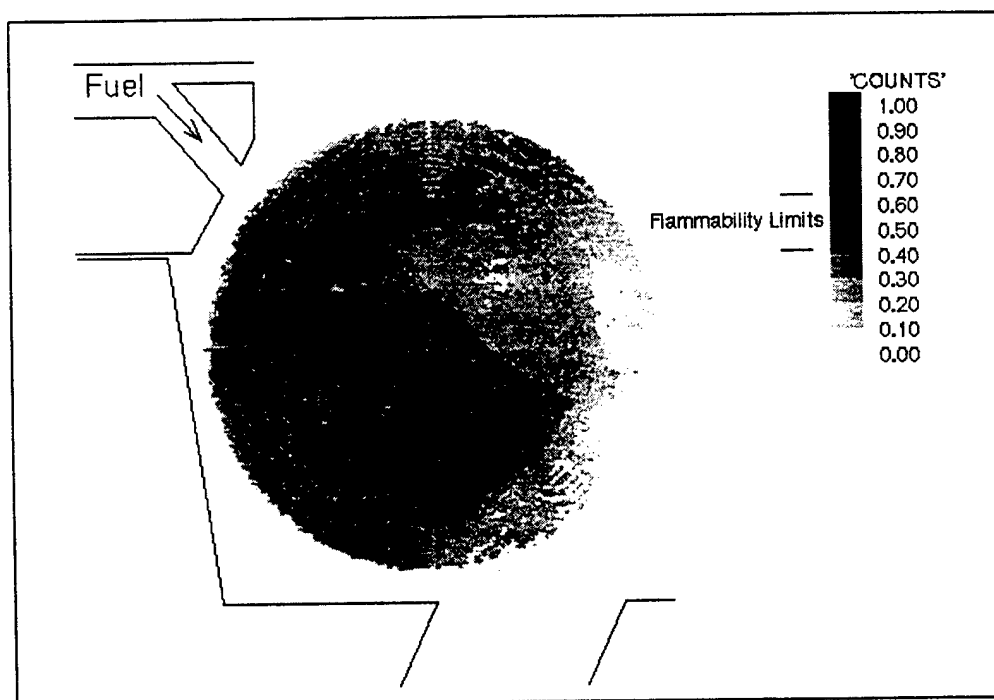**Figure 11**: High Air/Fuel Momentum Ratio of Run7. Interdigitated Fuel Injector.

Discussion

The cold flow studies involved the imaging of CH_4 using Raman spectroscopy. Since the imaged signal strength was a function of molar concentration (pressure), the higher pressure conditions yielded higher signal to noise ratios than the lower pressure runs. This was seen to be very important for the lower equivalence ratios investigated since lower overall methane concentrations existed. Figure 8 shows results from Run 3 with a high air/fuel momentum ratio of 29.98. For this condition, the air inlet jet dominantly controlled the off-axis methane jet. Notice that the fuel jet is forced to follow a pattern suggested by Figure 6 of a similar momentum ratio condition simulated by the water flow visualization study. The large well-defined fuel concentration gradient seen in Figure 8 implies that the flow field was reasonably stable and steady over the 20 image collection period. Evidence of the air-inlet jet can be seen on the right-hand side of the Figure 8. The disappearance of CH_4 from the right side of the image was believed to be due to some degree of flow directed out of the imaged plane. This test condition generated a fuel rich yet combustible mixture in the dome head recirculation region.

Figure 9 shows an image from Run 2 which had a much lower air/fuel momentum ratio of 11.13. The region had a very large amount of methane present and was predominantly fuel rich, and revealed f-parameter values well above the flammability limits. The image of the fuel jet appears to indicate an impinging type of recirculating regime, depicted in Figure 7. Conclusions from previous water flow visualization experiments[Brophy,Hawk 1997] indicated that a momentum ratio of 11.13 should result in the recirculating regime fluctuating between impinging and passive, but the image seems to depict a purely impinging regime. This is believed to be a result of the compressible gas flow versus incompressible water flow visualization.

The effects of compressibility in the cold flow tests were believed to be the reason for the definitive impinging flow regime occurring at such a high momentum ratio of 11.13. Further testing needs to by performed in order to isolate this behavior and draw firmer conclusions.

18

<u>Interdigitated Fuel Injector</u>

Cold flow images for the inter-digitated fuel injector are shown in Figures 10 and 11. Figure 11 shows the results from run 7 which was for an air/fuel momentum ratio of 28.0 and Figure 10 shows the results from run 8 which had a momentum ratio of 12.64. Although Figure 10 represents a much higher fuel flow rate, there is not much difference in fuel concentration levels on plane A-A between the two images. This observation implies that the recirculating regime on plane A-A is apparently insensitive to the overall air/fuel momentum ratio of the combustor. This is believed to be due to the majority of the fuel contained in the off-axis jets being injected around or "in-between" the four air-inlet jets and into the aft end of the combustor. The slight increase in fuel concentration levels was expected for the lower momentum ratio conditions and was believed to be due to the portion of the center fuel jet which was redirected back into the dome head region.

The fuel concentration levels seen for the interdigitated configuration fell within the flammability limits and were seen to be higher at the extreme front end of the combustor. A similar out-of-plane motion, as seen in earlier figures, was believe to be responsible for the diminishing levels of methane on the right side of the images. This fuel injection scheme appeared to be very favorable from a flameholding standpoint due to the insensitivity of the dome head fuel concentration levels to the momentum ratios evaluated and overall combustor equivalence ratios.

Figure 12 summarizes observations of the previous water flow visualization tests for three combustor geometries with the current cold flow study of the 60-degree same-station combustor. All information presented in Figure 12 is for the in-line fuel injector orientation, depicting the two recirculation regimes present. . Select cold gas test conditions are shown as "hollow" circles on the figure. Since the interdigitated configuration did not appear to have any distinct recirculation regimes, a figure for that configuration is not appropriate.
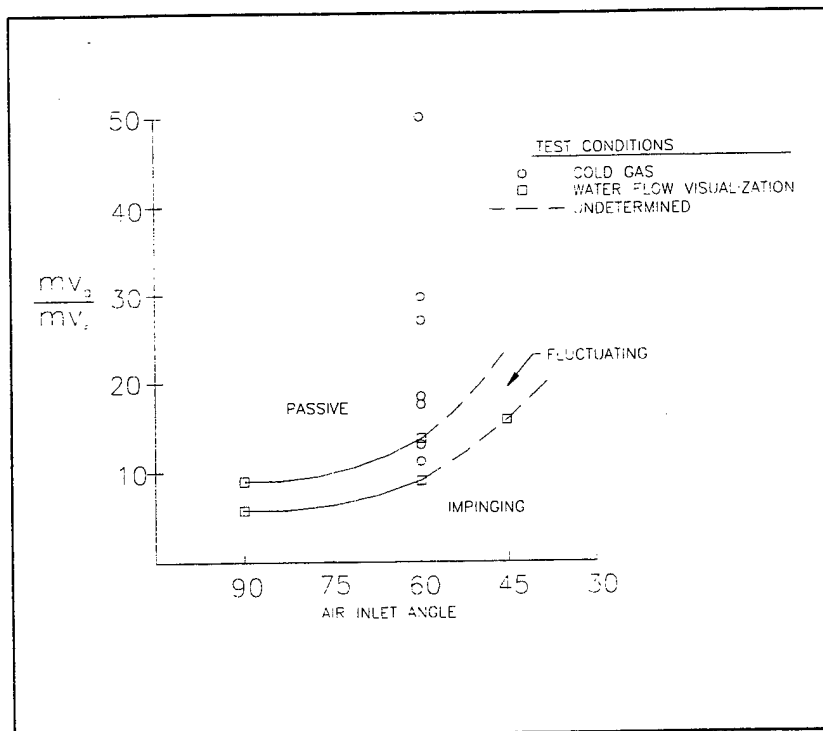
Figure 12: Recirculation Regimes for Combustors Evaluated with In-Line Fuel Injector

Summary and Conclusions

The work presented in this paper further characterizes the internal flow fields of four-inlet ducted rocket engine geometries. Vibrational Raman spectroscopy of gas-gas mixing was used to provide quantitative information on the fuel distribution for various configurations. This work compliments previous water flow visualization experiments to provide additional internal flow field characteristics of four-inlet geometries investigated. While the previous water flow visualization tests provided valuable qualitative characteristics on such flowfields, the cold gas flow tests provide quantitative information which supports prior qualitative conclusions and reveals local fuel concentrations to be expected on such systems .

20

The important conclusions reached from this work are:

1) The use of Raman spectroscopy to image the CH_4 distribution was successful and yielded the spatial distribution of fuel and information on the dome head flowfield structure. The technique was successfully applied to cold gas mixing flow fields of the optical combustor. The successful application of the technique to a reacting flowfield is possible and should be considered.

2) Observations of flowfield structures for the cold flow gas-gas mixing study agreed well with the observations made from a previous water flow visualization study and indicated that a substantial amount of inlet air is passively diverted into the dome head for four-inlet DRE combustors when compared to one and two inlet geometries.

3) The 60-degree same-station combustor was observed to have two distinct dome head recirculation regimes with the in-line fuel injector configuration as seen in previous water flow visualization tests. These regions were termed passive and impinging and were seen to be a strong function of the air/fuel momentum ratio. Fuel rich conditions typically existed on the imaged plane for this injector orientation. The combination of flow rate dependent recirculation zones and generally fuel rich conditions existing over a majority of the investigated range, resulted in the in-inline fuel injector orientation to be categorized as undesirable.

4) The interdigitated fuel injector produced combustible fuel-air mixture concentrations on the imaged plane. The fuel concentrations observed in this configuration, appeared to be desensitized to the air/fuel momentum ratios for fuel lean and fuel rich conditions. The interdigitated fuel injector was determined to be the most favorable injector orientation when operating the combustor over a wide range of air/fuel momentum ratios.

Acknowledgements

References

Blevins, J., and Coleman, H., "A Connect-Pipe Facility for the Evaluation of Ducted Rocket Engine Propellants," AIAA Paper 95-2937

Brophy, C. and Hawk, C., "Mixing and Combustion Studies of Four-Inlet Side Dump Combustors," AIAA Paper 96-2765.

Brophy C., Hawk, C., "Flow Visualization of Four-Inlet Ducted Rocket Engine Configurations, " *Journal of Flow Visualization and Image Processing*, Vol. 3, No. 1, 1997.

Kennedy, J., "Ramburner Flow Visualization Studies," 11th JANNAF Combustion Meeting, CPIA Publication No. 261, pp. 415-440, Sept. 1974.

Meinkohn, D. and Bagmen, J.W., "Experimental Investigation of a Hydrocarbon Solid Fuel Ramjet," Ramjet and Ramrocket for Military Application, AGARD-CP-507, March 1982.

Schadow, K.C., et al., "Water Tunnel and Windowed Combustion As Tools For Ducted Rocket Development," 1981 JANNAF Propulsion Meeting, Vol. 2, pp. 101-115.

Schetz, J., et al., "Flow Visualization Studies of a Solid Fuel Ramjet Combustor Using a New Material-Polyaphrons," 22nd JANNEF Combustion Meeting, pp. 351-359, October 1985.

Sochet, L.R., et al., "Use of Multichannel Pulsed Raman Spectroscopy as a Diagnostic Technique in Flames," *Combustion and Flame*, Vol. 36, pp. 109-116, 1979.

Stepowski, D., "Laser-Induced Fluorescence of the CH Molecule in a Low-Pressure Flame," *Journal of Quantum Spectroscopy and Radiation Transfer*, Vol. 32, No. 4, pp.363-370, 1984.

Stull, F.D., and Craig, R.R., "Investigation of a Ducted Inlet Side Dump Combustor Using Liquid Fuel Injection," *Journal of Propulsion and Power*, Vol. 1, No. 1, Jan.-Feb. 1985, pp. 83-88.

Vanka, S.P., Craig, R.R., and Stull, F.D., "Mixing Chemical Reaction and Flow Field Development in Ducted Rocket Engines," ANL-84-62, Sept. 1984.

Zetterstrom, K-A. and Sjoblom, B., "An Experimental Study of Side Dump Ramjet Combustors," 7th Internation

AIAA 96-2765

Mixing and Combustion Studies of Four-Inlet Side Dump Combustors

C.M. Brophy and C.W. Hawk

Propulsion Research Center
Department of Mechanical and Aerospace Engineering
The University of Alabama in Huntsville
Huntsville, AL 35899

32nd AIAA/ASME/SAE/ASEE
Joint Propulsion Conference
July 1-3, 1996 / Lake Buena Vista, FL

Mixing and Combustion Studies of Four-Inlet Side Dump Combustors

Christopher M. Brophy* and Clark W. Hawk†
Propulsion Research Center
Department of Mechanical and Aerospace Engineering
University of Alabama in Huntsville, Huntsville, AL 35899

Abstract

Water flow visualization and preliminary combustion studies have been performed in order to investigate the mixing and combustion processes inside of four-inlet side dump combustors also known as ducted rocket engines (DRE). The flow fields of four-inlet side dump combustor geometries were visualized using water flow visualization and documented with video and conventional photography so that relationships between various geometric/flow parameters and the flow field behavior could be obtained. It was shown that for inlet angles greater than 60 degrees, the geometries intrinsically direct a significant portion of the inlet flow towards the dome head region without the need for diverter devices. The resulting dome-region flow field contains two distinct recirculation patterns shown to be dependent on the momentum ratio and inlet flow inlet angle. These parameters are believed to strongly affect the existence and strength of transport mechanisms between the fore and aft combustor segments. The flow visualization work concluded that the 60 degree same-station combustor produced a favorable flow field over the range investigated and became the chosen geometry for the reacting-flow study. The geometry was used to construct an optically accessable stainless steel combustor for a reacting flow investigation. The reacting flow work utilizes laser induced fluorescence to view the flame front (CH) distribution and will potentially utilize stimulated Raman spectroscopy to view the cold/hot flow CH_4 behavior. Initial calibration work has been performed on campus. Direct-connect testing will take place at the U.S. Army Missile Command this summer.

Nomenclature

D = combustor model diameter
$\overline{U}$ = mean combustor flow velocity
h = dome height
x = axial location along combustor
$\dot{m}_a$ = mass flow of air
$\dot{m}_f$ = mass flow of fuel
$\dot{m}_a V_a$ = momentum of air
$\dot{m}_f V_f$ = momentum of fuel
Re_D = Reynolds number, UD/υ
ν = Kinematic viscosity

Introduction

Ducted rocket engine systems have recently received a revived interest due to their high specific impulse, throttlability, and suitability for long range applications. They obtain the high specific impulse by ducting the inlet flow in which they fly through inlet ducts and using it as the oxidizer which is mixed with a fuel rich gas from a gas generator. The mixture combusts and is then accelerated through a converging/diverging nozzle to generate thrust. A diagram showing the general layout of a DRE is shown in Figure 1. Much of the work performed in the past has been concentrated on one- and two-inlet geometries. These geometries offer an aerodynamic advantage since the inlet ducts may be tailored to generate lift for the vehicle but often require some type of inlet flow deflecting device to be installed in the ducts so that sufficient inlet flow enters the dome region of the combustor where the flameholding process typically occurs. These combustors have often been investigated using flow visualization with water for qualitative information[1-5] and direct-connect hot-fire testing for quantitative results[6-9].

Four-inlet geometries offer advantages over the one and two-inlet geometries such as steer-to-turn capability and the tendency to passively divert
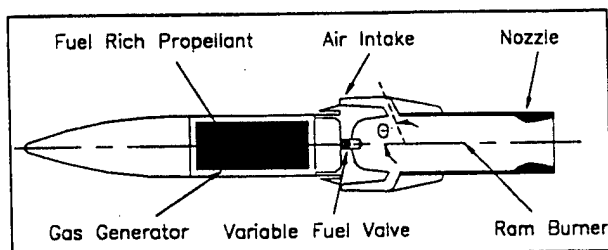
* Student member, AIAA
† Associate fellow, AIAA

Figure 1: A ducted rocket engine schematic

necessary inlet flow into the dome region of the combustors for flameholding requirements without the use of diverter devices commonly needed on other combustors. The effects of inlet flow angle, dump station, air/fuel mass ratios, air/fuel momentum ratios, dome height, and injector performance were investigated over a wide range with a water flow visualization facility and resulted in a 60 degree same-station combustor geometry to be chosen for the combustion diagnostics tests.

The reacting flow experiments will duplicate the momentum and mass flow range investigated in the flow visualization study in order to compare the flow fields observed for each study. Planar Laser Induced Fluorescence and Raman spectroscopy will be used to view the flame front (CH) and fuel (CH₄) distributions respectively. Additional information will be obtained pertaining to the flow structure existing near the flame-out condition for four-inlet same station side dump combustors.

Experimental Setup

Flow Visualization Facility

The flow visualization facility (Figure 2) has overall dimensions of 6.1 meters by 4.6 meters. Not shown in the figure are the 3800 liter reservoir tank and the centrifugal pump located below the deck. The power plant for the facility is a 22.4 kW variable RPM centrifugal pump capable of delivering 3000 liters per minute at 207 kPa to the combustor model. This pump was dedicated to delivering high volume at low pressure and was used to supply water as the "air" source for the combustor. A supplemental 517 kPa water supply arm was used to deliver the water for the "fuel" source at up to 132 liters per minute. The amount of water delivered to the model was controlled both by the pump RPM and by throttling the supply arms with globe valves. A PC monitored Blancett 401 flowmeters used on each arm, two pressure transducers, and provided remote pump control if desired. The combustor models were placed inside a 0.92m x 1.00m x 0.60m viewing tank which contained water to minimize refraction effects.
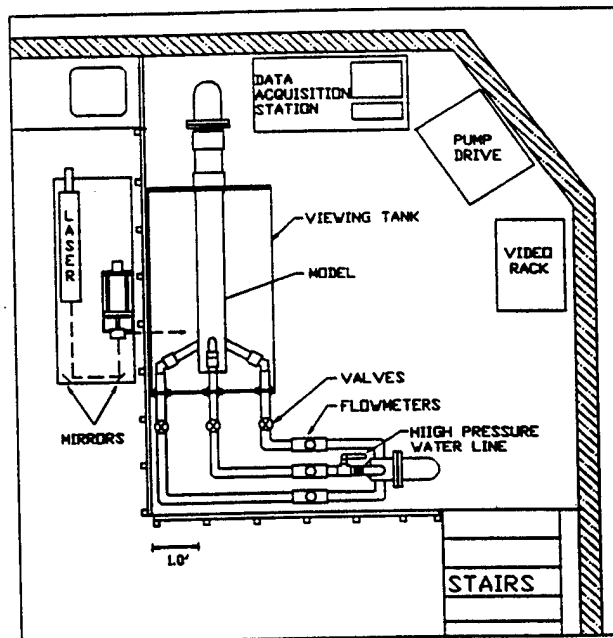

Figure 2: Flow Visualization Facility

The fuel injection geometry (Figure 3) is a concave dome head which contains the fuel injector and allows positioning at any axial location in the front end of the combustors. The dome height is defined as the axial distance between the beginning of the inlet flow dump station and the perimeter of the dome head. A five orifice injector was used, one axial orifice and four off-axis orifices angle at 45 degrees to the combustor axis.

Visualization of the flow field was achieved by seeding the reservoir tank with 0.0254 cm (0.010") polystyrene spheres. The fuel jet was left unseeded. "Outgassing" of air in the "fuel" supply after experiencing the pressure drop across the injector resulted in a mist of tiny inlet flow bubbles which provided adequate visualization of the fuel flow. A 5 watt Argon Ion laser was used to illuminate the flow field. The laser output was first focused and then expanded through a cylindrical lens to produce a light sheet approximately 1.0 mm thick. The sheet was capable of being oriented either vertically or horizontally. The images observed were captured on Hi8 video and by conventional photography.

Preliminary Hot-Fire Setup

A 101.4 mm internal diameter optically-accessible stainless steel combustor was constructed based on conclusions from the flow visualization work. The combustor has four same-station 60 degree inlet arms and a dome height of 1.27 cm. A 30.0 mm x 0.75 mm slot exists in the dome head of the combustor to allow a laser sheet to enter the combustor. Viewing of the illuminated area was performed by employing a

2

pinhole-like camera design (Figure 4). This design allows for a constant nitrogen flow over the primary collection optic in order to keep it clean during future direct-connect tests. The amount of nitrogen purged through the aperture will be typically less than 0.30% of the total flow rate of the combustor.

The preliminary combustor tests have been performed in a lab on campus in order to calibrate the collection optics and also to become familiar with the combustor and the methods used. The combustor was located on an optical table and burned methane through the fuel injector to generate both laminar and turbulent diffusion flames. The simple flame geometries allow calibration and evaluation of the optical techniques to be used. The physical layout is shown in figure 5.

The third harmonic of a Continuum SL-10 Nd:YAG was used to optically pump a Continuum ND60 dye laser containing a Coumarin 120 dye. Typical output energies were 6 mJ at 431.5 nm over a 5 ns pulse length. The output from the dye laser was vertical polarized and possesed a bandwidth of approximately .05 cm^{-1}. The beam first passed through a 1.0 m focal length plano-convex lens and then two cylindrical lenses to create a laser sheet 2.0 cm wide and 0.3 mm thick which was then directed into the combustor through the dome head.

The collected image was collimated, filtered by a 9 nm bandpass filter centered at 490 nm, and then refocused. A Princeton Instruments intensified CCD camera collected the image through a
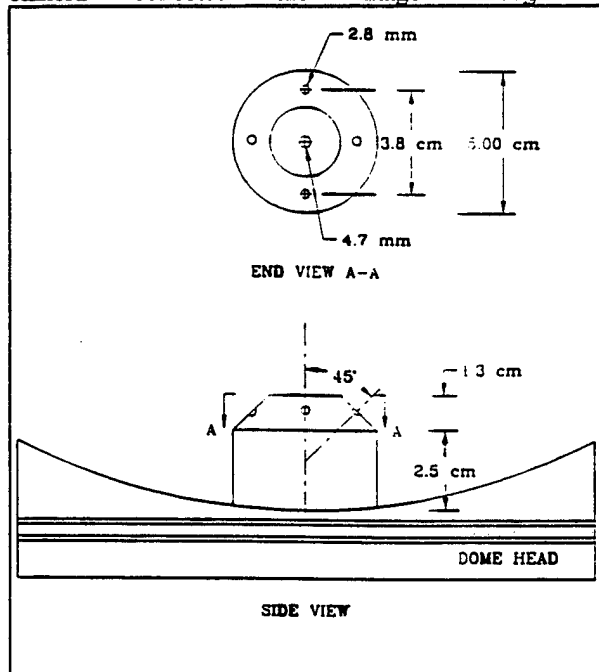
105mm focal length lens at a f-stop of 2.8. The imaged area was approxiamately 3.0 cm by 1.4 cm.

Results and Discussion

The flow visualization studies investigated two types of combustors, same-station and alternating station combustors. All were six-inch I.D. models and consisted of 45, 60, and 90 degree inlet flow inlet arm dump angles each with an internal diameter of 3.81 cm. All were investigated up to a Reynolds number of 5.5 x 10^5, but no Reynolds number effects were observed above Reynolds numbers of 1.5 x 10^4. The mass flow ratio ($\dot{m}_a / \dot{m}_f$) and momentum ratio ($\dot{m}_a V_a / \dot{m}_f V_f$) were varied between 10 to 60 and 0.43 to 2.58 respectively.

Dome Height

Dome height was the first parameter investigated. The first combustor tested was the 90 degree same-station combustor. A dome height of 0.25D (3.81 cm) resulted in symmetric, stable recirculation regions for the 90° same-station combustor over a wide range of momentum ratios and appeared to be the preferred height for that combustor and the fuel injector used based on the size and strength of the recirculation regimes. The preferred height was determined after testing each dome height setting over the range of momentum ratios specified earlier. Figure 6 shows the operating zones for momentum ratio versus dome
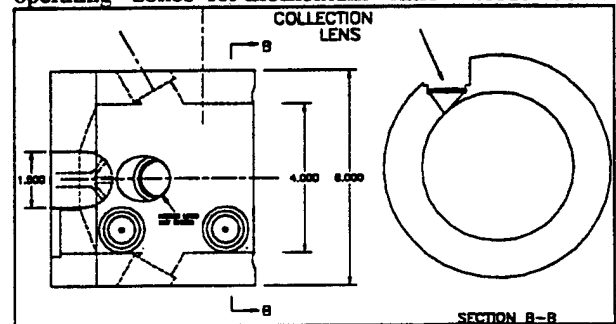

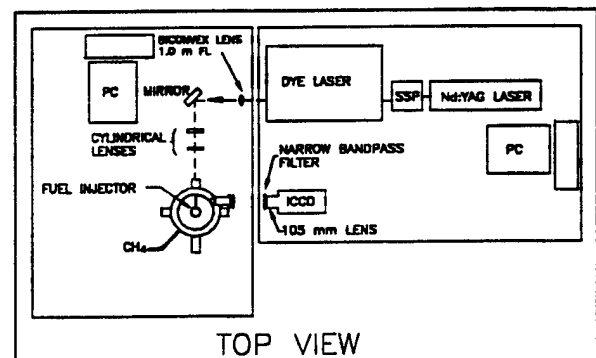Figure 4: Optical combustors showing pinhole camera

Figure 3: "Fuel" injector geometry

Figure 5: Preliminary Hot-Fire Setup

height for the 90 degree combustor. The preferred dome height was then chosen as the height which minimized the fluctuating behavior between the impinging and passive recirculation regimes while also avoiding wall impingment of the fuel jet. Dome heights greater than 0.27D resulted in the fuel jets impinged on the combustor wall and not the incoming inlet flow columns. The preferred dome height for the 60° same-station combustor was determined to be ≈0.083D (1.27 cm) by the same manner. An acceptable dome height for the 45° combustor was not found, so a dome height of 0 cm was used in order to provide the strongest recirculation possible. The alternating-station combustors had problems with two of the fuel jets impinging on the wall because the same fuel injector was used on all models.

Same-Station Combustors

The 90 degree same-station combustor was investigated first with a low "fuel" flow rate. The flow field contained symmetric counter-rotating zones on both sides of the inlet flow inlet station for plane A-A. Figure 7 shows the orientation of the sheet lighting relative to the combustor. The recirculation zones increased in strength as the "inlet flow" flow rate increase, but the downstream zone appeared to fluctuate in size and shape. Figure 8 shows the pairing of two counter-rotating regions found between each of the inlet arms for plane B-B. These regions appeared to be tube-like and were seen to contain substantial amounts of "fuel". The endpoints of the tube could not be isolated, but appeared to begin in the dome head region and terminate approximately 1.0 inlet diameter downstream from the inlet flow station. The structures seen in the flow field did not appear to develop further
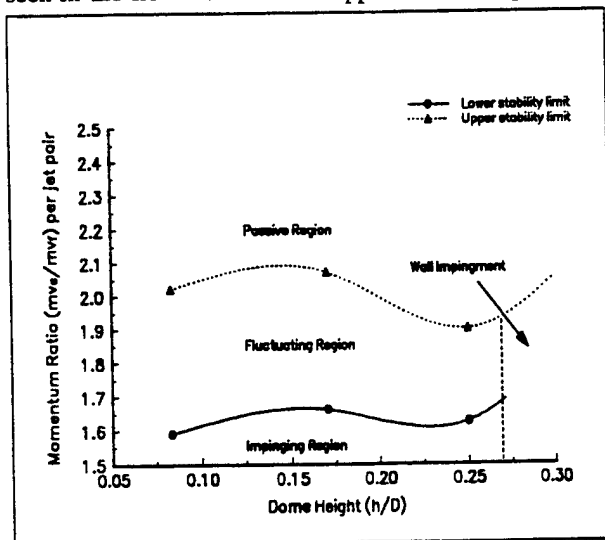
for Reynolds numbers above 5.5×10^4, but fluctuations in size and shape were observed.

The low "fuel" flow rate resulted in a momentum ratio of 2.39. For the high momentum ratios, the fuel jet was seen to "bend back" and follow the governing "inlet flow" flow. This was termed a "passive" flameholding scenario. There was no significant change in this flow field until a momentum ratio between 1.90 and 1.61 was reached. In this range, the fuel jet(s) fluctuated between the "passive" scenario and a straight fuel jet, termed "impinging", which impinged on the incoming "inlet flow" column. Below a momentum ratio of 1.61, the fuel jet would partially penetrate the inlet flow column and then bifurcate into two branches. One would be deflected towards the wall and the other towards the stagnation point of the four jets. The result was two recirculation zones split and driven by the fuel jet.

The 60 degree combustor was investigated at a dome height setting of 0.083D and over the same momentum ratio range. The recirculation regimes observed near the dome head on the 90 degree combustor also occurred in the 60 degree combustor but were seen to transition at a higher momentum ratio. The "passive" regime (Figure 9) existed down to a momentum ratio of 2.05, fluctuated in the range between 2.05 and 1.72, and became "impinging" below 1.72 (Figure 10). The critical momentum ratio values are defined as the value at which the fuel jet transitions from passive to impinging. This was taken as the center value in the fluctuating region. The critical momentum ratios for the 60 and 90 degree combustors are shown to be similar when the only lateral momentum component of the "inlet flows" were compared.

The downstream recirculation regions and reattachment lengths remained relatively constant over the momentum ratio range investigated, but did reduce in size once the center fuel jet penetrated the stagnation point of the four inlet flow columns. The transport "tubes" existing in between the "inlet flow"
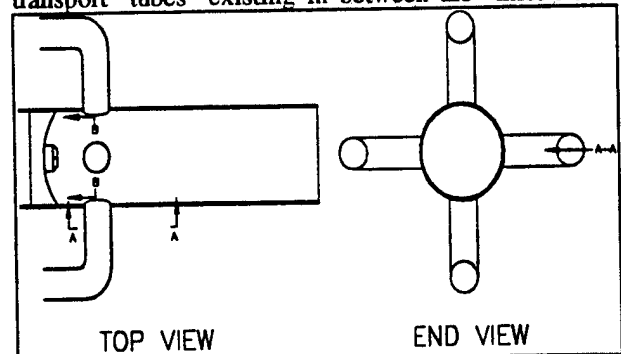
Figure 6: Recirculation regimes for 90 degree

Figure 7: Flow Visualization Laser Sheet Orientation

4

Figure 8: View B-B of 90° same-station combustor

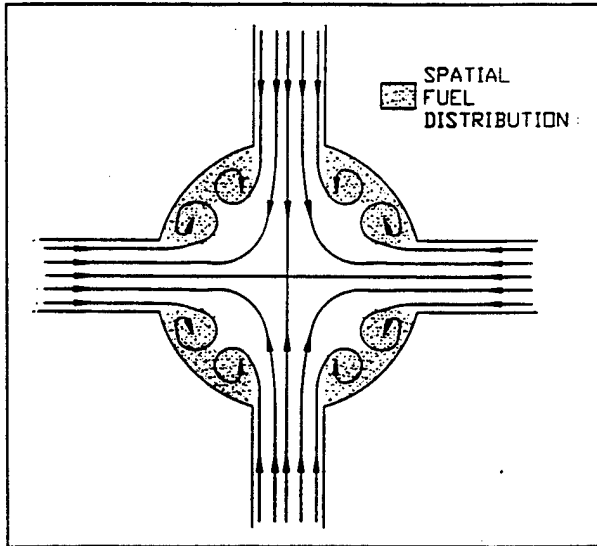**Figure 9**: Observed streamlines in 60° combustor.
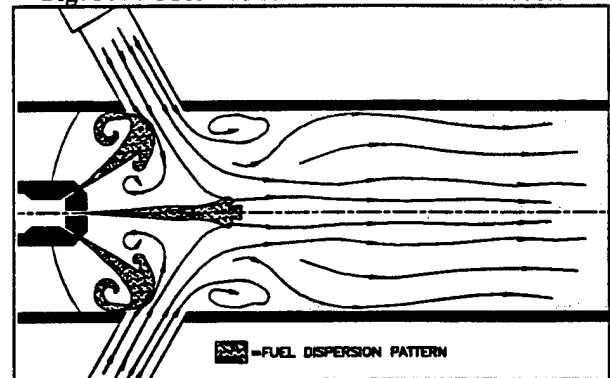
Figure 10: View A-A of 60° same-station combustor

inlet arms appeared to be weaker and shorter in length than observed in the 90 degree combustor. No fuel accumulation in the dome head region was observed for this combustor, indicating that the transport mechanisms were indeed functioning.

The 45 degree same-station combustor exhibited the weakest recirculation zones. This was likely due to the reduced amount of inlet flow momentum normal to the combustor axis which was seen to produce much of the mixing and transport that occurs between the "fuel" and "air inlet flow" jets. The center fuel jet was seen to penetrate the "inlet flow" jets easily while the fuel from the four off-axis jets seemed to accumulate in the dome head region. The flow field did not change significantly over the entire momentum ratio range The transport "tube" mechanisms existing in between the inlet arms for the 60 and 90 degree combustors could not be located for the 45 degree combustor.

Alternating-Station Combustors

The alternating-station combustors did not produce favorable flowfields. For this reason, they will not be further addressed in this paper. For a more complete review of the flow visualization work and the alternating station combustor behavior, the reader is directed to reference 10 and 11.

Preliminary Reacting Flow Results

Initial combustion diagnostics were performed on an optics table at campus. By viewing a simple methane diffusion flame through the collection optics, optical access was verified. The low f-number primary collection optic resulted in the imaged being warped in a convex manner. A conformal mapping code is being
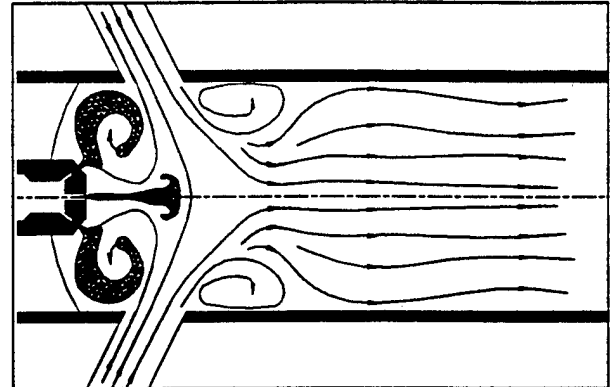
written to correct for the deformation by calibrating off of a target slide. Figure 11 shows the geometry for the calibration study. A 45 degree methane diffusion flame was used, and a laser sheet penetrated through the center of the jet from below.

The goals of the combustion diagnostics tests are to be able to view the fuel (CH_4) and flame front (CH) behavior simultaneously in the combustor. To do this, a minimum of two cameras will eventually be needed. At this point in time, only one camera is available and being used to evaluate various techniques that could be used for these goals.

The first method investigated in this study in one in which the (0,0) $A^2\Delta\text{-}X^2\Pi$ band of CH is excited at 431.5nm and the fluorescence signal is observed through the (0,1) band at 489nm. The problem with this method is that the $\Delta v \neq 0$ are only approximately 2% of the diagonal transitions and therefore are typically weak[12]. Another potential problem with this method is that there is a Stokes Raman signal existing for methane at 493.6 nm for the same excitation. Although the Raman signal was seen to be extremely weak at atmospheric pressures and the energies used in this study, the signal will become significant at higher combustor pressures. Reference 10 presents methods to separate these signals.
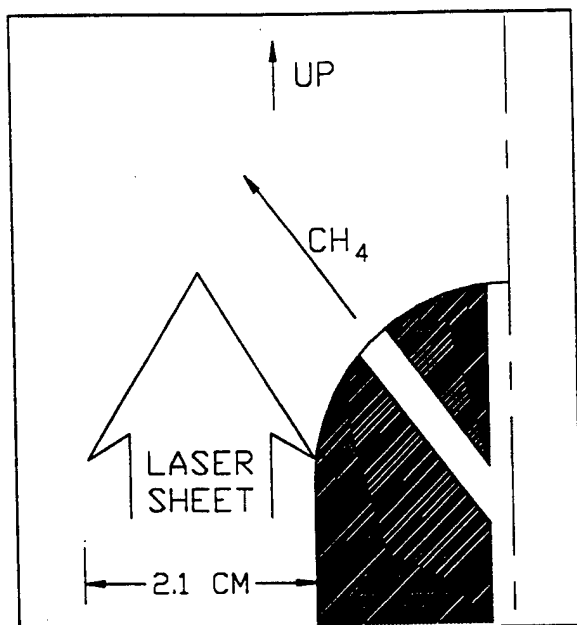
Figure 11: Calibration Flame Geometry combustor

Figure 12:Laminar diffusion flame

The dye laser was tuned to 431.5 nm and the output energy was typically around 6 mJ over 5 ns. The sheet was directed into the combustor and the signal imaged by the collection optics. A 9 nm bandwidth filter centered at 490 nm was used to filter the unwanted light, and the Princeton Instruments intensified camera was gated for a 50 ns shutter speed.

To estimate the amount of background signal collected, the camera was exposed to the imaged area while the laser pulse was blocked. No image was seen. This implied that the images collected were laser induced. The first image taken was that of a laminar methane flame shown in figure 12. The lower portion of the flame is believed to be CH fluorescence, while the upper portion of the flame appears to be contaminated with what is believed to be laser induced incandescence. This was determined by detuning the laser off of 431.5 nm and viewing the altered image. Further studies will be run to investigate the possibility of separating the two signals, and to determine exactly what they are.

Figure 13 shows a turbulent diffusion flame (attached) which clearly shows the fuel core and the neighboring reaction zone. Figure 14, shows a lifted turbulent diffusion flame. Definite flow structure can be seen for this flame.

Figure 11: Turbulent diffusion flame

6

Figure 14: Turbulent lifted diffusion flame

Summary

The flow fields observed in the four-inlet geometries have the intrinsic characteristic of diverting a substantial amount of the inlet fl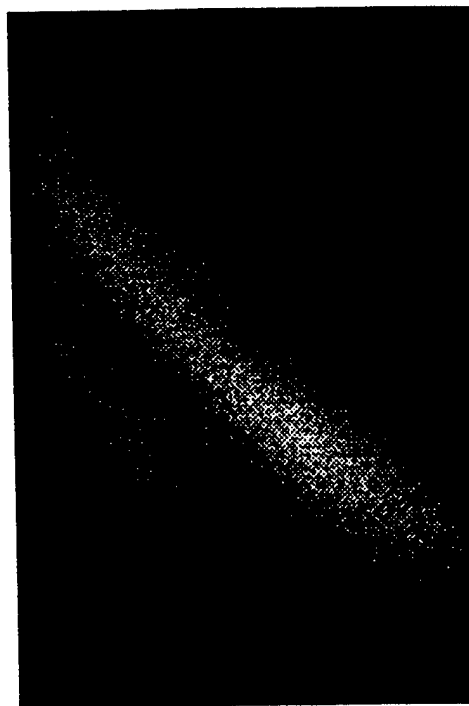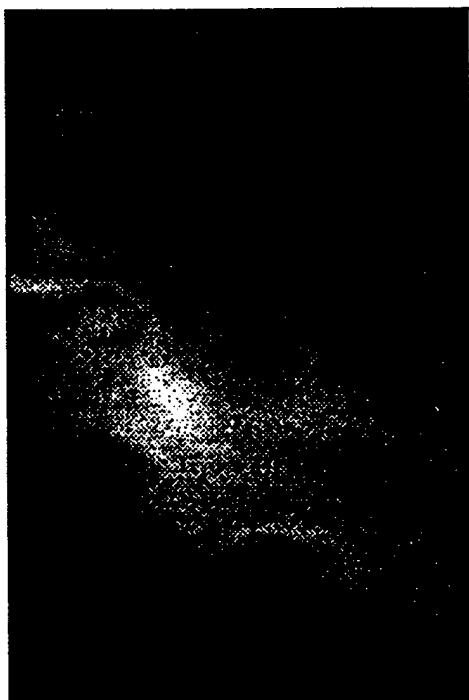ow into the dome region of the combustors resulting in two recirculation regions. Characteristics of the recirculation patterns and geometrical limitations resulted in preferred dome heights of 0.25D and 0.083D for the 90 and 60 degree combustors respectively. A preferred dome height was not found for the 45 degree combustor.

The 90° same-station combustor contained strong and stable recirculation zones both upstream and downstream of the inlet flow inlet locations. The upstream recirculation zone interacted with the off-axis fuel jets in two distinct patterns. It was seen that above a critical momentum ratio, the fuel jet "bent backwards" and followed a pattern dictated by the "inlet flow" flow resulting in one primary recirculation zone per jet. Once the momentum ratio was lowered below a critical momentum ratio, the same fuel jet impinged and penetrated the incoming inlet flow column resulting in two counter-rotating recirculation zones located on either side of the fuel jets. In between each of the "inlet flow" inlet columns existed two counter-rotating tubes aligned with the combustor axis. These tubes were believed to be the primary transport mechanisms responsible for transferring the dome region products to the aft combustor chamber.

The 60 degree same-station combustor contained similar flow structures as seen in the 90 degree same-

station combustor, but they were observed to be less organized and weaker in strength.

None of the 45 degree same-station combustors generated a favorable flow field. The shallow inlet flow-inlet angle resulted in directing most of the "inlet flow" momentum downstream, thereby greatly reducing the amount of mixing which occurred. This produced a fuel-rich dome head region. It is recommended that only inlet flow inlet angles of 60 degrees or greater be considered for application.

The preliminary combustion tests have begun to explore various diagnostic techniques for view the fuel and flame front distribution. Early results are promising, but higher signal levels will be needed for actual direct-connect testing. This requires that additional transition bands be explored in order that the best method may be employed. The possible detection of laser induced incandescence introduces a problem that must be addressed before further tests are made. Ideas for solving some of these problems are presented in the next section.

Future Work

Future work will include CH imaging by using a stronger transition band. Allen, M. et. al.[14] concluded that the maximum fluorescence signal could be obtained by exciting at 428 nm and observing the fluorescence at 431 nm. The only problem with this method is that a very narrow bandpass filter would be needed, and care must given to off-axis rays.

The camera gating sequence will also be reevaluated in order to guarantee the least amount of noise is introduced into the signal.

Finally, once a satisfactory experimental method is chosen, the optical combustor will be relocated to the Propulsion Directorate of the U.S. Army Missile Command for direct-connect testing.

References

1. Kennedy, J.B., 1974. Ramburner Flow Visualization Studies, *11th JANNEF Meeting*, CPIA Publication Number 261, pp. 415-440.
2. Chittilapilly, L.T., Venkateswaran, S., 1990. Flow Measurements in a Model Ramjet Secondary

Combustion Chamber, *Journal of Propulsion,* Vol. 6, No. 6, pp. 727-731.

3. Schadow, K.C., Chieze, D.J., 1981. Water Tunnel and Windowed Combustion as Tools For Ducted Rocket   Development, Vol. 2, *JANNEF Propulsion Mtg*, pp. 101-115.

4. Schetz, J.A., Hewitt, P.W., and Thomas, R., 1983. Swirl Combustor Flow Visualization Studies in a Water Tunnel, *Journal of Spacecraft*, Vol. 20, No. 6, pp. 574-582.

5.   Winter, E.F. , 1951. Flow Visualisation Techniques Applied to Combustion Problems, *Journal of the Royal Aeronautical Society*, Vol. 62, pp. 268-276

6. Hsieh, W.H., Yang, V., 1989. Measurement of flowfield in a simulated solid-propellant ducted rocket combustor using laser Doppler velocimetry, *25th Joint Propulsion Conference*, AIAA Paper No. 89-2789.

7. Reuter, D.M., Hegde, U.G., and Zinn, B.T., 1990. Flowfield Measurment in an Unstable Ramjet Burner, *Journal of Propulsion*, Vol. 6, No. 6, pp. 680-685.

8. Universal Energy Systems, Inc., 1983. Multi-Ducted Inlet Combustor Research and Development, *Interim Report for Period September 1982 - August 1983*, AFWAL-TR-83-2081.

9. Vanka, S.P., Craig, R.R., and Stull, F.D., 1984. Mixing, Chemical Reaction, and Flow Field Development in Ducted Rockets, *Progress Report*

10. Brophy, C. and Hawk, C., "Flow Visualization of Four-Inlet Ducted Rocket Engine Geometries", *Journal of Flow Visualization and Image Processing*, Exp. Fall '96.

11. Brophy, C. and Hawk, C., "A Flow Visualization Facility for Ducted Rocket Engine Mixing Studies", AIAA Paper No. 95-2934.

12. Namazian, M., et. al., Two-Wavelength Single Laser CH and CH₄ Imaging in a Lifted Turbulent 3597-3600

13. Allen, M., et. al., Digital Imaging of Reaction Zones in Hydrocarbon-Air Flames Using Planar Laser-Induced Fluorescence of CH and C₂, *Optics Letters*, Vol. 11, No. 3, pp. 126-128

14. Verdieck, J., et. al., Laser-Induced Saturated Fluorescence Investigations of CH, CN, and NO in Flames, *Eighteenth Symposium on Combustion*, 1981, pp. 1559-1566.
Garland, N., Crosley, D., Relative Transition

AIAA 95-2934

A Flow Visualization Facility for Ducted Rocket Engine Mixing Studies

Christopher M. Brophy and Clark W. Hawk
Propulsion Research Center
Department of Mechanical and Aerospace Engineering
University of Alabama in Huntsville
Huntsville, Alabama 35899

31st AIAA/ASME/SAE/ASEE
Joint Propulsion Conference and Exhibit
July 10-12, 1995/San Diego, CA

A Flow Visualization Facility for Ducted Rocket Engine Mixing Studies

Christopher M. Brophy* and Clark W. Hawk†
Propulsion Research Center
Department of Mechanical and Aerospace Engineering
University of Alabama in Huntsville, Huntsville, AL 35899

Abstract

A water flow visualization facility has been designed and constructed in order to investigate the mixing processes inside of four-inlet ducted rocket engines (DRE) with a variety of fuel injectors, flow rates, and geometries. The facility has the capability of monitoring and varying the flow rates through all five inlets of the combustor model and can produce overall flow rates up to 3213 liters per minute (850 gpm). Flow visualization was achieved by seeding the flow field with polystyrene spheres and illuminating them with laser sheet lighting. Images revealed complex mixing patterns within the dome head region of the combustors which were recorded with video and conventional photography.

Nomenclature

D = combustor model diameter
$\overline{U}$ = mean combustor velocity
h = dome height
x = axial location along combustor
$\dot{m}_a$ = mass flow of air
$\dot{m}_f$ = mass flow of fuel
$\dot{m}_a v_a$ = momentum of air
$\dot{m}_f v_f$ = momentum of fuel
Re_D = Reynolds number, UD/v

Introduction

Ducted rocket engine systems have recently received a revived interest due to their high specific impulse, throttlability, and resulting long range capabilities. They obtain the high specific impulse capabilities. They obtain the high specific impulse by ducting the air in which they fly through inlet ducts and using it as the oxidizer when mixed with a fuel-rich gas from a gas generator. The mixture combusts and is then accelerated through a converging/diverging nozzle to generate thrust. A diagram showing the general layout of a DRE is shown in figure 1.

The majority of the research performed in the past on ducted rocket engines has been with one- and two-inlet engine geometries. These geometries have often been investigated using flow visualization with water[1-5] for qualitative information on the general flow field and direct-connect testing[6-9] for quantitative results. The facility constructed at The University of Alabama in Huntsville (UAH) is being used to study different mixing scenarios for four-inlet ducted rocket engine geometries through flow visualization with water. The effects of air inlet angle, air inlet location, air/fuel mass ratios, air/fuel momentum ratios, dome height, and injector performance are being investigated over a wide operational range. By allowing for such a wide range of operating parameters, much of the engine's flight envelope may be simulated, thereby allowing the investigation of flame holding and auto ignition potential of the various geometries over most of the operational range. Information gained from the qualitative work performed in the flow visualization facility will be used in the design of an optically accessible sub-scale combustor to be used in direct-connect testing with methane as a fuel simulant.

Facility Description

The water flow visualization facility has overall dimensions of 6 meters by 4.6 meters (20'x15'), and is located on the UAH campus. A top view of the facility showing the overall layout is shown in figure 2. Not shown in the figure are the 3780 liter (1000 gallon) reservoir tank and the centrifugal pump located below the deck. The power plant for the facility is the 30 hp variable RPM centrifugal pump capable of delivering 3080 liters per minute (815 gpm) at 206 kPa (30 psi) to the combustor model. This pump is designed to deliver a high volume at low pressure and is used to supply water for use as

Figure 1: A ducted rocket engine schematic

Figure 2: Flow visualization facility layout

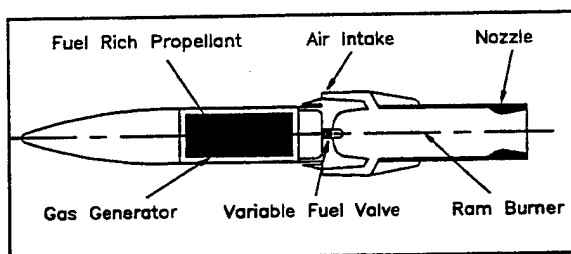**Figure 3:** The dome head and fuel injector installed in the 90° same-station combustor;w/injector details

the "air" source for the combustor. A supplemental 517 kPa (75 psi) water supply arm is used to deliver the water for the "fuel" source at up to 132 liters per minute (35 gpm). The amount of water delivered to the model is controlled both by the pump RPM and by throttling the supply arms with globe valves. A PC is used to monitor the Blancett W1120 flow meters used on each inlet, two pressure transducers, and provide external pump control if desired.

The combustor models are placed inside a 91cm x 122cm x 61cm viewing tank which contains water to minimize refraction effects. The inlet arms of each model interface with the supply arms by PVC unions which allow for quick connect/disconnect. The fuel arm is connected with the rear of the dome head with a section of PVC and two Fernco couplings. The dome head, shown in figure 3, is a hemispherical piston head with O-rings that contains the fuel injector and is permitted at any axial location in the front end of each combustor. The dome height is defined as the axial distance between the air inlet dump station and the lip of the dome head. It may be adjusted by varying the PVC length between the Fernco couplings. Different fuel injector designs may be installed into the dome head by simply loosening two allen screws and substituting the new core into a 5 cm diameter receptacle and retightening the screws.

Visualization of the flow field is achieved by either seeding the fuel jet or the air jets with 0.0254 cm (0.010") polystyrene spheres. Seeding of the fuel jet is accomplished by pressuring a highly seeded bath of the spheres and bleeding them into the fuel arm through a gate valve. This method produces the best tracking of the fuel distribution. The air jets can be seeded by simply placing the beads into the large reservoir up to a 10^5 particles/m^3 density. The fuel jet is then left unseeded, but does illuminate well due to cavitation of the fuel stream after experiencing the pressure drop of the injector. The latter method appears to work best for long duration testing. A 5 watt Argon Ion laser is used to illuminate the polystyrene spheres and air bubbles. The laser
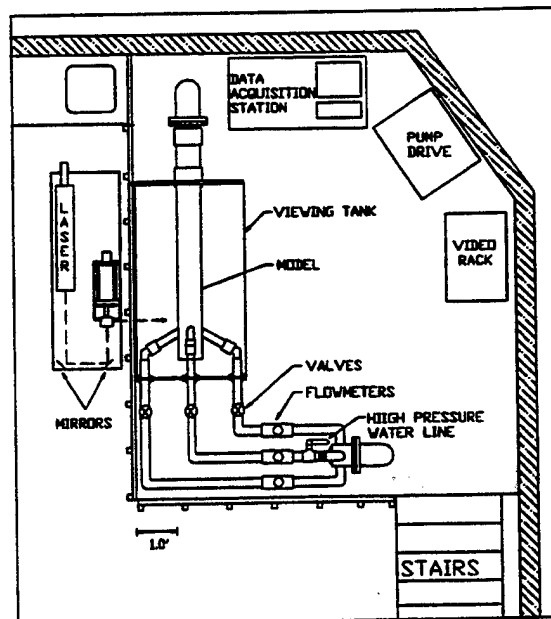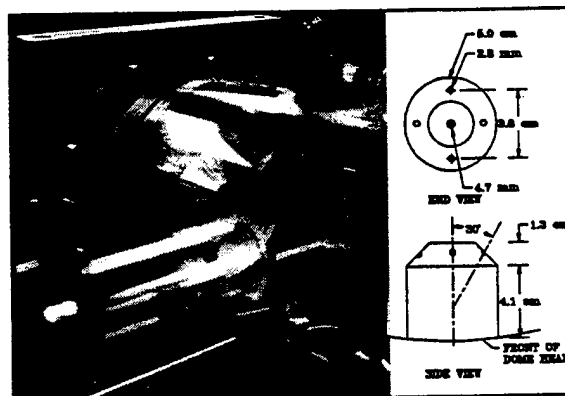
output is first focused and then expanded through a cylindrical lens to produce a light sheet approximately 1.5 mm thick. The sheet may be oriented either vertically or horizontally and its location controlled by moving the sheet lighting assembly with a stepper motor. The images are then recorded on both Hi8 video tape and by conventional photography.

Initial Results

The facility has evaluated 3 of the 6 chosen ducted rocket engine combustors, each having an inner diameter of 15.24 cm (6"). The combustors evaluated to date are the 45, 60, and 90 degree same-station inlet combustors shown below in figure 4.

Parameter	Range
Mass flow ratios	$10 \leq \dfrac{\dot{m}_a}{\dot{m}_f} \leq 60$
Momentum ratios	$0.05 \leq \dfrac{\dot{m}_a v_a}{\dot{m}_f v_f} \leq 20.0$
Dome height	$0 \leq d_h \leq 20.0\,cm$
Air inlet angles	45°, 60°, and 90°
Fuel injectors	Limited to a 5 cm diameter

All have been investigated up to a Reynolds number of 5.5×10^5 and over the range of mass and momentum ratios described in the facility description section.

The flow field for the 90 degree same-station combustor produced an apparently fuel-rich region between the dome head and the inlet dump station for most of the flow rates. Although this region did have recirculation, the apparent lack of "air" indicates that this inlet dump configuration is not ideal. Figure 5 shows the flow field behavior for the 90 degree same-station dump combustor for three different flow rate conditions. The photographs are of sheet lighting along the combustor axis at mid plane. The bottom picture in figure 5 is for a Reynolds number of 2.2×10^5, a mass flow ratio of 25.0, and a dome height of 7.00 cm. There is evidence that the fuel jet is penetrating the stagnation point of the four "air" jets and generating significant mixing after the dump station. The problem still remains of the apparently fuel rich region in the front end of the combustor which would likely lead to flame extinction once the rich limit is reached.

The 60 degree combustor generated a pair of stable counter-rotating regions on each side of the angled fuel jets. The recirculation regions existed for dome heights up to 0.75D. Dome heights greater than this value produced regions which became unstable and periodic. The evidence of increased "air" in the dome head region implies a more suitable combustion mixture thereby improving flame holding and auto-ignition characteristics. Figure 6 shows the 60 degree combustor with three mass flow ratios. Notice that the center fuel jet appears to penetrate the stagnation point of the "air" inlets for the lower mass flow ratio.

The 45 degree same-station combustor appeared to have similar but weaker recirculation zones than the 60 degree same-station combustor. This is most likely due to the amount of momentum introduced normal to the combustor axis by the "air" inlets. The reduced amount of momentum normal to the combustor axis obviously reduces the amount of mixing that occurs between the "fuel" and "air" jets, therefore increasing the necessary combustor length for complete combustion. The center fuel jet appears to penetrate the "air" jets more easily than the other combustors, which is expected. There also appears to be a larger "slow" zone around a fast moving core downstream of the air inlet station for this combustor, emphasizing the reduced amount of mixing for this configuration.
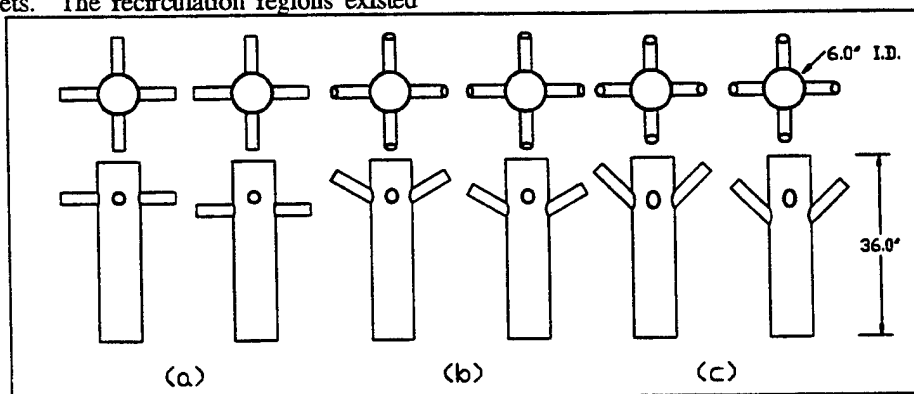
Figure 4: Ducted rocket engine model combustors with various air injection geometries
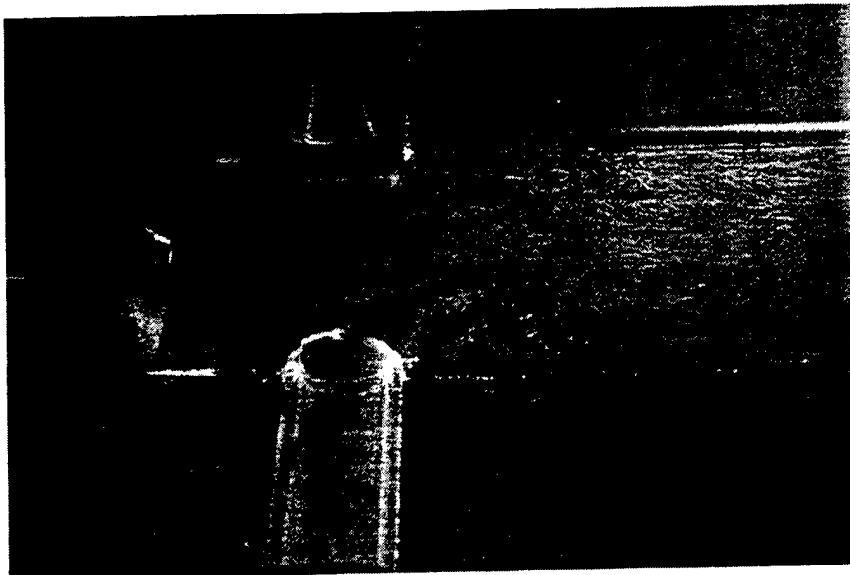
$\overline{U} = 1.139$ m/s
$\mathrm{Re}_D = 2.17 \times 10^5$
$\dot{m}_a / \dot{m}_f = 37.5$
$\dot{m}_a v_a / \dot{m}_f v_f = 16.32$
h= 7.00 cm
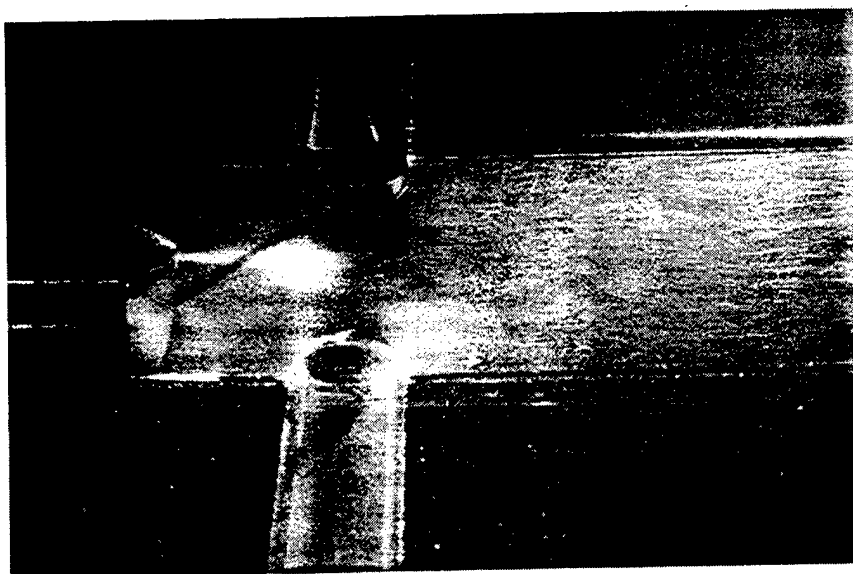
$\overline{U} = 1.146$ m/s
$\mathrm{Re}_D = 2.18 \times 10^5$
$\dot{m}_a / \dot{m}_f = 30.0$
$\dot{m}_a v_a / \dot{m}_f v_f = 10.44$
h= 7.00 cm
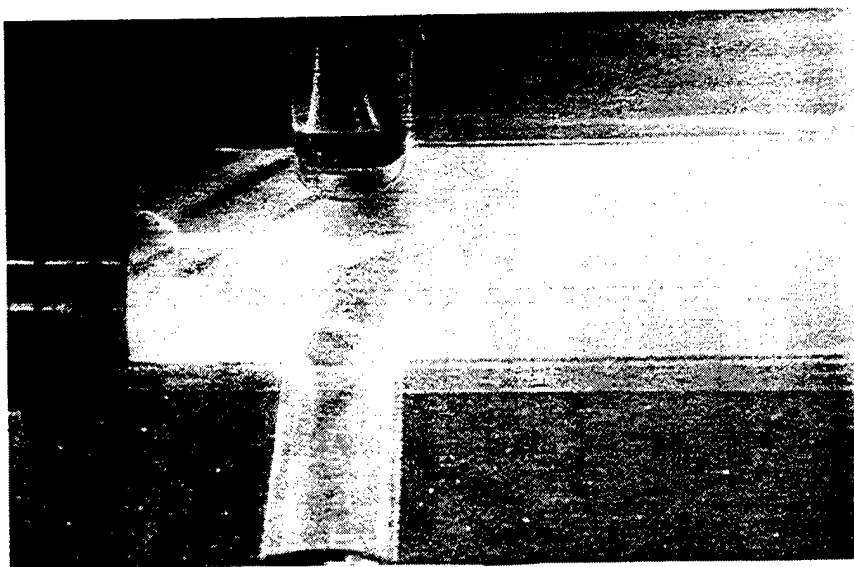
$\overline{U} = 1.154$ m/s
$\mathrm{Re}_D = 2.20 \times 10^5$
$\dot{m}_a / \dot{m}_f = 25.0$
$\dot{m}_a v_a / \dot{m}_f v_f = 7.25$
h= 7.00 cm

Figure 5: 90° same-station combustor flow field at different fuel flow rates

$$\overline{U} = 1.139 \text{ m/s}$$
$$Re_D = 2.17 \times 10^5$$
$$\dot{m}_a / \dot{m}_f = 30.0$$
$$\dot{m}_a v_a / \dot{m}_f v_f = 7.25$$
$$h = 4.00 \text{ cm}$$
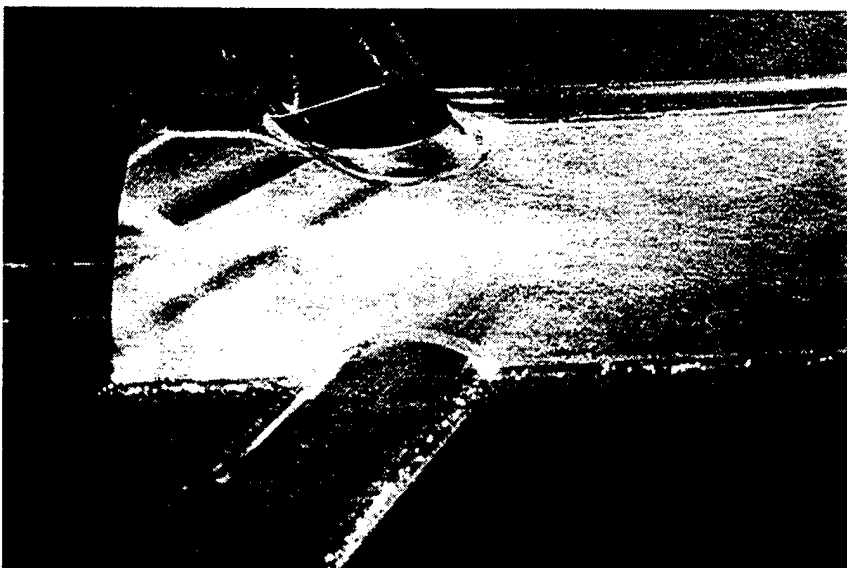
$$\overline{U} = 1.146 \text{ m/s}$$
$$Re_D = 2.18 \times 10^5$$
$$\dot{m}_a / \dot{m}_f = 30.0$$
$$\dot{m}_a v_a / \dot{m}_f v_f = 10.44$$
$$h = 4.00 \text{ cm}$$
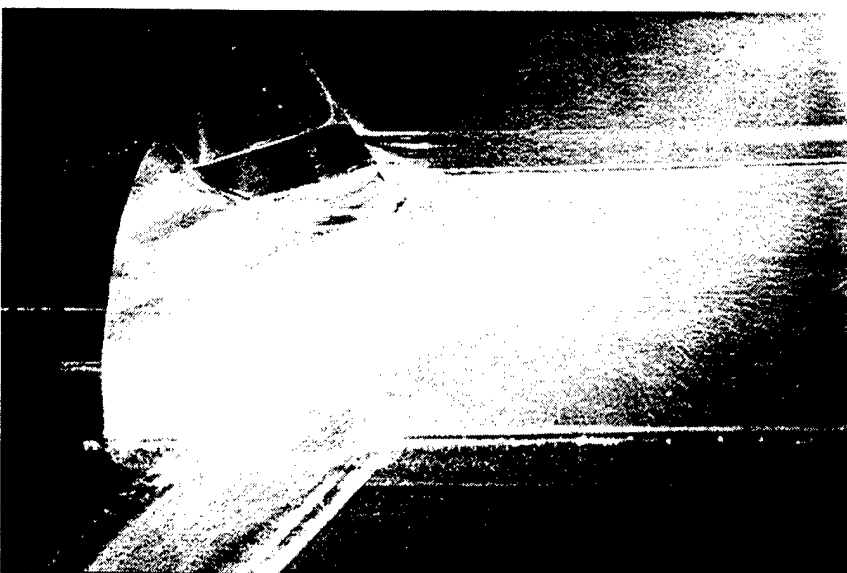
$$\overline{U} = 1.154 \text{ m/s}$$
$$Re_D = 2.20 \times 10^5$$
$$\dot{m}_a / \dot{m}_f = 25.0$$
$$\dot{m}_a v_a / \dot{m}_f v_f = 7.25$$
$$h = 4.00 \text{ cm}$$

Figure 6: 60° same-station combustor flow field at different fuel flow rates

$\overline{U}$ = 1.139 m/s
Re_D= 2.17 x 10^5
$\dot{m}_a / \dot{m}_f$ = 37.5
$\dot{m}_a v_a / \dot{m}_f v_f$ = 7.25
h= 3.00 cm
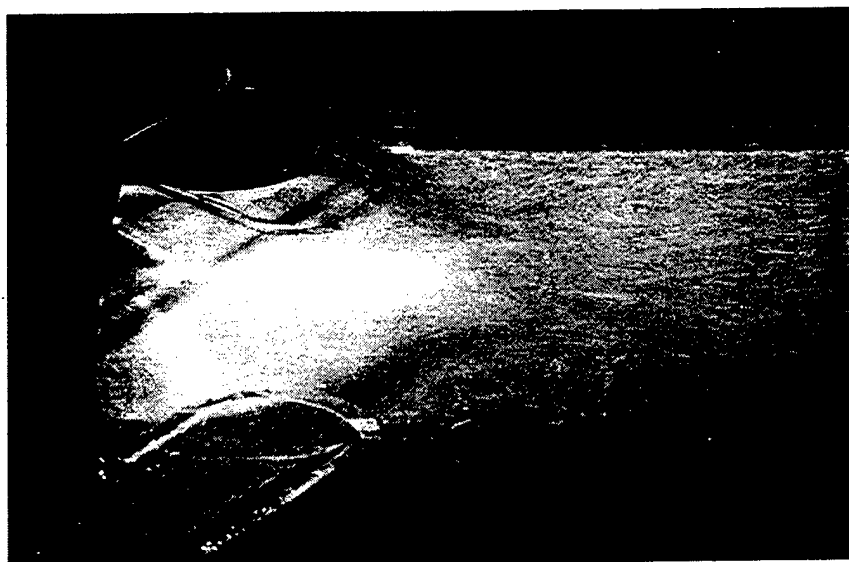
$\overline{U}$ = 1.146 m/s
Re_D= 2.18 x 10^5
$\dot{m}_a / \dot{m}_f$ = 30.0
$\dot{m}_a v_a / \dot{m}_f v_f$ = 10.44
h=3.00 cm

$\overline{U}$ = 1.154 m/s
Re_D= 2.20 x 10^5
$\dot{m}_a / \dot{m}_f$ = 25.0
$\dot{m}_a v_a / \dot{m}_f v_f$ = 16.32
h= 3.00 cm

Figure 7: 45° same-station combustor flow field at different fuel flow rates

0.5 cm upstream of air inlets

0.5 cm off injector face
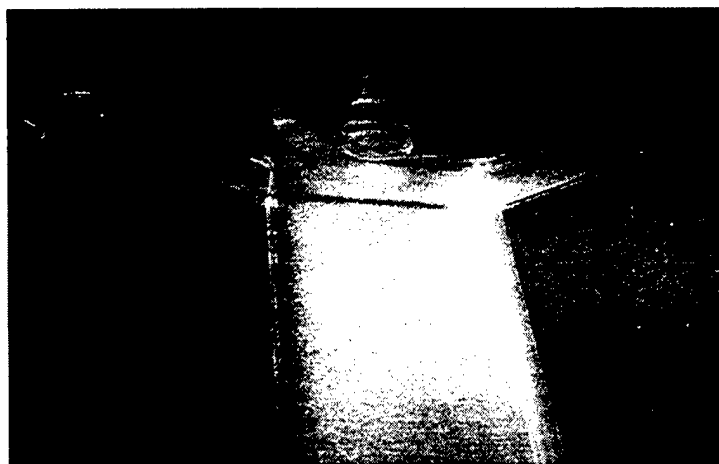
Overhead view

Figure 8: Other combustor viewpoints

Summary

The performance and initial results from the ducted rocket engine flow visualization facility indicate that it will be extremely valuable in contributing to the DRE research program underway at UAH. The information provided by the various seeding and laser lighting techniques yielded insight into possible combustor characteristics such as flame holding and auto ignition characteristics.

The seeding of the "air" inlets with polystyrene spheres and allowing the "fuel" injector to cavitate produced an easily visualized flow field. The viewing tank constructed for the models worked exceptionally well at minimizing refraction effects, therefore allowing acceptable viewing, photographing, and video recording of the combustor flow fields.

The conclusions reached from work performed with the facility will be used in choosing the geometry of the optically accessible combustor to be constructed for direct-connect testing. Results from the direct-connect test will provide valuable information about the mixing, flame holding, and auto-ignition properties of ducted rocket engines over a wide operating range while revealing the validity of using flow visualization to gain insight into four-inlet DRE combustor flow fields.

References

1) Winter, E.F. ,"Flow Visualisation Techniques Applied to Combustion Problems," *Journal of the Royal Aeronautical Society*, Vol. 62, pp. 268-276.

2) Kennedy, J.B., "Ramburner Flow Visualization Studies," 11th JANNEF Meeting, Sept. 1974, pp. 415-440, CPIA Publication Number 261.

3) Schadow, K.C., Chieze, D.J., "Water Tunnel and Windowed Combustion as Tools For Ducted Rocket Development," JANNEF Propulsion Mtg, Vol. 2, 1981, pp. 101-115.

4) Schetz, J.A., Hewitt, P.W., and Thomas, R., "Swirl Combustor Flow Visualization Studies in a Water Tunnel," *Journal of Spacecraft*, Vol. 20, No. 6, 1983, pp. 574-582.

5) Universal Energy Systems, Inc., "Multi-Ducted Inlet Combustor Research and Development," Interim Report for Period September 1982 - August 1983, AFWAL-TR-83-2081.

6) Chittilapilly, L.T., Venkateswaran, S., "Flow Measurements in a Model Ramjet Secondary Combustion Chamber," *Journal of Propulsion,* Vol. 6, No. 6, Nov.-Dec. 1990, pp. 727-731.

7) Hsieh, W.H., Yang, V., "Measurement of flowfield in a simulated solid-propellant ducted rocket combustor using laser Doppler velocimetry," 25th Joint Propulsion Conference, AIAA Paper No. 89-2789.

8) Reuter, D.M., Hegde, U.G., and Zinn, B.T., "Flowfield Measurment in an Unstable Ramjet Burner," Journal of Propulsion, Vol. 6, No. 6, pp. 680-685.

9) Vanka, S.P., Craig, R.R., and Stull, F.D., "Mixing, Chemical Reaction, and Flow Field Development in Ducted Rockets," Progress Report, September 1984.

Ducted   Rocket   Engine   Research

MICOM   Contract   No.   DAAH01-93-R326

The MICOM Ducted Rocket Engine Research Program is divided into the following task with the assigned personnel as shown:

Task 1.0 **Ballistic Properties of Booster Propellant Candidates** with Dr. Robert A. Frederick, Jr. as P.I. assisted by Mr. Brian Greiner, GRA.

Task 2.0 **Benchtop Erosion Simulator** has been delayed due to reduced funding.

Task 3.0 **Solid Fuel-Gas Generator Fuel Candidates Ignition and Combustion Characteristics** with Dr. Douglas Feikema as P.I. assisted by Mr. John Dempsey, GRA.

Task 4.0 **Ducted Rocket Engine Critical Test Parameters Identification** with Dr. Hugh Coleman as P.I. assisted by Mr. John Blevins, GRA.

Task 4.2 **Verification of Critical Parameters Through Flow Visualization** with Dr. Clark Hawk as P.I. assisted by Mr. Chris Brophy, GRA.

Task 5.0 **Program Management and Support** with Dr. Clark Hawk as Program Director assisted by Ms. Linda Marion, Administrative Assistant

This fifth quarterly report contains a overall program management summary followed by detailed discussions of accomplishments and plans for the technical tasks in numerical order.

AIAA

AIAA 95-3085
Labscale Hybrid Uncertainty Analysis

B. Greiner and R. A. Frederick, Jr.
Propulsion Research Center
University of Alabama in Huntsville
Huntsville, AL 35899

AIAA/SAE/ASME/ASEE
31th Joint Propulsion
Conference and Exhibit
July 10-12, 1995 / San Diego, CA

Labscale Hybrid Uncertainty Analysis

B. Greiner[*] and R. A. Frederick, Jr.[†]

Propulsion Research Center, University of Alabama in Huntsville
Huntsville, Alabama 35899

Abstract

A past investigation by The University of Alabama in Huntsville Propulsion Research Center into the mechanisms of hybrid rocket instability led to a detailed experimental uncertainty analysis of a labscale hybrid motor used in the study. This uncertainty analysis was carried out to determine the quality of the experimental data obtained from the labscale device and the applicability of labscale hybrid testing in general. In particular, calculations of the uncertainties in the measurements of fuel regression rate, oxidizer flux, motor characteristic velocity, and the oxidizer-to-fuel mass ratio were made. These calculations were performed using the accepted methodology of Coleman and Steele.

The results showed that the typical uncertainties in the measurements of the fuel regression rate ($\pm8.7\%$), oxidizer flux ($\pm10.8\%$), motor characteristic velocity ($\pm10.5\%$), and the oxidizer-to-fuel mass ratio ($\pm9.2\%$) were relatively high, thus limiting the use of the labscale hybrid motor for quantitative investigations. The uncertainty levels were dominated by 1) high measurement uncertainties in the diameters of the initial fuel grain initial port and the nozzle throat, 2) a large conceptual bias in the burn duration, 3) a conceptual bias in the average chamber pressure, and 4) a high precision uncertainty showing low repeatability of some results. These high levels of uncertainty lead to limited utility of labscale data in the generation regression rate/oxidizer flux curve fits and to low resolution in the determination of characteristic velocity efficiency.

Methods that were identified to reduce the level of uncertainty in the data reduction results were to: 1) increase the scale of the test motor, reducing the uncertainties in the measurements of the diameters of the fuel grain port and nozzle throat; 2) increase the burn duration, which would reduce the domination of the burn duration conceptual bias; and 3) reduce the uncertainty in the average chamber pressure measurement through either an increase in the test pressure or in the accuracy of the calibration methodology, both of which were believed to have questionable or limited effectiveness. A parametric study of these changes is recommended to determine the magnitude of expected improvements in the accuracy.

Nomenclature

B_α = bias (fixed) uncertainty in parameter α
C^* = characteristic velocity
C_d = metering venturi discharge coefficient
D_i = initial fuel grain port diameter
D_{th} = throat diameter of motor nozzle
D_{vent} = throat diameter of metering venturi
G_{ox} = gaseous oxygen mass flux
ℓ = Aft mixing section length
L = fuel grain total length
Δm = change in fuel grain mass
m_i = initial mass of fuel grain
m_f = final mass of fuel grain
$O\!/\!F$ = mass ratio of oxidizer to fuel
P_α = precision (random) uncertainty in α
P_c = average chamber pressure
P_{up} = average pressure upstream metering venturi
Δr = change in fuel grain port radius
$\dot{r}$ = average fuel regression rate
R = gas constant for oxygen
Δt = change in time
t_i = ignition time
t_f = shutdown time
T_{up} = average temperature upstream of venturi
U_α = total uncertainty in component α
x_i = test input parameter

Greek

γ = specific heat ratio for oxygen
μ = mean value
π = pi, 3.141592654...
ρ_f = density of solid fuel component
σ = standard deviation

Introduction

In order to reduce the cost and complexity of experimental programs quite often experimenters choose to use subscale or labscale test rigs in place of full-scale testing. From these labscale tests, data are retrieved in order to gain more information about the basic operational phenomenea and physics. This methodology has been widely applied in the area of propulsion testing for the past fifty years. However, until recently, little more than afterthought has been given to the experimental uncertainty of the data from which any empirical correlations are made. This is particularly the case with labscale testing surrounding hybrid rocket motors.[1]

A test program conducted by The University of Alabama in Huntsville Propulsion Research Center into the mechanisms of hybrid rocket instability led

---

* Graduate Research Assistant, AIAA Student Member
† Assistant Professor, Mechanical and Aerospace Engineering, Senior Member AIAA

to a detailed experimental uncertainty analysis of a labscale hybrid motor used in the investigation.[2] The primary purpose of the uncertainty analysis was to determine the quality of the experimental data obtained from the labscale device. However, the results of the analysis were also used to make a determination of the overall applicability of labscale hybrid testing. In the process, several key parameters were identified which dominated the uncertainties in the data reduction equations. This paper details the experimental uncertainty analysis that was performed on the Labscale Hybrid Motor (LHM) by describing: 1) the experimental motor hardware and data acquisition system, 2) the development of the data reduction and uncertainty equations, and 3) the analysis of the results from these equations. This will suggest parametric study of the key data reduction parameters to identify the optimum test conditions for the highest quality hybrid data.

Experimental Setup

Motor Hardware

The LHM hardware consisted of a forward closure, a grain holder, and an aft closure, as shown in Figure 1. A gaseous oxygen feed system was connected to the motor at the forward closure. The grain holder surrounds cartridge loaded fuel grains which are held in place by a retaining washer at each end of the grain holder. The aft mixing section consisted of an aft closure and a carbon insert surrounding a tungsten nozzle. The LHM offered flexibility in selecting various lengths of aft mixing section, ℓ in Figure 1, different nozzle diameters, and different grain lengths.

During operation of the LHM, gaseous oxygen was injected in the forward end of the motor and diffused by the forward closure diffuser screen. The gaseous oxygen flow rate was controlled by a dome-loaded pressure regulator upstream of a metering venturi. After a 10-second oxygen pre-flow, a current applied to a squib in the forward closure ignited the fuel. After a burn time of approximately two seconds, the oxygen flow was terminated and a nitrogen purge-flow was initiated to ensure complete extinguishment of the fuel surface. Short burn times were used due to the thermal limits of the uncooled tungsten nozzles used for these experiments.

The primary type of fuel were used in the test firings was hydroxyl-terminated polybutadiene (HTPB). Standard operating procedure called for four grains which were cartridge loaded in the fuel grain holder. Each grain was nominally 2.5 inches long, had a 0.820-inch diameter port, and a 1.375-inch outer diameter. The HTPB(R-45)/N-100 fuel grains ($C_{6.939}H_{9.855}N_{0.178}O_{0.264}$) were mixed and cast under a vacuum in phenolic sleeves. The castings were then cured for 24 hours at 140 °F.

Data Acquisition System

The instrumentation used for the LHM experiments supplied data on the motor pressures, temperatures, and oxygen flow rate. Forward and aft pressure transducers were used to measure the pressures inside the motor. The pressure and temperature of the incoming oxygen were measured upstream of a choked metering venturi to determine the oxidizer mass flow rate. The various measurements were recorded on a digital system (0-40 Hz) and on an analog FM tape system.

The motor chamber pressure data were obtained from the test analog data recordings. The analog data was passed through a 5 kHz low-pass anti-aliasing filter and then digitized at 10 kHz. This high-frequency data was calibrated using the low-frequency data since the calibration techniques used on the NASA/MSFC analog system were found to be unacceptable. Instead, a technique of calibration was selected which consisted of selecting two pairs of corresponding points from the high frequency data (voltage-time) and the low frequency data (pressure-time) from which a linear calibration curve was constructed. The technique of calibrating using the low frequency data introduced a ±10 psia bias uncertainty into the high frequency data due to the scatter of the high frequency data at the calibration points. This data was used for qualitative visual analysis as well as for digital analysis of the frequency content through the use of Fast Fourier Transform (FFT) techniques. The motor operating times were also determined from the high-frequency digital data. A precision balance was used to weigh each fuel grain pre- and post-test in order to determine the average regression rate.
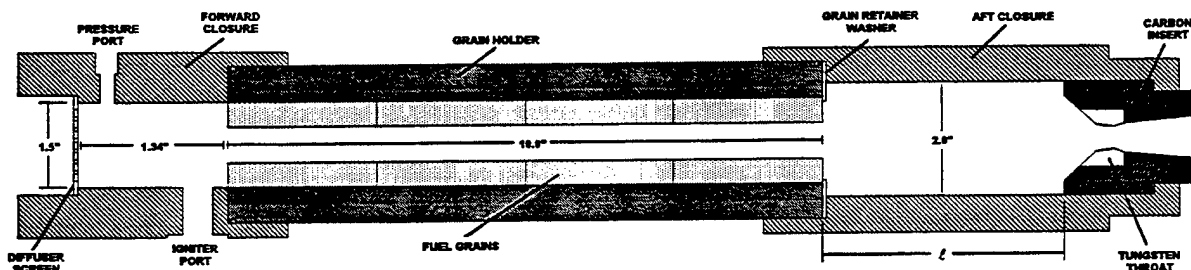

Figure 1. Sketch of Thiokol/UAH/MSFC LHM Layout.

Analysis of Labscale Uncertainty

Using methods established by Coleman and Steele,[3] an experimental uncertainty analysis was performed to determine the uncertainty in the experimental results and to determine the important data reduction parameters in LHM testing. This also enabled an evaluation of the overall applicability of LHM testing. The basic uncertainty technique consists of determining the sensitivity of the data reduction equations to each input parameter, multiplying by the parameter bias limit, calculating the precision limit from the standard deviation of the test data, and combining these values in a root-sum-square form to determine overall uncertainty. In order to carry out this analysis, the equation for the experimental value of interest must be written *explicitly* in terms of measurable or input parameters. The development and results of these calculations are shown in the following sections for all the data reduction equations.

Reduction of Data

Test data were reduced to determine the actual oxygen mass flux (G_{ox}), average fuel burning rate ($\dot{r}$), characteristic velocity (C^*), and oxidizer-to-fuel ratio (O/F) during each test. The following equations express each of these results in terms of data measured from each test. The full development of the data reduction equations used in this paper are detailed in Reference 4.

The oxidizer mass flux G_{ox} was determined from measurements of the average temperature (T_{up}) and pressure (P_{up}) upstream of the oxygen venturi, and the initial and final propellant mass (m_i and m_f):

$$G_{ox} = \frac{2C_d P_{up} D_{vent}^2 \gamma \sqrt{\left[\dfrac{2}{\gamma+1}\right]^{\gamma+1/\gamma-1}}}{\left(\dfrac{4(m_i - m_f)}{\pi \rho_f L} + 2D_i^2\right)\sqrt{\gamma R T_{up}}} \quad (1)$$

where L is the length of the fuel grain, D_i is the initial grain port diameter, ρ_f is the solid fuel density, C_d is the venturi discharge coefficient, and D_{vent} is the venturi throat diameter. The ideal gas constant (R) and ratio of specific heats (γ) are for oxygen.

For the calculation of regression rate, the mass consumption was assumed to occur evenly only over the fuel grain bore surface during the firing. This assumption is reasonable because of the short burn times used in this investigation but under the additional assumption that the ignition and shutdown transients were small compared to the burn times.

This leads to the following equation for the average regression rate:

$$\dot{r} \approx \frac{\Delta r}{\Delta t} = \frac{\sqrt{\dfrac{4(m_i - m_f)}{\pi \rho_f L} + D_i^2} - D_i}{2(t_f - t_i)} \quad (2)$$

where t_i and t_f are the ignition and shutdown times.

In studies of instabilities it is sometimes useful to examine combustion efficiency. This may be accomplished by dividing the actual motor characteristic velocity C^* by the theoretical C^* at the same actual O/F ratio. The overall O/F ratio in this investigation was found by taking the ratio of the oxidizer and fuel mass flow rates. This leads to the equation for the O/F ratio of:

$$O/F = \frac{\overbrace{C_d P_{up} \pi D_{vent}^2 \gamma \sqrt{\left[\dfrac{2}{\gamma+1}\right]^{\gamma+1/\gamma-1}} \Big/ 4\sqrt{\gamma R T_{up}}}^{\text{oxidizer mass flow rate}}}{\underbrace{(m_i - m_f) \Big/ (t_f - t_i)}_{\text{fuel mass flow rate}}} \quad (3)$$

The expression for the motor characteristic velocity was developed from the definition of C^* which is the product of the average chamber pressure (P_c) and the nozzle throat area, divided by the total mass flow rate. This leads to the final data reduction equation:

$$C^* = \frac{P_c \overbrace{\dfrac{\pi}{4} D_{th}^2}^{\text{throat area}}}{\underbrace{\dfrac{C_d P_{up} \pi D_{vent}^2 \gamma \sqrt{\left[\dfrac{2}{\gamma+1}\right]^{\gamma+1/\gamma-1}}}{4\sqrt{\gamma R T_{up}}}}_{\text{oxidizer mass flow rate}} + \underbrace{\dfrac{m_i - m_f}{t_f - t_i}}_{\text{fuel mass flow rate}}} \quad (4)$$

Generalized Uncertainty Analysis

The first phase of an uncertainty analysis is the development of expressions for the values of interest from the data reduction equations. For brevity, the following expressions for the experimental uncertainty of the LHM are detailed using the gaseous oxidizer flux, Equation (1), as an example. These uncertainty expressions can then be examined to determine the critical or dominant test parameters.

First, the basic equation for the uncertainty must be considered. For G_{ox}, the generalized uncertainty equation is written:

$$U_{G_{ox}} = \sqrt{B_{G_{ox}}^2 + P_{G_{ox}}^2} \quad (5)$$

where $B_{G_{ox}}$ represents the total bias or *fixed* uncertainty limit in G_{ox} which includes the contributions to the overall uncertainty that are constant from test to test. $P_{G_{ox}}$ represents the precision or *random* uncertainty limit for G_{ox} which is the contribution due to the statistically random "scatter" in the data. The concepts of $B_{G_{ox}}$ and $P_{G_{ox}}$ are best demonstrated by the illustration shown in Figure 2.
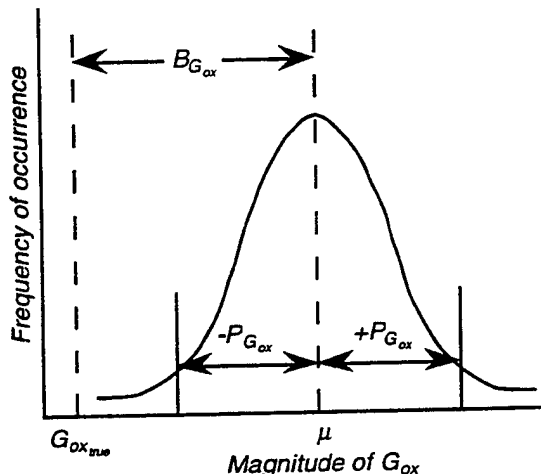

Figure 2. Illustration of Bias and Precision Uncertainty Limits.

Figure 2 shows a Gaussian distribution of flux readings centered about a point offset from the true value of G_{ox} by an amount equal to the bias limit $B_{G_{ox}}$. The methodology used to determine the bias limit is discussed in the following paragraphs. The precision limit $P_{G_{ox}}$ is found by determining the standard deviation, or σ, of the data about the mean value μ at a single set point and then doubling it to obtain the 95% confidence or "2σ" interval. This is the limit within which one can be confident that 95% of the readings will lie. For this investigation, the scatter in results from test to test was considered to be due to slight uncontrollable differences in test parameters such as the venturi upstream pressure and temperature. This scatter is trapped into the precision limit estimate by calculating the value of σ for the test data.

In order to calculate the bias limit for G_{ox}, one must determine how the uncertainty of each input parameter propagates into the bias limit. As stated earlier, this is accomplished by first writing the data reduction equation for the result of interest explicitly in terms of *measurable* input parameters. The data reduction equation for G_{ox} is repeated here for convenience:

$$G_{ox} = \frac{2C_d P_{up} D_{vent}^2 \gamma \sqrt{\left[\frac{2}{\gamma+1}\right]^{\gamma+1/\gamma-1}}}{\left(\frac{4(m_i - m_f)}{\pi \rho_f L} + 2D_i^2\right)\sqrt{\gamma R T_{up}}} \quad (1)$$

In examining Equation (1), it is seen that the input parameters are: C_d, P_{up}, D_{vent}, γ, m_i, m_f, ρ_f, L, D_i, and T_{up}. From Reference 3, the expression for the propagation of the bias uncertainties of the data reduction equation input parameters x_i into G_{ox} is written:

$$B_{G_{ox}} = \sqrt{\sum_i \left(\frac{\partial G_{ox}}{\partial x_i} B_{x_i}\right)^2} \quad (6)$$

where the partial derivative term is simply the sensitivity of G_{ox} to parameter x_i and is determined for each parameter from the basic data reduction equation for G_{ox}. Equation (6) has the additional assumption that correlated biases between parameters, if they exist, are negligible. Expanding Equation (6) using Equation (1):

$$
\begin{aligned}
B_{G_{ox}}^2 &= \left(\frac{\partial G_{ox}}{\partial C_d} B_{C_d}\right)^2 + \left(\frac{\partial G_{ox}}{\partial P_{up}} B_{P_{up}}\right)^2 + \left(\frac{\partial G_{ox}}{\partial D_{vent}} B_{D_{vent}}\right)^2 \\
&+ \left(\frac{\partial G_{ox}}{\partial \gamma} B_\gamma\right)^2 + \sum_{j=1}^4 \left(\frac{\partial G_{ox}}{\partial m_i} B_{m_{i_j}}\right)^2 + \sum_{k=1}^4 \left(\frac{\partial G_{ox}}{\partial m_f} B_{m_{f_k}}\right)^2 \\
&+ \left(\frac{\partial G_{ox}}{\partial \rho_f} B_{\rho_f}\right)^2 + \left(\frac{\partial G_{ox}}{\partial L} B_L\right)^2 + \left(\frac{\partial G_{ox}}{\partial D_i} B_{D_i}\right)^2 \\
&+ \left(\frac{\partial G_{ox}}{\partial T_{up}} B_{T_{up}}\right)^2
\end{aligned} \quad (7)
$$

Note that for the fuel grain mass terms a summation is included to account for the bias limits in the individual fuel grains.

An indication of the relative importance of each input parameter can be determined by conducting a "zero-order" uncertainty analysis. In this analysis the precision uncertainties are neglected and the bias uncertainties in the individual parameters are assumed to be 1% of the nominal parameter value. The partial derivatives were calculated to determine the parameter sensitivities. Due to the relative complexity of the data reduction equations, a finite differencing technique was used to approximate these derivatives. These calculations were carried out for each test and each data reduction equation using a spreadsheet utility. Table 1 shows the results of these calculations for the individual G_{ox} parameters on a nominal HTPB test.

Table 1. Zero-Order Uncertainty Analysis Results for Gaseous Oxidizer Flux (G_{ox}) using 1% Nominal Uncertainties.

x_i	$\dfrac{\partial G_{ox}}{\partial x_i}$	1% of Nominal	$\dfrac{\partial G_{ox}}{\partial x_i}B_{x_i}$
C_d	$0.327\ \dfrac{lbm}{in^2\ sec}$	0.02	$0.0031\ \dfrac{lbm}{in^2\ sec}$
P_{up}	$0.0002\ \dfrac{lbm/in^2\ sec}{psi}$	11 psi	$0.0024\ \dfrac{lbm}{in^2\ sec}$
D_{vent}	$6.151\ \dfrac{lbm/in^2\ sec}{in}$	0.001 in	$0.00615\ \dfrac{lbm}{in^2\ sec}$
γ	$0.0763\ \dfrac{lbm}{in^2\ sec}$	0.0139	$0.0011\ \dfrac{lbm}{in^2\ sec}$
m_i	$-0.0016\ \dfrac{lbm/in^2\ sec}{gm}$	0.50 gm	$-0.0008\ \dfrac{lbm}{in^2\ sec}$
m_f	$0.0016\ \dfrac{lbm/in^2\ sec}{gm}$	0.41 gm	$0.0006\ \dfrac{lbm}{in^2\ sec}$
ρ_f	$1.673\ \dfrac{lbm/in^2\ sec}{lbm/in^3}$	$0.0003\ \dfrac{lbm}{in^3}$	$0.0006\ \dfrac{lbm}{in^2\ sec}$
L	$0.0056\ \dfrac{lbm/in^2\ sec}{in}$	0.1 in	$0.0006\ \dfrac{lbm}{in^2\ sec}$
D_i	$-0.613\ \dfrac{lbm/in^2\ sec}{in}$	0.0082 in	$-0.00502\ \dfrac{lbm}{in^2\ sec}$
T_{up}	$-0.0003\ \dfrac{lbm/in^2\ sec}{R}$	5.25 R	$-0.0015\ \dfrac{lbm}{in^2\ sec}$

By combining the terms in the last column of Table 1 according to Equation (7), the overall bias for G_{ox} using the zero-order analysis is ±0.0093 lbm/in²·sec or ±3.0% of nominal. Comparing this to the results in the last column of Table 1, one can see that the uncertainty in G_{ox} is strongly dominated by the propagation of uncertainties in D_{vent} and D_i. Uncertainties in C_d, P_{up}, and γ are minor contributors while the remaining input parameters

(m_i, m_f, ρ_f, L, and T_{up}) have only a weak influence. This analysis indicates that by minimizing uncertainties in D_{vent} and D_i, and to some extent C_d, P_{up}, and γ, the uncertainty in G_{ox} is minimized. The results also show that the other parameters can be neglected so long as the magnitudes of their uncertainties are equal to or less then those of the dominant parameters on a percent of nominal basis. Table 2 at the bottom of this page shows the results of the zero-order analysis on all of the data reduction equations. The double checks represent the dominant input parameters, single checks are the minor contributors, blanks show a weak influence, and the dash indicates that the particular data reduction equation is independent of that input parameter.

Detailed LHM Uncertainty Analysis

The next step in the examination of the LHM uncertainty was to perform the detailed level analysis. This is a refining type analysis that is performed once test data is taken which permits the calculation of the precision index, or 2σ, and a better estimate of the system biases. Table 3 below shows representative values for the precision limits for the different data reduction results as well as the precision uncertainty as a percent of the nominal resultant value.

Table 3. Representative Precision Limits in the Experimental Results.

Experimental Result	Precision Limit, P_α	% of Nominal
G_{ox} (1)	$\pm 0.00489\ \dfrac{lbm}{in^2\ sec}$	±1.6
$\dot{r}$ (2)	$\pm 0.001158\ \dfrac{in}{sec}$	±2.9
O/F (3)	±0.296	±5.8
C* (4)	$\pm 317.2\ \dfrac{ft}{sec}$	±6.8

Table 4 shows the estimates of the input parameter bias limits in absolute magnitude as well as a percentage of actual value for a representative HTPB test. The estimates of the individual biases were made at a 95% confidence level. The biases for D_{vent} and C_d were based on the venturi manufacturer's

Table 2. Results of Zero-Order Analysis on Data Reduction Equations.

	INPUT PARAMETERS														% Bias
	C_d	P_{up}	T_{up}	D_{vent}	γ	m_i	m_f	ρ_f	L	D_i	t_i	t_f	D_{th}	P_c	
G_{ox} (1)	√	√	√	√√	√					√√	-	-	-	-	±3.0
$\dot{r}$ (2)	-	-	-	-	-	√	√	√	√	√	√	√	-	-	±3.9
O/F (3)	√	√		√√		√	√	-	-		√	√	-	-	±4.6
C* (4)		√		√√				-	-	-			√√	√	±3.0

5

American Institute of Aeronautics and Astronautics

Table 4. Estimate of Input Parameter Bias Limits for LHM Detailed Analysis of G_{ox}.

Input Parameter	Bias Limit, B_α	% of Actual
C_d	±0.02	±2.1
D_{vent}	±0.001 in	±1.0
P_{up}	±5 psi	±0.5
T_{up}	±10 R	±1.9
γ	±0.05	±3.6
m	±0.0005 gm	±0.0001
ρ_f	±0.004 lbm/in³	±11.9
L	±0.05 in	±0.5
D_i	±0.05 in	±6.1
D_{th}	±0.005 in	±1.6
P_c	±10 psi	±2.1
t_i	±0.035 sec	±1.8
t_f	±0.115 sec	±5.8

were primarily due to oscillations and drops or rises in pressure during the burn duration. On average, this conceptual bias was ±30 psi. Using the root-sum-square method of combining the conceptual and calibration biases gave a total bias in chamber pressure of ±31.6 psi.

The primary contribution to the bias in the ignition and shutdown times was a conceptual uncertainty in the definition of burn time. This concept is illustrated in Figure 4 which shows the pressure-time plot for a typical HTPB test conducted using an aft mixing section with $\ell = 4.0"$ (see Figure 1). Detailed in Figure 4 are the two regions within which it may safely be assumed the ignition and shutdown points lie. These two regions were from test to test, on average, 0.07 and 0.23 seconds long, consecutively. According to convention, the bias limit for each region is therefore one-half the span, or ±0.035 and ±0.115 seconds, as shown in Table 4.

specifications. For P_{up} and T_{up}, biases were based on the calibration specifications and on fluctuations of conditions during tests. The bias in γ was based on scatter in published values for oxygen. The bias for the mass measurements was based on the accuracy of the digital analytical scale used. The fuel grain length bias was taken from the accuracy of the calipers used to measure the grains. For the fuel density, the bias was estimated based on scatter in accepted density values. The bias in the initial port diameter was estimated based on the casting mandrel tolerances. The bias in D_{th} was based on drawing tolerances.

As stated earlier, a bias of ±10 psi was introduced in the measurement of chamber pressure due to the methodology used for calibration of the test data. However, an additional, more dominant bias due to a conceptual uncertainty in the definition of chamber pressure was present in the testing as well. This is illustrated in Figure 3 below. Uncertainty in the chamber pressure measurement (which was entered in the data reduction equations as the mean pressure)

Figure 4. Illustration of Burn Duration Conceptual Bias.

Taking the values from Table 4 and substituting them into Equation (7) gives a bias limit for a typical G_{ox} test of ±0.032 lbm/in²·sec (for this particular test, $G_{ox} = 0.319$ lbm/in²·sec), or approximately ±10.7%. Next, substituting this bias value and precision limit for G_{ox} form Table 3 into Equation (5) gives an overall uncertainty limit for G_{ox} of ±0.0324 lbm/in²·sec, or ±10.8%. The uncertainty values vary slightly from test to test due to the dependence of the sensitivity parameters to the actual test conditions.

Table 5 shows the results of similar calculations carried out on Equations (2), (3), and (4) for the same test. Shown in the last two columns are the bias and total uncertainty limits in terms of percent of the data reduction result. By examining plots of the results generated from the reduction of the LHM data, with "error bars" included to represent the uncertainty in the results, and by examining and comparing Tables 1 through 5, several items can be noted which are indicative of the behavior of hybrid testing.

Figure 3. Illustration of Chamber Pressure Conceptual Bias.

Table 5. Detailed LHM Uncertainty Analysis Results for a Typical Test.

	INPUT PARAMETERS														% Bias	% Uncert.
	C_d	P_{up}	T_{up}	D_{vent}	γ	m_i	m_f	ρ_f	L	D_i	t_i	t_f	D_{th}	P_c		
G_{ox} (1)	✓			✓						✓✓	-	-	-	-	±10.7	±10.8
ṙ (2)	-	-	-	-	-					✓✓	✓	✓✓	-	-	±8.2	±8.7
O/F (3)	✓			✓				-	-	-	✓	✓✓	-	-	±7.1	±9.2
C* (4)			✓	✓	✓			-	-	-		✓	✓✓	✓✓	±8.2	±10.5

Figure 5 shows the typical hybrid plot of ṙ versus G_{ox} with the uncertainty of the results indicated by the error bars. Also shown in Figure 4 is a curve fit taken from Sutton for HTPB.[5] The dashed lines indicate 5% error bars on the curve fit which provided reasonable coverage of the original data from which the fit was generated. One of the indications of Figure 5 is that the majority of the data generated by the LHM, within the uncertainty of the results, falls within the 5% bands of the curve fit. However, equally evident is the fact that several other fits could be generated that would equally suffice for the LHM data due to the high level of uncertainty. This is a demonstration of the inaccuracy in using labscale hybrid data to generate regression rate curve fits such as the one in Figure 5. Further, once a curve fit is generated, the level of uncertainty associated with the data is lost without knowledge of the original data. Current research by Brown, Coleman, and Steele[6] at The University of Alabama in Huntsville is examining the methodology necessary to determine the uncertainty of such curve fits generated from test data of this type.

By comparing the precision and bias limits (Tables 3 and 5), it can be seen that the overall uncertainties of the regression rate and flux measurements are dominated by the bias limits which indicates good repeatability. In a closer examination of Table 5, the primary contributors to the uncertainty in the data points in Figure 5 are the measurement of the initial port diameter and the conceptual bias of the shutdown transient time. This

points to two methods to reduce the uncertainty in this type of plot. The first is to reduce the uncertainty in the measurement of the port diameter by either increasing the size of the fuel grain or increasing the measurement accuracy. The second is to reduce the uncertainty in the burn times. This can only be accomplished by increasing the burn duration since the bias itself is conceptual rather than due to any measurement inaccuracy. Increasing the duration reduces the sensitivity of the regression rate equation to the conceptual bias even though the bias itself remains the same.

As stated previously, it is sometimes useful to compare the efficiency of combustion in the form of the characteristic velocity. Figure 6 shows a plot of C* versus O/F for several HTPB tests as compared to theoretical C* values generated using the NASA SP-273 thermochemistry code. The stochiometric O/F ratio for HTPB/N-100 is approximately 3.0. Shown in Figure 6 are the results from tests using 1.0", 4.0", and 0.0" or butted aft closure (see Figure 7) configurations. Data points that lie closer to the theoretical curve would be considered to have higher C* efficiencies. Thus, on initial inspection of Figure 6 the conclusion may be drawn that tests conducted using the 4.0" closure have higher C* efficiencies when compared to those using the 1.0" or butted aft closure. However, the uncertainty bars on the C* results indicate that the level of uncertainty does not permit the resolution required to measure a test-to-test difference in C* for these tests. Thus, no
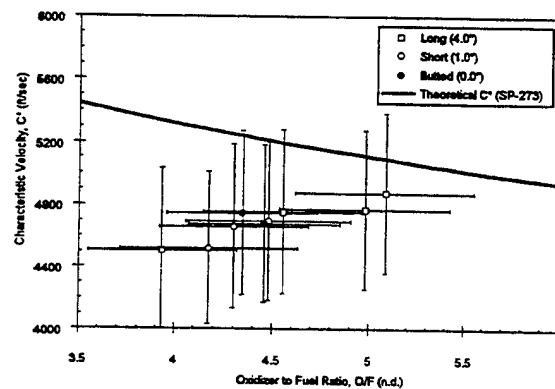
Figure 5. Plot of Regression Rate vs. Oxidizer Flux with Uncertainty Bars.

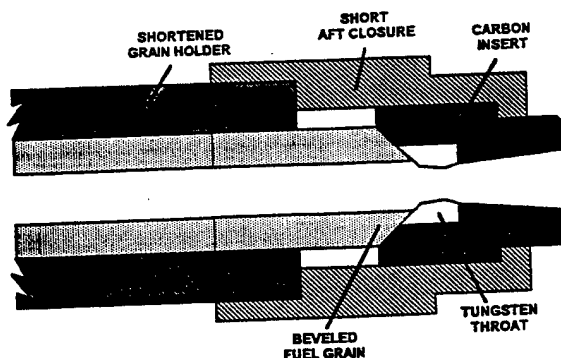Figure 6. Plot of C* versus O/F Ratio for Selected HTPB Tests with Uncertainty.

Figure 7. LHM Butted End Grain Configuration.

conclusions may be drawn about the effect of instability on the C* efficiency in the LHM tests. In fact, it is quite possible that efficiencies of greater than 100% could be generated by the LHM according to the uncertainty bars. Finally, the plot shows that for this type of analysis to be worthwhile, uncertainties in the results must be very small, on the order of ±1%) to gain the necessary resolution.

Referring again to Tables 3 and 5, by comparing the bias and precision limits for C* and $O/_F$, it is evident that the precision limits contribute to a sizable portion of the overall uncertainties in these two results. This is indicative of the difficulty of repeating particular test conditions for a comparison of this type. Also, this comparison indicates that reduction of biases contributions in the input parameters are only partially effective. Nevertheless, in examining Table 5 it is seen that burn time bias dominates the bias in $O/_F$ and the that C* bias is dominated by biases in nozzle throat diameter and chamber pressure. Again, increasing the burn duration would reduce the $O/_F$ bias.

Two methods exist for reducing the C* bias. The first is to reduce the bias uncertainty in the measurement of the nozzle throat diameter. It is doubtful that the accuracy could be increased due to the small size of the nozzle throat and the fact that the diameter can erode measurably during a test which would again lead to a conceptual bias. However, by increasing the size of the throat, which points to increasing the scale of the motor as a whole, would reduce the sensitivity of the C* data reduction equation to the throat measurement bias. The second method to reduce the C* bias is to select a more accurate method for calibrating the chamber pressure data. This will have only a limited effect since the conceptual bias dominates in this reading due to the oscillations that exist even in "stable" tests, or those with a low level of pressure oscillations. The conceptual bias is even greater for "unstable" tests in which oscillations of up to ±75 psi (or approximately ±17% of mean P_c) have been noted.[1,4]

Another possibility is to test at higher chamber pressures thus reducing the percent bias in P_c. This would only be effective under the assumption that the absolute bias in chamber pressure remains constant. There is no indication either way as to the validity of this assumption.

Summary of Results and Conclusions

The typical uncertainties in the measurements of the fuel regression rate (±8.7%), oxidizer flux (±10.8%), motor characteristic velocity (±10.5%), and the motor oxidizer-to-fuel mass ratio (±9.2%) were found to place limits on the use of the labscale motor for quantitative investigations. These limits were indicated through an examination of standard plots for determining hybrid performance. First, labscale regression rate/oxidizer flux data was shown to be of limited use in the generation of curve fits. This was due primarily to a high measurement in the grain initial port diameter and a uncertainty in the burn duration. Second, large conceptual bias in the C* versus $O/_F$ ratio plot the low resolution in the C* versus $O/_F$ ratio plot indicates the lack of utility of labscale data in determining small changes (<10%) in C* efficiency. This low resolution was due, in part, to the lack of repeatability, indicated by the dominant precision index for C* and $O/_F$ ratio; and in part due to the domination by the measurement uncertainty of the nozzle throat diameter and conceptual bias in the average chamber pressure.

In general, three methods were identified as approaches to reducing the uncertainties mentioned. The first was to increase the scale of the test motor. This would reduce the uncertainties in the measurements of the diameters of the fuel grain port and nozzle throat. The second method was to increase the burn duration, which coincidentally would require an increase in the motor size. The increase would reduce the domination of the burn duration conceptual bias. The last approach identified was to reduce the uncertainty in the average chamber pressure measurement through either an increase in the test pressure or in the accuracy of the calibration methodology. However, both of these were believed to have questionable or limited effectiveness.

A parametric study of the changes suggested is recommended to determine the magnitude of improvement in the accuracy that could be expected. Additionally, this study should indicate the optimal motor configuration for obtaining high quality hybrid performance data. At minimum, it is clear that all test programs conducting hybrid motor performance measurements must have some level of uncertainty analysis conducted in order to determine the quality of the data obtained.

References

1. Hollman, S. and Frederick, R., "Labscale Testing Techniques for Hybrid Rockets," *AIAA Paper No. 93-2409*, June 1993.

2. Greiner, B. E., "Experimental Investigation of Combustion Instability using a Labscale Hybrid Rocket Motor," A Master's Thesis, The University of Alabama in Huntsville, October, 1993.

3. Coleman, H. W. and Steele, W. G., *Experimentation and Uncertainty Analysis for Engineers*, John Wiley & Sons, Inc., 1989.

4. Greiner, B. and Frederick, R. A., Jr., "Experimental Investigation of Labscale Hybrid Instability," *AIAA Paper No. 94-2878*, June 1994.

5. Sutton, G., *Rocket Propulsion Elements*, 6th edition, John Wiley & Sons, 1992, pp. 502-552.

6. Brown, K., Coleman, H., and Steele, W., "Estimating Uncertainty Intervals for Linear Regression," *AIAA Paper No. 95-0796*, January 1995.

clean with nonuniform burning, with some pronounced dips and rises.

Overall, there is a good qualitative correlation between the predicted augmented pressure curve and the static firing data of Ref. 4. Because of nozzle throat erosion later in the experimental firing, the predicted peak pressure is somewhat higher than expected (no throat erosion modeled). Similarly, for the flight case with increasing forward acceleration and spin as the firing proceeds, the predicted pressure peaks somewhat higher than expected relative to the reported data of Ref. 4. Only later into the flight does the normal acceleration of the motor rotation begin to dominate the lateral and longitudinal acceleration components in affecting the combustion process.

References

[1]Greatrix, D. R., "Parametric Analysis of Combined Acceleration Effects on Solid-Propellant Combustion," *Canadian Aeronautics and Space Journal*, Vol. 40, No. 2, 1994, pp. 68–73.

[2]Hejl, R. J., and Heister, S. D., "Solid Rocket Motor Grain Burnback Analysis Using Adaptive Grids," *Journal of Propulsion and Power*, Vol. 11, No. 5, 1995, pp. 1006–1011.

[3]Greatrix, D. R., Gottlieb, J. J., and Constantinou, T., "Quasi-Steady Analysis of the Internal Ballistics of Solid-Propellant Rocket Motors," *Canadian Aeronautics and Space Journal*, Vol. 33, No. 2, 1987, pp. 61–70.

[4]Lucy, M. H., "Spin Acceleration Effects on Some Full-Scale Rocket Motors," *Journal of Spacecraft and Rockets*, Vol. 5, No. 2, 1968, pp. 179–183.

Propellant Design Relationships for Throttled Gas Generators

R. A. Frederick Jr.*
*University of Alabama in Huntsville,
Huntsville, Alabama 35899*
and
Iwao Komai†
NOF Corporation, Taketoyo, Achii 470-23, Japan

Nomenclature

A_b = propellant burn surface area
a = burning rate coefficient
a' = burning rate coefficient at reference pressure and temperature
$c*$ = propellant characteristic exhaust velocity
K = burn area over throat area
$\dot{m}_f$ = mass flow rate of fuel
N_{MAX} = maximum allowable pressure sensitivity
n = pressure exponent
P = chamber pressure
P' = chamber pressure over reference pressure
r = propellant burn rate
T_i = initial propellant temperature
α = temperature sensitivity coefficient
α' = temperature sensitivity coefficient at reference pressure
ρ_p = propellant density

Subscripts
r = reference conditions
s = standard conditions
1 = maximum limit
2 = minimum limit

Introduction

WHEN formulating gas generator propellants, the designer must achieve a specified mass flow schedule. One approach is to use propellants with large pressure sensitivity and a variable-area nozzle. This promotes substantial variations in mass flow while maintaining a reasonable pressure range. The propellant temperature sensitivity and combustion efficiency are additional factors that influence the design. The objective of this work is to calculate a propellant solution space that fulfills the design requirements for a variable-flow gas generator. The scope includes 1) developing a design methodology that incorporates mass flow rate, pressure, and temperature requirements; 2) deriving design equations for propellants with temperature-dependent pressure exponents; and 3) calculating regions of compliant propellant ballistics for an example ducted rocket application.

Approach

Gas Generator Constraints

The gas generator design is assumed to be bounded by mass flow rate, propellant temperature, and chamber pressure requirements. The mass flow rate range of a ducted rocket motor can be determined from anticipated altitude, flight Mach number, and operational oxidizer-to-fuel ratio considerations: $\dot{m}_{f1} \leq \dot{m}_f \leq \dot{m}_{f2}$. The gas generator must deliver this entire range. The operating environment dictates a range of initial propellant temperatures: $T_{i,1} \leq T \leq T_{i,2}$. The maximum chamber pressure is defined by structural/weight considerations of the missile. The minimum pressure could be guided by either the choked-flow or propellant extinguishment: $P_1 \leq P \leq P_2$. It is not required that this pressure range be spanned, but the pressure limits must not be violated.

For steady-state operation, the propellant burning rate range is derived from extreme values of the required mass flow rate and the propellant burn surface area by

$$r_2 = \dot{m}_{f\,max}/\rho_p A_{b\,min} \tag{1}$$

$$r_1 = \dot{m}_{f\,min}/\rho_p A_{b\,max} \tag{2}$$

A stable equilibrium chamber pressure also requires the pressure exponent must be less than one.

Figure 1 shows how these burn rate, pressure, and pressure-exponent limits form a parallelogram-shaped region (A–B–C–D) of compliant burn rate/pressure combinations. Initial temperature effects are illustrated by two propellant burn rate curves. The maximum temperature curve intersects point A, while the minimum temperature curve intersects point C. Expressing these design criteria mathematically, we have

$$r(P_1, T_2) \leq r_1 \quad \text{and} \quad r(P_2, T_1) \geq r_2 \tag{3}$$

and $n < 1$.

Mathematical Derivations

Propellant burning rate is assumed as a function of pressure and temperature with

$$r = a_s \exp[\alpha(T_i - T_{i,s})]P^{[n_s + \beta(T_i - T_{i,s})]} \tag{4}$$

Small variations in β will result in large changes in burning rate at operational pressures. Normalizing with a reference pressure P_r, at which the contribution of the β term is zero, yields,

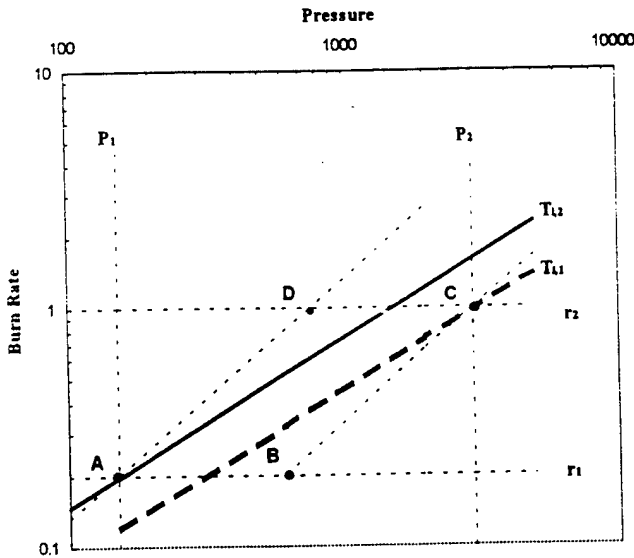$$r = a'_s \exp[\alpha'(T_i - T_{i,s})]P'^{[n_s + \beta(T_i - T_{i,s})]} \tag{5}$$

$$B_n^{I} = \frac{T_{i,2} - T_{i,1}}{\ell n\, P_2' - \ell n\, P_1'} \tag{9b}$$

$$C_n^{II} = \frac{\ell n\, P_1'(T_{i,2} - T_{i,s}) - \ell n\, P_2'(T_{i,1} - T_{i,s})}{\ell n\, P_2' - \ell n\, P_1'} \tag{9c}$$

Now, substituting $n_{s\,max}$ into Eqs. (6) and (7) gives equations for the reference burning rate at conditions II and III.

$$\ell n\, a_s'|_{yII} = \ell n\, r_2 - n_{s\,max}\, \ell n\, P_2' - (T_{i,1} - T_{i,s})(\alpha' + \beta\, \ell n\, P_2') \tag{10}$$

$$\ell n\, a_s'|_{III} = \ell n\, r_1 - n_{s\,max}\, \ell n\, P_1' - (T_{i,2} - T_{i,s})(\alpha' + \beta\, \ell n\, P_1') \tag{11}$$

where $n_{s\,max}$, the maximum allowable standard exponent, and N_{MAX}, the overall maximum exponent that the designer allows, are related by

$$n_{s\,max} = N_{MAX} \le 1.0, \qquad\qquad \text{if}\quad \beta = 0 \tag{12a}$$

$$n_{s\,max} = N_{MAX} - \beta(T_{i,2} - T_{i,s}), \quad \text{if}\quad \beta > 0 \tag{12b}$$

$$n_{s\,max} = N_{MAX} - \beta(T_{i,1} - T_{i,s}), \quad \text{if}\quad \beta < 0 \tag{12c}$$

Equations (8–12) now define the reference propellant burning rate a_s' and its corresponding reference exponent n_s as functions of α' and β.

Results for an Example Application

An example application is now shown for a ducted rocket gas generator. Table 1 lists the selected and derived parameters for the application. An 8.0-in.-diam, end-burning gas generator was assumed to operate over a Mach number range of 2.5–3.5, at altitudes from 6500 to 65,000 ft. Other assumptions include 1) the reference pressure is 1000 psia, 2) the reference temperature is 65°F, and 3) $N_{MAX} = 1.0$. The effect of temperature sensitivity parameters α' and β on the resulting a_s' vs n_s solution space will now be presented and discussed for this application.

Conventional Propellants: Effect of α when $\beta = 0$

The design relationships are first applied to conventional propellants that have no pressure exponent sensitivity ($\beta = 0$). Figure 2a is a propellant diagram that describes the region of acceptable burn rate properties as a function of increasing α' (equivalent to conventional propellant temperature sensitivity for this case). The x axis represents the propellant burning rate at the reference pressure ($P_r = 1000$ psia) and reference temperature ($T_{i,s} = 65°F$). The y axis represents the corresponding burn rate exponent at the reference temperature n_r.

The $\alpha = 0$ case shows the largest area of ballistic properties that will satisfy the gas generator constraints. The solution space is a triangular region with vertices at condition I [defined by Eqs. (8) and (9)], condition II [defined by Eqs. (10) and (12a)], and condition III [defined by Eqs. (11) and (12a)]. Condition I represents the reference burning rate for the minimum

Fig. 1 Ballistics limitations diagram.

where $a_r' = r(P_r, T_{i,s})$ and $P' = P/P_r$, making $\alpha' = \alpha + \beta\, \ell n\, P_r$. Normalizing makes α' the temperature sensitivity at the reference pressure. Changes in β then rotate each constant-temperature burn rate line about the point that it intersects the reference pressure.

Propellant Design Relationships

Equations to define a burning-rate, pressure-exponent solution space are now developed that satisfy the design constraints. Three limiting conditions are examined: condition I, the minimum exponent propellant sketched in Fig. 1; condition II, the maximum exponent propellant that overlays line A–D in Fig. 1; and condition III, the maximum exponent propellant that overlays line B–C in Fig. 1.

The range of acceptable pressure exponents for condition I is found by substituting Eq. (5) into Eqs. (3), yielding,

$$n_s \le \frac{\ell n\, r_1 - \ell n\, a_s'}{\ell n\, P_1'} - \frac{T_{i,2} - T_{i,s}}{\ell n\, P_1'}\,\alpha' - (T_{i,2} - T_{i,s})\beta \tag{6}$$

$$n_s \ge \frac{\ell n\, r_2 - \ell n\, a_s'}{\ell n\, P_2'} - \frac{T_{i,1} - T_{i,s}}{\ell n\, P_2'}\,\alpha' - (T_{i,1} - T_{i,s})\beta \tag{7}$$

The reference burning rate for condition I is found by equating Eqs. (6) and (7) and solving

$$\ell n\, a_s'|_{I} = A_a^{I} - B_a^{I}\alpha' - C_a^{I}\beta \tag{8}$$

where

$$A_a^{I} = \frac{\ell n\, P_2'\, \ell n\, r_1 - \ell n\, P_1'\, \ell n\, r_2}{\ell n\, P_2' - \ell n\, P_1'} \tag{8a}$$

$$B_a^{I} = \frac{\ell n\, P_2'(T_{i,2} - T_{i,s}) - \ell n\, P_1'(T_{i,1} - T_{i,s})}{\ell n\, P_2' - \ell n\, P_1'} \tag{8b}$$

$$C_a^{I} = \frac{\ell n\, P_1'\, \ell n\, P_2'(T_{i,2} - T_{i,1})}{\ell n\, P_2' - \ell n\, P_1'} \tag{8c}$$

Substituting Eqs. (8) into either Eq. (6) or (7) yields the minimum exponent as a function of α and β:

$$n_s|_{I} = A_n^{I} + B_n^{I}\alpha' + C_n^{I}\beta \tag{9}$$

where

$$A_n^{I} = \frac{\ell n\, r_2 - \ell n\, r_1}{\ell n\, P_2' - \ell n\, P_1'} \tag{9a}$$

Table 1 Baseline ducted rocket gas generator

Selected	Derived
$\dot{m}_{min} = 0.48$ lbm/s	$r_1 = 0.20$ in./s
$\dot{m}_{max} = 3.26$ lbm/s	$r_2 = 1.00$ in./s
$T_1 = -15°F$	$A_a^{I} = -0.5902$
$T_2 = 145°F$	$B_a^{I} = -21.32$
$P_1 = 150$ psia	$C_a^{I} = -111.31$
$P_2 = 3000$ psia	$A_n^{I} = 0.5372$
$A_b = 50.27$ in.^{2}	$B_n^{I} = 53.4$
$N_{MAX} = 1.0$	$C_n^{I} = -21.4$
$\rho_P = 0.047$ lb/in.^{3}	——

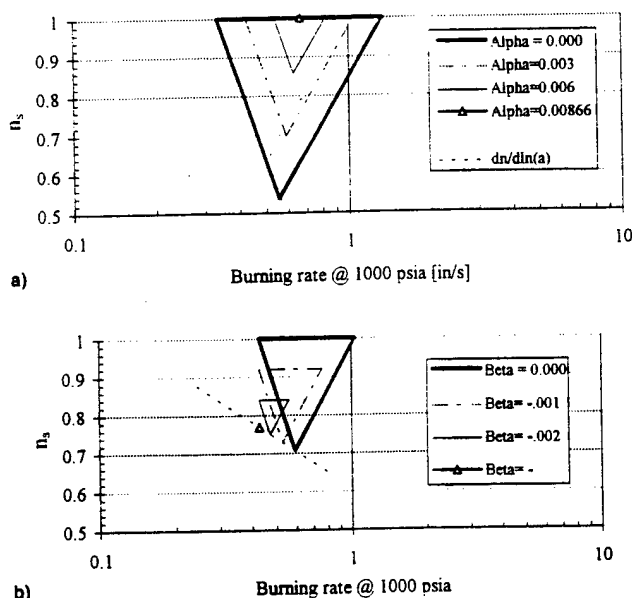a)　　Burning rate @ 1000 psia [in/s]

b)　　Burning rate @ 1000 psia

Fig. 2　Propellant ballistics diagram: a) $\alpha = 0.6-0.00866$, $\beta = 0.000$ and b) $\alpha = 0.00318$, $\beta = 0$ to -0.00289.

exponent propellant that satisfies the constraints. The maximum exponent N_{MAX} and standard exponent n, are identical in this case.

As α' is increased, the triangular region becomes smaller. The minimum exponent increases until the burn rate curves span from line A–C to line B–D in Fig. 1, in which case

$$\alpha'_{MAX} = (N_{MAX} - A_n^I)/B_n^I, \qquad @(\beta = 0) \qquad (13)$$

giving the value of 0.00866 1/°F, which is plotted as the center point of Fig. 2a.

Effect of β at Constant α'

Figure 2b illustrates the effects of variations in the pressure exponent sensitivity for a fixed value of α'. In this case, α' is assumed constant at 0.00318 1/°F, while the exponent sensitivity ranges from 0 to −0.00289 1/°F. The variation in exponent sensitivity causes a reduction of the triangular solution space until it becomes a point at the maximum allowable value. The minimum exponent increases while its corresponding reference burning rate decreases.

Increasing the pressure exponent sensitivity then reduces and translates the propellant solution space to narrower exponent ranges and lower reference burning rates. The maximum value of pressure exponents also decreases as β increases [Eq. (12b)].

Conclusions

Propellant design relationships for variable exponent propellants have been developed and applied to a gas generator design problem. The method defines a region of acceptable propellant ballistic properties as a function of two propellant temperature sensitivity parameters. The design achieves mass flow rate, pressure, pressure exponent, and temperature range constraints. The propellant diagram approach gives the designer or propellant formulator a region of compliant ballistic properties for a given application instead of a single design point.

Acknowledgment

Effects of Kevlar® Fibers on Ammonium Perchlorate Propellant Combustion

M. H. Hites*

Illinois Institute of Technology, Chicago, Illinois 60616

and

M. Q. Brewster†

University of Illinois at Urbana–Champaign,
Urbana, Illinois 61801

Introduction

MICROSCOPIC chopped Kevlar fibers were added to ammonium perchlorate (AP) composite propellants to investigate their burn rate enhancing features. Kevlar fibers have been used in the past[1] to increase the strength of AP composite propellants, but as a side effect it was observed that the fibers increased the burning rate of an AP/Al composite as much as 27% at 3.5 MPa. In the present work, steady burning rate measurements and combustion photography were used to quantify the burning rate enhancement and suggest a possible explanation for the observed increases.

Experimental

The steady burning rate was measured for the series of AP composite propellants shown in Table 1. The burning rate of each propellant was measured using the fuse wire technique in a nitrogen-purged combustion bomb. Strands of 7×7 mm cross section and 30–60 mm length were coated lightly with vacuum grease as an inhibitor and were ignited by nichrome wire. The initial temperature of strands was ambient room temperature (20–25°C).

High-speed and microscope photography were used to investigate the qualitative differences between the gas phase combustion and surface condition of the various propellants. Conventional VHS camcorder movies and 35-mm SLR macrolens photography were also used to reveal macroscopic differences between the propellants. Although only photographs from the 35-mm photography are presented here, some observations based on the other photographic techniques are discussed when applicable.

Results

Burning rate measurements of the nonmetallized propellants are shown in Fig. 1 along with the corresponding burning rate equation:

$$r = aP^n$$

where burning rate r is in mm/s and pressure P is in MPa. The coefficient a and exponent n were determined by a least-squares fit, and a linear correlation coefficient of 0.98 or better was calculated for each of the curve fits. Figure 1a shows that the addition of small amounts of Kevlar increased the burning rate and lowered the burning rate exponent slightly in nonmetallized AP systems. Figure 1b compares propellants with fiber lengths of 2 and 5 mm to a fiberless AP composite propellant and demonstrates increased burning rate with increased

AIAA 96-3254
AMMONIUM NITRATE-BASED SOLID FUEL
GAS GENERATOR FOR GAS HYBRID
ROCKETS

Kohsei Miyata
Robert A. Frederick, Jr.

Propulsion Research Center
University of Alabama in Huntsville
Huntsville, AL 35899

32nd AIAA/ASME/SAE/ASEE
Joint Propulsion Conference
July 1-3, 1996 / Lake Buena Vista, FL

AMMONIUM NITRATE-BASED SOLID FUEL GAS GENERATOR FOR GAS HYBRID ROCKETS

Kohsei Miyata[*]
Robert A. Frederick, Jr.[†]

Propulsion Research Center
University of Alabama in Huntsville
Huntsville, AL 35899

Abstract

Ammonium-nitrate(AN) based propellant are candidates for fuel generation in a gas hybrid rockets(GHR). When used as a gas generator in conjunction with HNO_3, the calculated specific impulse increases as much as 25 seconds compared with AN solid propellant rockets. This study examines the combustion mechanisms of metalized, AN gas generator propellants for this application. Analysis of the combustion wave structure of the AN gas generator propellants showed that Granular Diffusion Flame(GDF) theory can explain the effects of the pressure and temperature on the burning rate characteristics of the AN propellants. Experimental data and theoretical calculations showed excellent correlation within the pressure and temperature range investigated. Results of the analysis also showed qualitatively that chemical reaction in the gas phase is a dominant factor on determining the burning rate of these propellants. The gas phase sensitivity of the combustion wave dominated the propellant temperature sensitivity. Thus, it is concluded that the burning rate characteristics and temperature sensitivity of these AN propellants are controlled by the gas phase chemical reactions despite existence of thick melt layer on the burning surface.

Introduction

Ammonium nitrate (AN) is an insensitive, affordable and Cl-free oxidizer crystal for solid propellants. Recently, these characteristics have become important for next generation solid propellant rockets and hence, AN has regained interest as a replacement of ammonium perchlorate(AP)[1-8]. Compared with AP composite propellants, the AN propellants must overcome the problems of low burning rate, high pressure exponent, and low specific impulse(Isp).

For burning rate augmentation, it is known that some chromate compounds, such as Cr_2O_3, $Cu_2Cr_2O_7$, or $(NH_4)_2Cr_2O_7$ act as catalysts[2,9,10]. However, these additives have not achieved the burning rate levels that are required for practical systems.

The high pressure exponents associated with AN (n~0.8) are not desirable for solid propellants. However, this characteristic is desirable for variable flow gas generator propellants as some studies show[11-13].

Metal particles such as Al and/or Mg have been introduced into AN composite propellants to increase the specific impulse[1,3]. Unfortunately, all such attempts were not completely successful without some AP to achieve the temperature required for metal particle ignition.

The hybrid rocket also has been regained interest as an insensitive, Cl-free and affordable propulsion system. Especially, the gas generator type hybrid rocket(GHR)[14-22] combined with insensitive gas generators, which is shown in Figure 1, is considered as a near-term application. Although some studies focused on utilization of high energy-density materials such as glycidyl azide polymer(GAP), experimental work[19,20] revealed that hydroxyl terminated polybutadiene(HTPB) as a fuel binder still produces a good performance, so that a fuel-rich, insensitive conventional gas generator is a possibility for the GHR gas generator. For this conventional gas generator, AP cannot be used without a Cl scavenging agent because it contains large amount of Cl.

On the other hand, problems of AN composite propellants described above can be overcome if GHR is introduced. Thus, ammonium nitrate(AN) was chosen as an oxidizer in this study.

It is known that there are several reaction paths on the decomposition and reaction of AN[9,23-26] which makes detailed investigation very difficult. Thus, detailed combustion mechanisms of AN composite propellants have not yet been verified.

In this study, theoretical performance of GHR with AN composite propellants is briefly described. The burning rate and temperature sensitivity of AN composite propellants are investigated in order to gain basic

---

[*]Graduate Student, Student Member AIAA.
[†]Assistant Professor, Department of Mechanical and Aerospace Engineering, Senior Member AIAA.

understanding of combustion mechanisms of the propellants.

Theoretical Performance of GHR

GHR performance with AN composite propellants is calculated with using thermochemical equilibrium codes[27]. Results are shown in Figure 2. The liquid oxidizer chosen is HNO_3, which is storable in room temperature. For comparison, the Isp of AN composite propellant which refers to solid propellant rockets is also shown. Equivalence ratio, Φ_{eq}, is equal to 1.0 for both cases. Chamber pressure, P_c, is varied from 5 to 20 MPa. Values of Isp are the ones at optimum expansion.

As shown, the Isp of the GHR ranges from 247 to 278 seconds, which is greater than that of solid rockets at the same chamber pressure. For example, the Isp of the GHR reaches approximately 263 seconds at Pc = 10 MPa, while that of AN composite is approximately 238 seconds. The GHR produces the same Isp at lower pressure, or higher Isp at the same pressure. The Isp increase shown here is considered to be enough to compensate weight increase caused by additional oxidizer tank, feed system and secondary chamber. Mean molecular weight of the exhaust gas is relatively constant through chamber pressure range, while adiabatic flame temperature increases as the pressure increases. Thus, the pressure dependency of Isp is caused by the flame temperature increase.

Figure 3 shows relationships between vacuum specific impulse, Isp_{vac} for various liquid oxidizer /fuel gas mass flow ratio, O/F. HTPB concentration within the gas generator propellant is changed from 20 to 60 %wt. Chamber pressure is 10MPa. No metal compounds are included in this calculation. Optimum O/F which gives maximum $Isp_{,vac}$ remained unchanged except for the 50% HTPB propellant. For a system stand point lower O/F ratio is suitable to decrease the oxidizer tank size. In this point of view, lower HTPB concentration or higher AN concentration within the propellant is desirable. Ultimately the optimum O/F and fuel concentration have to be determined for each specific application with system trade studies.

Burning Rate Characteristics

Typical burning rate of AN composite propellants is shown in Figure 4[3,7]. This composition includes 60% AN, 20% HTPB and 20% Al. Initial temperature was changed from 243 to 343 K. Vieille's law (or St. Robert's law) for the propellant yields following expressions:

$$r_b = a \, P_c^n \tag{1}$$

where a and n are tabulated as Table-1. T_0 is initial temperature of the propellant. As is clearly seen, the burning rate linearly increases as pressure increases in $\ln P_c$ vs. $\ln r_b$ plane. Pressure exponent of the burning rate, n, does not change as T_0 changes, although coefficient, a, decreases as T_0 decreases.

The low burning rate of the AN composite propellant is generally explained by endothermic phase change from solid to liquid which produces a thick melt layer on the burning surface of the propellants. This melt layer is believed to inhibit heat feedback from the gas phase to the burning surface, thus decreases the burning rate of the propellant. However, an analysis in the following section revealed that melt layer does not play major role on determination of the burning rates.

Analysis on Combustion Mechanisms

There are many combustion models on solid rocket propellants, such as Thermal Layer model[23], GDF model[28,29], Hermance's model[30], BDP model[31,32], PEM model[33,34], etc.. Major effort has been taken to build a numerical code which takes into account many details of phenomenological descriptions especially after Hermance[30]. In order to understand and explain the overall mechanism of combustion, however, the GDF model is still believed to be a good starting point[35].

The GDF model first assumes steady-state combustion. The propellant matrix consists of oxidizer and binder portion, and these are distributed isotropically in the matrix. Physical properties of the solid phase are assumed constant in space and time.

It has been observed that there is a melt layer on the burning surface of AN composite propellants[23,24,36]. In order to verify the phenomena within the melt layer, let τ_m be residence time in the melt layer. Then,

$$\tau_m = (\rho_m/\rho_s)(L_m/r_b)$$
$$\sim L_m/r_b \tag{2}$$

where ρ_m and ρ_s are densities of melt layer and solid phase, respectively. L_m is thickness of the melt layer and r_b is

burning rate. According to experimental data of Brewster, et.al.[1], L_m and r_b are 50 mm and 0.5 mm/sec, respectively. Therefore, the residence time of the melt layer is in the order of 10^{-1} sec.

On the other hand, a procedure similar to the GDF model yields

$$\tau_m \sim d^2/D_m \qquad (3)$$

where d and D_m are oxidizer diameter and diffusion coefficient, respectively, and details of the derivation is given in the following section. Brewster, et.al. gives d $\sim 6 \times 10^{-4}$ m. D_m is in the order of 10^{-9} m^2/sec [37]. Therefore, τ_m is in the range of 10^1 sec.

Equation.(3) is very sensitive to d since it is proportional to d^2, and actual d of the propellant has distribution so that the residence time changes both in time and space within the combustion wave structure. However, the result of this simple analysis indicates that the time required for complete diffusion of oxidizer and fuel components can be much greater than its residence time in the melt layer. Consequently, no diffusion or mixing processes were considered within the melt layer. No reactions between liquefied AN and HTPB are also assumed within the melt layer since decomposition of AN takes place just above the burning surface[23-25].

Hence, the burning surface of the propellant is defined just above the melt layer so the liquefaction is treated as a condensed phase reaction. Above the burning surface, fuel and oxidizer gas pockets produced by decomposition of both AN and HTPB are assumed to exist as shown in Figure 5. Heterogeneity in the gas phase in which exothermic reactions generate heat feedback to the burning surface is taken into account.

It is interesting to note that experimental investigations done by Whittaker & Barham[36], Kubota, et.al.[4], Alspach[38] and Brewster et.al.[1] show an apparent temperature step just above the burning surface as shown in Figure 6. Though other investigators suppose this as a gas phase reaction zone, Brewster et.al. explain this as a "build-up" of some residual materials. In their experiments, the thickness of the build-up layer is the same order of that of melt layer if a microthermocouple junction is placed on the AN crystal. The thickness of the "build-up"

layer reduces to 1/4 when the junction is on the "fill" region which is fuel-rich pocket propellants. If it is a carbonaceous build-up, then the layer must be thicker when the junction is on the fuel-rich region. Consequently, it is not likely that the build-up is carbonaceous materials.

Brill et.al.[25] showed that decomposition reaction of AN is very complicated and even may consist of re-combination of ammonia and nitric acid. Though the first stage decomposition is believed as decomposition into ammonia and nitric acid molecules, their experiments confirmed complication of decomposition and reaction processes of AN. On the other hand, Alspach's data clearly show the existence of a two stage reaction in the gas phase, one just above the burning surface which corresponds to "build-up" temperature and the other far from the burning surface. Although data of Kubota et.al[4] are not conventional AN propellants, these also show the same tendency in general. Therefore, it is concluded that no matter how the first stage gas phase reaction is completed, it nevertheless exists. Since AN consists of ammonia and nitric acid, NO_2 and N_2O may be considered as intermediate combustion products as in case of double-base propellant combustion. Unfortunately, detailed gas phase reactions are difficult to measure by experiments. Further investigations are required to verify the reaction processes of the combustion wave of the propellant.

Although mechanisms of these reaction zones are still to be investigated, it also can be possible to treat overall mechanism as a combination of monopropellant flames of AN and diffusion flames of decomposition gases of AN and binder. As a first approximation, the AN monopropellant flame is assumed to be in the vicinity of the burning surface so that it is considered as a burning surface reaction.

The assumptions made above enable us to use GDF model with collapsed AP monopropellant flames, which is mainly concerned AP composite propellant combustion[29]. Thus, following procedure is essentially the same as GDF model itself although physical meanings of each parameter and coefficient are different.

Total characteristic length of combustion wave, L, is assumed as a linear summation of

that of physical diffusion, L_d, and chemical reaction, L_c.

$$L = L_d + L_c \qquad (4)$$

Next, heat flux in vicinity of the burning surface is considered. Radiative heat transfer from the gas phase to the burning surface is neglected in this case. Then,

$$(\lambda_g \Phi_L)/L = \rho_p r_b c_p \Psi_L \qquad (5)$$

where 1 is thermal conductivity, ρ is density and c is specific heat. Subscript g denotes gas phase and p denotes propellant liquid phase. Φ_L and Ψ_L are defined as

$$\Phi_L = T_g \cdot T_s \qquad (6)$$

$$\Psi_L = T_s \cdot T_o \cdot Q_s/c_p \qquad (7)$$

where T_g is gas phase temperature, T_s is burning surface temperature and Q_s is heat generated on the burning surface. Therefore, burning rate is expressed by Eq.(5) once L is properly estimated. However, care has to be taken that primary flame which corresponds to AP monopropellant flame must be collapsed so as to be approximated as a surface reaction term.

Estimation of L_d and L_c is obtained as the same manner as GDF model. In case of L_d is dominant in the combustion wave,

$$L_d = u_g \tau_d \qquad (8)$$

where u_g and t_d are gas velocity and residence time in the gas phase, respectively. Simplified mass conservation for steady-state combustion yields,

$$u_g = \rho_p r_b / \rho_p \qquad (9)$$

In order to estimate τ_d, mass and size of the decomposed gas pocket is considered as

$$\rho_g d^3 = \mu \qquad (10)$$

where μ, d, R are mass, scale and gas constant of the gas pocket, respectively. Let D_g be a diffusion coefficient. Then, Fick's 1st law gives

$$J = -D_g (\partial C/\partial y) \qquad (11)$$

where J is molar number of diffusive matter per unit surface and time. C is concentration and y is direction of diffusion. J is represented with using μ as

$$J = (\mu/M)(d^2/\tau_d) \qquad (12)$$

where M is molecular mass. Spacial distribution of decomposed gases just above the burning surface is approximated as a

linear function of distance. Then, $(\partial C/\partial y)$ is expressed as

$$(\partial C/\partial y) - -(\mu/M)/d^4 \qquad (13)$$

Substituting Eqs. (12) and (13) into Eq. (11), one can obtain an estimation

$$\tau_d - d^2/D_g \qquad (14)$$

Now, Eqs. (9), (10), and (14) are substituted into Eq. (8),

$$L_d = (\mu^{2/3}/D_g) \ (\rho_p r_b/\rho_g^{3/5}) \qquad (15)$$

In order to eliminate r_b in Eq. (15), Eq. (5) is substituted. Then L_d is expressed as

$$L_d = \{\lambda_g \Phi_L/(c_p \Psi_L)\}^{1/2}$$
$$x \ (\mu/r_g^{5/6} D_g^{1/2}) \qquad (16)$$

Next, characteristic length for chemical reaction L_c is estimated. Using residence time for chemical reaction, τ_c,

$$L_c = (\rho_p r_b/\rho_p)\tau_c \qquad (17)$$

Overall reaction is supposed as a one-step, second order reaction as

Oxidizer + Fuel -> Product

then the τ_c becomes

$$\tau_c^{-1} = (1-\varepsilon)^2 \rho_g Z_g \exp(-E_g/RuT_g) \qquad (18)$$

where e is mass fraction of decomposed gases, Z_g is pre-exponential factor, E_g is activation energy and Ru is universal gas constant. Although molecular corrosion theory gives Z_g as a function of $Tg^{1/2}$, this term is treated as a constant. Substituting Eq.(18) into Eq.(17) and taking limit $\varepsilon \to 0$,

$$L_c = (\rho_p r_b/\rho_p)$$
$$\{\rho_g Z_g \exp(-E_g/RuT_g)\}^{-1} \qquad (19)$$

Eq. (19) is substituted into Eq. (5).

$$L_c = \{\lambda_g \Phi_L / c_p \Psi_L\}^{1/2}$$
$$/[\rho_g\{Z_g \exp(-E_g/RuT_g)\}^{1/2}] \qquad (20)$$

To obtain the GDF expression of the burning rate characteristics, Eqs. (4), (5), (16) and (20) are combined and yield

$$1/r_b = \rho_p c_p \lambda_g \{\Phi_L / c_p \Psi_L)\}^{1/2}$$
$$x \ \{(\mu/\rho_g^{5/6} D_g^{1/2})$$
$$+ 1/[\rho_g Z_g^{1/2}$$
$$x \ \exp(-E_g/2RuT_g)]^{-1}\} \qquad (21)$$

Suppose the change of T_s as pressure changes is sufficiently small. Then,

$$\rho_g^{5/6} D_g^{1/2} = (\rho_g D_g)^{1/2}\rho_g^{1/3}$$

$$\sim \rho_g^{1/3} \qquad (22)$$

Using Eq. (22) and perfect gas equation of state, and approximate all terms other than r_b and ρ_g be constants, we obtain the final form of the GDF expression of the burning rate as

$$P_c / r_b = a* + b* \, P_c^{2/3} \qquad (23)$$

where a* and b* are constants represent effects of chemical reaction and physical diffusion on the burning rate characteristics. Note that a* includes reaction term which generates heat in the gas phase, while b* does not include any reaction terms. As a result, pressure exponent of the burning rate does not become less than 1/3 in GDF expression.

Experimental data shown in Figure 4 are replotted in Figure 7 using Eq.(23). Despite scatter in the data, it agrees well with the modified GDF model described above. Thus, the overall combustion mechanism of AN composite propellant is explained as a combination of physical diffusion and chemical reaction.

As Eq. (23) shows, burning rate of the propellant is controlled by a* and b* in the GDF model. Figure 8 indicates the characteristics of these two parameters as T_o changes. The order of a* is 10^1 through T_o is changes from 243 to 343 K while that of b* maintained 10^{-1} to 10^0. Thus, it is clear that a* is the dominant parameter on determining the overall burning rate characteristics of the propellant .

Temperature Sensitivity Analysis

Equation (23) derives that temperature sensitivity of the propellant can be decomposed into the sensitivities of a* and that of b*. These parameters are defined as follows:

$$\sigma_{p,a*} = \partial a* / \partial T_o \qquad (24)$$

$$= -15.0 \, \% \, \text{atm} (\text{mm} / \text{sec K})^{-1}$$

$$\sigma_{p,b*} = \partial b* / \partial T_o \qquad (25)$$

$$= -0.56 \, \% \, \text{atm} (\text{mm} / \text{sec K})^{-1}$$

Both terms have sensitivity to T_o, although, the order of $\sigma_{p,a*}$ is much greater than that of $\sigma_{p,b*}$ as shown. Therefore, the temperature sensitivity of AN composite propellant is considered to be chemical reaction controlled just as the overall burning rate is chemical reaction dominant.

If the mechanism of temperature sensitivity is chemical reaction dominant, then it can be supposed that the mechanism is similar to that of double-base propellants in which flame structure is pre-mixed, no diffusion flame is observed and chemical reactions determine the burning rate of the propellants. Now, σ_p is expressed as[39-42]

$$\sigma_p = \Phi + \Psi \qquad (26)$$

$$= (\Omega + \Theta + \Psi) / 2$$

where Φ and Ψ are temperature sensitivity of the gas phase and the condensed phase, respectively. Then each terms in Eq. (27) is defined and expressed as

$$\Omega = (\partial T_g / \partial T_o)_p \, \{E_g / (Ru \, T_g^2)\} \qquad (28)$$

$$\Theta = \{(\partial T_g / \partial T_o) - (\partial T_s / \partial T_o)\}_p$$
$$/ (T_s - T_o - Q_s / c_p) \qquad (29)$$

$$\Psi = \{1 - (\partial T_s / \partial T_o)\}_p$$
$$/ (T_s - T_o - Q_s / c_p) \qquad (30)$$

If the burning rate is expressed as an Arrhenius type reaction at the burning surface temperature, we obtain

$$(\partial T_s / \partial T_o)_p = \sigma_p \, Ru \, T_s^2 / E_s \qquad (31)$$

Estimated values of T_s, Q_s, E_s and c_p are 600 K[23,24], -1180 kJ/kg[1], 169.3 kJ/kmol[43] and 1.90 kJ/kg[43], respectively. By using Eqs. (26) and (30), results of temperature sensitivity analysis shown in Figure 9 was obtained. It is clear that Φ is a dominant factor on determining the overall temperature sensitivity of the propellant burning rate.

Although low burning rate of AN composite propellants is caused by the melt layer which acts as a thermal barrier for heat flux from the gas phase, characteristics analysis of the temperature sensitivity described above revealed that the gas phase chemical reaction is the dominant factor on temperature sensitivity determination. Thus, liquefaction of AN does not play an important role on temperature sensitivity of AN composite propellants.

Conclusions

An AN composite propellant was proposed as a gas generator propellant for GHR. Theoretical calculations showed a 25 seconds specific impulse increase when compared with AN solid propellant rockets. The combustion mechanism of the propellant was

5

American Institute of Aeronautics and Astronautics

investigated. Results of the investigation showed that the burning rate characteristics of the propellants can be explained with a GDF prediction. It was shown quantitatively that the gas phase chemical reactions are a dominant factor on determining the burning rate characteristics. Analysis based on the GDF model showed that temperature sensitivity of the propellant burning rate is also a chemical reaction dominant. On the other hand, analysis based on the double-base-like reaction controlled mechanism showed that temperature sensitivity in the gas phase is a dominant factor. Thus, mechanisms of an AN composite propellant combustion are explained as a gas phase chemical reaction dominant phenomena.

References

[1] Brewster, M. Q., Sheridan, T. A. and Ishihara, A., "Ammonium Nitrate-Magnesium Propellant Combustion and Heat Transfer Mechanisms", Journal of Propulsion and Power, Vol. 8, No. 4, 1992, pp. 760-769.

[2] Korting, P. A. O. G., Zee, F. W. M. and Meulenbrugge, J. J., "Combustion Characteristics of Low Flame Temperature Chlorine-Free Composite Solid Propellants", Journal of Propulsion and Power, Vol. 6, No. 3, 1990, pp. 150-155.

[3] Miyauchi, K. and Kubota, N., "Combustion of A³NPL Propellants", Technical Report TR-A-1008, Technical Research and Development Institute, JDA, Tokyo, Japan, 1987(in Japanese. Abstract available in English).

[4] Kubota, N. Katoh, K. and Nakashita, G., "Combustion Mechanism of GAP/AN Propellants", Proceedings of the 22nd International Annual Conference of ICT, 1991, pp. 42.1-42.9.

[5] Mieadema, J. R., Klein, A. J. J. and Zee, F. W. M., "Particle Size Distribution Effect on Burn Rate of Ammonium Nitrate Based Propellant", AIAA paper 95-2714.

[6] Kuwahara, T. and Shinozaki, N., "Ignition Characteristics of AN/Al/AP Composite Propellants", Kayaku Gakkaishi, Vol. 55, No. 3, 1994 (in Japanese. Abstract available in English).

[7] Miyauchi, I., Yamasaki, T., Kuwahara, T. and Kubota, N., "Combustion of A³NPL Propellant", Kogyokayaku Kyokaishi, Vol. 48, No. 2, 1987, pp.77-84 (in Japanese. Abstract available in English).

[8] Greiner, B and Frederick, R. A. Jr., "Experimental Investigation of Ammonium Nitrate Propellant Ballistic Properties", AIAA Paper 96-3275.

[9] Encyclopedia of Explosives and Related Items, PATR 2700, 8, Armament Research and Development Command, U.S. Army, AD A057-762, 1978, pp. A311-A354.

[10] Klager, K. and Zimmerman, G. A., "Steady Burning Rate and Affecting Factors: Experimental Results", in DeLuca, L., Price, E. W. and Summerfield, M., Eds., Nonsteady Burning and Combustion Stability of Solid Propellants, Progress in Astronautics and Aeronautics, Vol. 143, AIAA, 1992, pp. 59-109.

[11] Cohen, J., Landers, L. C., and Lou, R. L., "Minimum-Response-Delay Controllable Solid-Propellant Gas Generators", Journal of Spacecraft, Vol. 14, No. 5, AIAA, 1977, pp. 310-314.

[12] Kubota, N., Yano, Y., Miyata, K., Kuwahara, T., Mitsuno, M. and Nakagawa, I., "Energetic Solid Fuel for Ducted Rockets (2)", Propellants,Explosives,Pyrotechnics 16, 1991, pp.287-292.

[13] Frederick, R. A. Jr., and Komai, I., "Variable Exponent Solid Propellant for Gas Generators", Journal of Propulsion and Power, Vol. 12, No. 3, 1996.

[14] Aerojet Solid Propulsion, Aerojet Tech Systems, Martin Marietta Aerospace, "Hybrid Propulsion Technology Program Phase1-Final report", Vol. 1, Executive Summary, Contract No. NAS8-37777, 1989.

[15] Atlantic Research Corp., Virginia Propulsion Division, "Hybrid Technology Program Phase 1-Final Report", Vol. 1, Executive Summary, Contract No. NAS8-37775, 1989.

[16] Culver, D. W. and Mueggenberg, H. H., "AFT Mounted Gas/Liquid Injector Technology for Gas Generator Cycle Hybrid Rockets", AIAA Paper 91-2518, 1991.

[17] Culver, D. W., "Comparison of Forward and Aft Injected Hybrid rocket Boosters", AIAA Paper 91-2586, 1991.

[18] Cohen, N. S. and Strand, L. D., "Hybrid Propulsion Based on Fluid-Controlled Solid Gas Generators", AIAA Paper 93-2550, 1993.

[19] Kuwahara, T., Mitsuno, M., Odajima, H., Kubozuka, S., and Kubota, N., "Combustion Characteristics of Gas Hybrid rockets (1)", AIAA Paper 94-2880, 1994.

[20] Kuwahara, T., Mitsuno, M. and Odajima, H., "Combustion Characteristics of Gas Hybrid Rockets (2)", AIAA Paper 95-3083, 1995.

[21] Mahaffy, K. E., Harting, G. C., Bates, R., Walsh, R. and Hansen, C., "Hybrid Propulsion for Air Force Application Study", PL-TR-96-3018, Phillips Laboratory, US Air Force, 1996

[22] "AIAA Hybrid Rockt Technical Committee Meeting Minutes", 1996 Winter Steering Committee Meeting, Reno, NV, 1996.

[23] Chaiken, R. F., "Thermal Layer Mechanism of Combustion of Solid Composite Propellants: Application of Ammonium Nitrate Propellants", Combustion and Flames, Vol. 3, 1959, pp. 285-300.

[24] Anderson, W. H., Bills, K. W., Mishuck, E., Moe, G. and Shultz, R. D., "A Model Describing Combustion of Solid Composite Propellants Containing Ammonium Nitrate", Combustion and Flames, Vol. 3, 1959, pp. 301-317.

[25] Brill, T. B., Brush, P. J. and Patil, D. G., "Thermal decomposition of Energetic Materials 58. Chemistry of Ammonium Nitrate and Ammonium Dinitrate Near the Burning Surface Temperature", Combustion and Flame, Vol. 92, 1993, pp. 178-186.

[26] Chen, J. K. and Brill T. B., "Chemistry and Kinetics of Hydroxyl-Terminated Polybutadiene(HTPB) and Diisocyanate-HTPB Polymers During Slow Decomposition and Combustion-Like Conditions", Combustion and Flame, Vol. .87, 1991, pp. 217-232.

[27] Gordon, S. and McBride, B. J., "Computer Program for Calculation of Complex Equilibrium Compositions, Rocket Performance, Incident and Reflected Shocks and Chapman-Jougeuet Detonations", NASA SP-273, 1971.

[28] Steinz, J. A., Stang, P. L. and Summerfield, M., "The Burning Mechanism of Ammonium Perchlorate-Based Composite Propellants", AIAA Paper 68-658, 1968.

[29] Steinz, J. A., Stang, P. L. and Summerfield, M., "The Burning Mechanism of Ammonium Perchlorate-Based Composite Propellants", AMS Report No. 830, Princeton Univ., 1969, AD 688-944.

[30] Hermance, C. E, "A Model of Composite Propellant Combustion Including Surface Heterogeneity and Heat Generation", AIAA Journal, Vol. 4, No. 9, 1966, pp. 1629-1637.

[31] Beckstead, M. W., Derr, R. L. and Price, C. F.," A Model of Composite Solid Propellant Combustion Based on Multiple Flames", AIAA Journal, Vol. 8, No. 12, 1970, pp. 2200-2207.

[32] Beckstead, M. W., Derr, R. L. and Price, C. F., "The Combustion of Solid Monopropellants and Composite Propellants", Thirteenth (International) Symposium on Combustion, Combustion Institute, Pittsburgh, PA, 1971, pp. 1047-1056.

[33] Glick, R. L., "On Statistical Analysis of Composite Solid Propellants Combustion", AIAA Journal, Vol. 12, 1974, pp. 384-385.

[34] Glick, R. L., "Distribution Functions for Statistical Analysis of Monodisperse Composite Solid Propellant Combustion", AIAA Journal, Vol. 14, 1976, pp. 1631-1633.

[35] Ramohalli, K. N. R., "Steady-State Burning of Composite Propellants under Zero Cross-Flow Situation", Kuo, K. K. and Summerfield, M., Eds., Fundamentals of Solid-Propellant Combustion, Progress in Astronautics and Aeronautics, Vol. 90, AIAA, 1984, pp. 409-477.

[36] Whittaker, A. G. and Barham, D. C., "Surface Temperature Measurements on Burning Solids", The Journal of Physical Chemistry, Vol. 68, No. 1, 1964, pp.196-199.

[37] Gray, D. E. Ed., "American Institute of Physics Handbook", McGraw-Hill, 1963.

[38] Alspach, D. A., "Temperature Measurements Through a Solid-Propellant Combustion Wave Using Imbedded Fine Wire Thermocouples", AL-TR-89-085, U.S. Air Force Astronautics Laboratory, AD-A218 642, 1990.

[39] Kubota, N. and Ishihara, "Analysis of the Temperature Sensitivity of Double-Base Propellants", Twentieth Symposium (International) on Combustion, The Combustion Institute, Pittsburgh PA, 1984, pp. 2035-2041.

[40] Kubota, N., "Temperature Sensitivity of Solid Propellants and Affecting Factros: Experimental Results", in DeLuca, L., Price, E. W. and Summerfield, M., Eds., Nonsteady Burning and Combustion Stability of Solid Propellants, Progress in Astronautics and Aeronautics, Vol. 143, AIAA, 1992, pp. 11-143.

[41] Cohen, N. S. and Flanagan, D. A., "Mechanisms and Models of Slid-Propellant Burn Rate Temperature Sensitivity: A Review", AIAA Journal, Vol. 23, No. 10, 1985, pp. 1538- 1547.

[42] Summerfield, M., Caveny, L. H., Battista, R. A., Kubota, N., Gostintsev, Yu, A. and Isoda, H., "Theory of Dynamic Extinguishment of Solid Propellants with Special Reference to Nonsteady Heat Feedback Law", Journal of Spacecraft and Rocket, Vol. 8, No. 3, 1971, pp. 251-258.

[43] Taylor, J. and Sillito, G. P., "The Use of Ammonium Nitrate as a Solid Fuel to Provide Gas for Propulsive Purposes", Third Symposium(International) on Combustion, Flame and Explosion Phenomena, William and Wilkins, 1949, pp. 572-579.

Table-1
Burning Rate Parameters of the AN Composite Preopellants

To(K)	a	n
243	0.0255	0.887
293	0.0315	0.887
343	0.0400	0.887
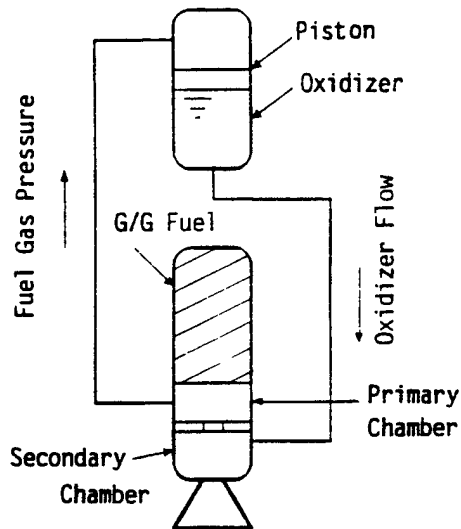
Figure 1 Schematic of Gas Hybrid Rockets

Figure 3 Specific Impulse Characteristics of GHR

Figure 2 Performance Comparison of GHR and Solid Rockets
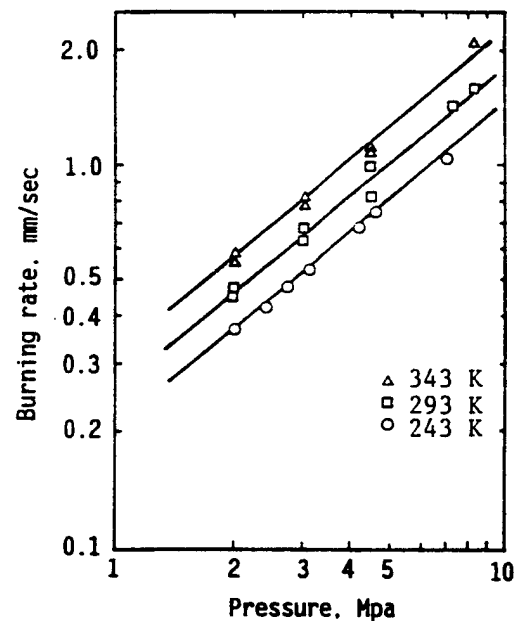
Figure 4 Burning Rate Characteristics of Typical AN Composite Propellants[3,7]

Solid Phase   Surface Melt Layer   Gas Phase

Chemical Reaction Length. Lc

AN Crystal

Gas Pocket Diameter. d

Physical Diffusion Length. Ld
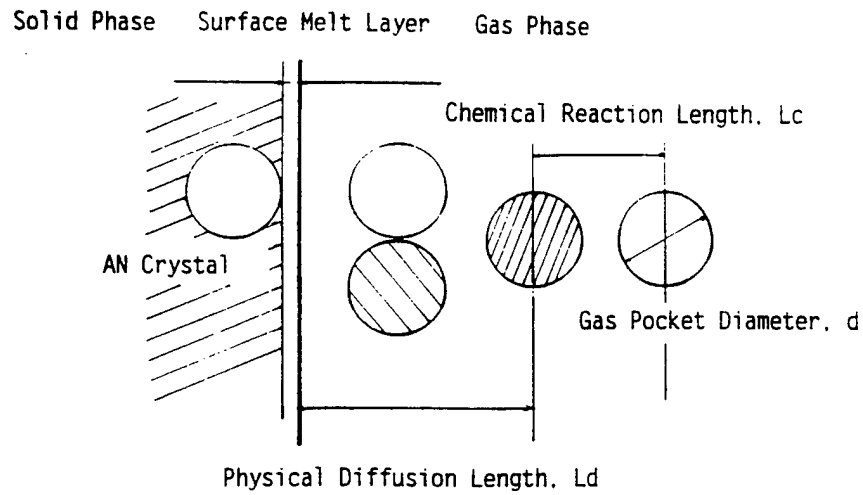
Figure 5   Schematic of AN Composite
                Propellant Combustion

AN Composite Propellant Temperature Profile at 200 psia

Diameter of the Thermocouple Junction = 150 um

Ts = 600 K
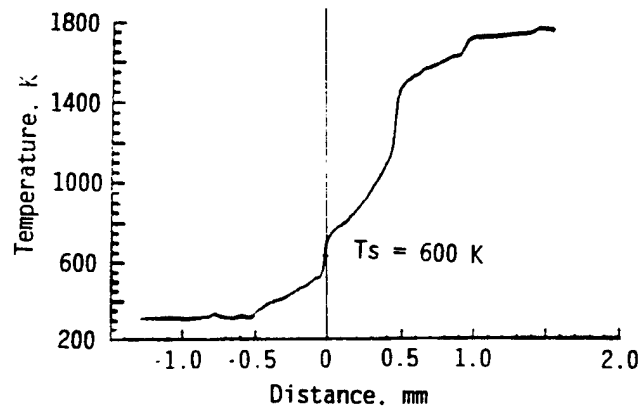
Figure 6   Typical Temperature Profile
                of AN Composite Propellants[38]
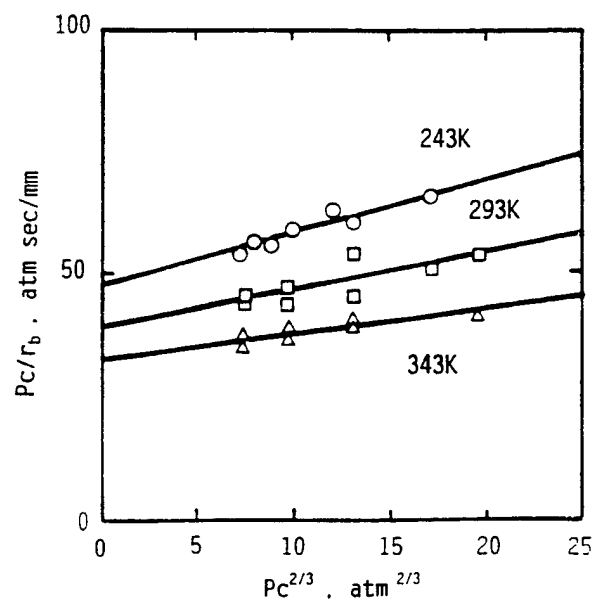
Figure 7   GDF plot of the AN composite Propellants
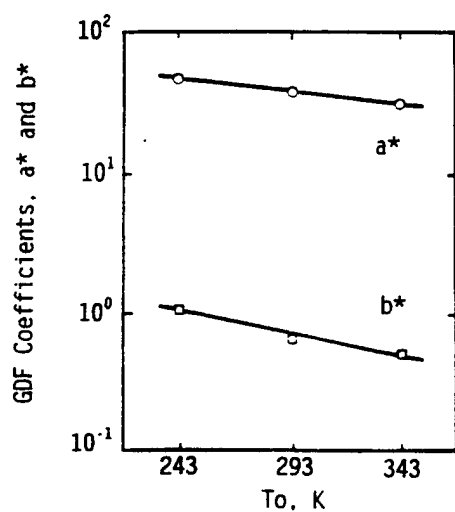
Figure 8   Chemical Reaction and Physical
               Diffusion Parameters
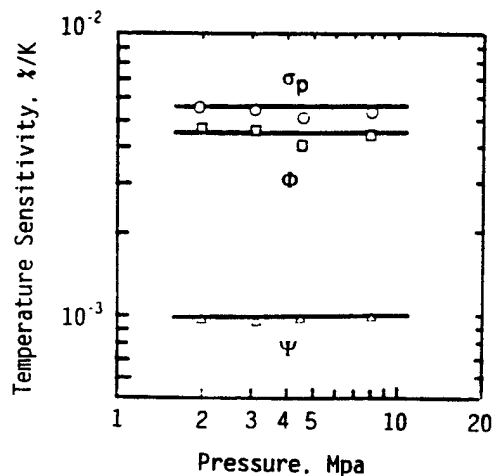
Figure 9   Mechanisms of Temperature
               Sensitivity of the Propellants

AIAA 95-2582

Numerical Analysis of a Nonlinear Burn Rate Equation

Rodney D. Bishop
Sverdrup Technology, Inc.
MSFC Group
620 Discovery Drive
Huntsville, AL 35806

Dr. Robert A. Frederick, Jr.
The University of Alabama in Huntsville
Propulsion Research Center
Huntsville, AL 35899

31st AIAA/ASME/SAE/ASEE
Joint Propulsion Conference and Exhibit
July 10-12, 1995/San Diego, CA

NUMERICAL ANALYSIS OF A NONLINEAR BURN RATE EQUATION

Rodney D. Bishop[*]

Sverdrup Technology, Inc., MSFC Group

620 Discovery Drive, Huntsville, AL 35806

Robert A. Frederick, Jr., Ph.D.[†]

The University of Alabama in Huntsville, Propulsion Research Center

Huntsville, AL 35899

In this paper, a nonlinear solid rocket propellant burn rate equation is developed. Temperature sensitivity coefficients are produced based on the nonlinear equation. Modeling of the solid propellant burn rate with the nonlinear equation is compared with equations used to model the solid propellant burn rate. The analysis compares solid propellant burn rate data produced by the Beckstead, Derr, Price Multiple Flame Model. This data is taken at nine pressures and three temperatures. This paper studies the effects of the number of pressures used and the propellant particle size. Also, a random error is added to the data points. It is shown that a higher order version of the nonlinear burn rate equation with fewer data points is a better model than the current models with more data points.

NOMENCLATURE

a   pressure coefficient

c^* characteristic velocity

D^2 coefficient of determination

K   ratio of propellant burning surface area to nozzle throat area

n   pressure exponent

P   chamber pressure

r   solid propellant burn rate

S_r sum of the square of the residuals uncertainty around the mean

$S_{y/}$ standard error of the estimate

T   temperature

α empirical constant

β empirical constant

ε residual

π_c temperature sensitivity of characteristic velocity

π_K temperature sensitivity of pressure at constant motor geometry

ρ_g density of the combustion gases

ρ_p density of the propellant

σ_p temperature sensitivity of burn rate at constant pressure

INTRODUCTION

The Ducted Rocket Engine

A ducted rocket engine (DRE) is an engine that uses air as an oxidizer and takes its fuel from a gas generator. The air and the fuel mix in the combustion chamber and are ejected through a nozzle. A DRE requires a flight speed of about Mach 2 to operate efficiently. To get a ducted rocket engine up to this operating speed, a solid propellant boost motor is used. The boost motor casing serves as the combustion chamber for the air and fuel mixture. Figure 1 shows a DRE with a solid boost motor attached.

Accurately describing the burn rate of the propellant is important when calculating the performance of the boost motor. If the burning rate relationship used to calculate performance varies significantly from the actual ballistic performance of the boost motor the performance will not be accurately predicted. For example, if the temperature of the boost motor increases, the burn rate increases. The effect of the initial propellant temperature as well as chamber

---

[*] Engineer II, Thermal and Fluids Analysis Section. Member, AIAA

[†] Asst. Professor, Dept. of Mech and Aero Engr. Member, AIAA.

pressure influence the propellant burning rate. and hence the motor performance. and are therefore. important design considerations for solid boost motors.

rate data can take a nonlinear shape in a log-log plot of burn rate versus chamber pressure. The dashed line represents a curve fit of the data if St. Robert's Law is used as the model equation.
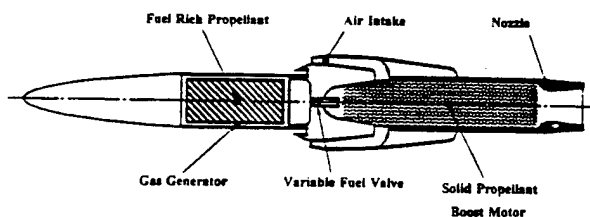
Figure 1 A ducted rocket engine with a solid rocket propellant boost motor.
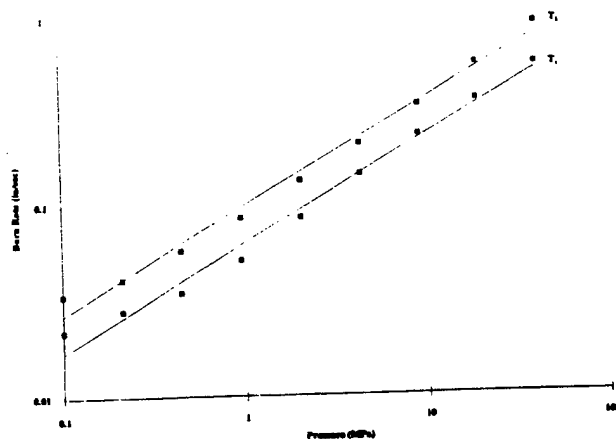
Figure 2 Propellant burn rate characteristics.

Solid Propellant Burn Rate

The most basic form of the solid propellant burn rate expression. called St. Robert's Law[20] is

$$r = aP^n \tag{1}$$

In this equation. the pressure coefficient and exponent are assumed constants so the burn rate is a function of chamber pressure only. The pressure coefficient can be a function of the initial temperature of the propellant and can be approximated as

$$a = a_0 exp\left[\sigma_P(T - T_o)\right] \tag{2}$$

giving the burn rate expression the final form of

$$r = a_0 exp\left[\sigma_P(T - T_o)\right]P \tag{3}$$

Since the pressure exponent is assumed constant. and the pressure coefficient is constant for a given temperature. the family of burn rate curves are straight and parallel for different initial propellant temperatures when plotted in the $\log(P) \log(r)$ plane. In reality the actual burn rate lines can take a nonlinear form. Figure 2 demonstrates how the burn

From the literature[16], the effects of making the burn rate pressure exponent a function of temperature can be predicted. By making the pressure exponent a linear function of temperature the burn rate lines are no longer parallel. However, they are still linear because the pressure coefficient and pressure exponent are solely a function of temperature.

The effect of the initial propellant temperature on motor performance is shown in Figure 3 where chamber pressure is shown as a function of time at two different temperatures. At the higher temperature the propellant burns faster which results in higher motor pressures. Correspondingly at the lower temperature the propellant will take longer to burn and will burn at a lower pressure.

Since the linear expressions do not correlate exactly with the propellant burn rate curves, error will naturally be introduced when using this expression to predict motor chamber pressure. It is proposed that a nonlinear solid propellant burn rate expression be established and evaluated. The nonlinear expression will describe the propellant burn rate as a function of pressure and temperature. Evaluations will be completed to see if the burn rate is more accurately

portrayed and can lead to better prediction of the performance of the ducted rocket boost phase. Care must be taken, however, that the new expressions are not so "flexible" that they fit "noise" rather than the true burning rate curves of the propellant.
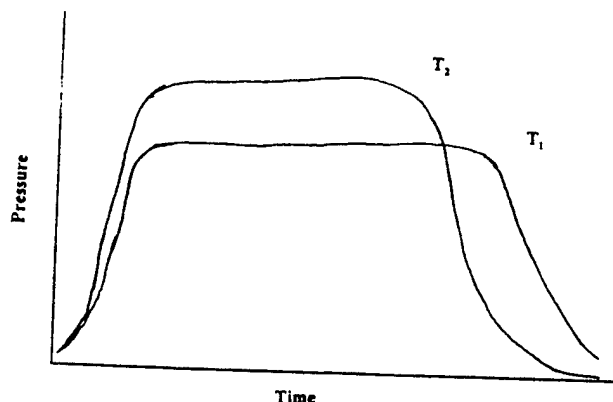
Figure 3 Effects of the initial propellant temperature on the solid propellant burn rate.[20]

First the new burning rate expression will be proposed. Predictions calculated with the Beckstead Derr Price combustion model[19] will be applied to the new expression. The effect of the order of the nonlinear expression on the least-squares residual will be calculated as a function of burn rate measurement uncertainty, number of pressure intervals in the burning rate data, and will be applied to propellant burn rate. Finally, the results will be presented and evaluated to determine if any improvements have been realized in solid propellant burn rate prediction.

A REVIEW OF TEMPERATURE SENSITIVITY EXPRESSIONS FOR SOLID PROPELLANTS

Temperature Sensitivity Expressions

There are two coefficients commonly used in solid propellant temperature sensitivity theory. The first is the temperature sensitivity of burning rate at a constant chamber pressure[6] and is defined as

$$\sigma_P = \left(\frac{\partial \ln r}{\partial T}\right) \qquad (4)$$

This is the percent change of burn rate per degree change in temperature and is a propellant parameter. Here the data are taken at constant pressure. Propellant strand burner test data are used to determine the burn rate to calculate the temperature sensitivity of burn rate.

The second coefficient is the temperature sensitivity of pressure and is defined in Equation 5.[6]

$$\pi_K = \left(\frac{\partial \ln P}{\partial T}\right) \qquad (5)$$

This is the percent change of the log pressure per degree change in initial propellant temperature. A motor firing is used to determine the temperature sensitivity of pressure since it is defined for a constant motor geometry which is defined as the ratio of propellant burning surface area to the nozzle throat area.

A third temperature related coefficient has also been defined. It is the temperature sensitivity of the characteristic velocity for a constant motor geometry[14].

$$\pi_c = \left(\frac{\partial \ln c^*}{\partial T}\right)_K \qquad (6)$$

To make use of strand burner rate data for motor pressure predictions, a relationship between the temperature sensitivity of burn rate, σ_P, and the temperature sensitivity of pressure, π_K, coefficients must be described. This could allow early evaluation of candidate propellant formulations and potentially reduce testing costs. Several expressions have been proposed by the researchers. A summary of the ideas previously presented is outlined in Table 1.

For this work, the Glick and Brooks term will be applied in the development of the nonlinear equation.

DEVELOPMENT OF THE NONLINEAR BURN RATE EXPRESSION

To better describe actual propellant burning rate data, a nonlinear burn rate expression will be developed and evaluated to enhance the performance

3

prediction of solid propellant rocket motors. This will maximize the use of strand burner tests allowing for a close approximation of the actual burn rate curves. To obtain a curved fit through the given data a least-squares multiple polynomial regression will be used to describe the burn rate as a function of both pressure and temperature.

Table 1 Summary of Temperature Sensitivity Coefficients

Author	σ_p	π_K
Geckler and Sprenger[7]	$\left(\frac{\partial \ln r}{\partial T}\right)_P$	$\left(\frac{1}{1-n}\right)\sigma_P$
Glick and Brooks[9]	$\left(\frac{\partial \ln r}{\partial T}\right)_P$	$\left(\frac{1}{1-n}\right)(\sigma_P + \pi_c)$
Gaunce and Osborne[5]	$\left(\frac{\partial \ln r}{\partial T}\right)_P$	$\frac{1}{1-n}\left\{\left[\frac{\partial(\rho_p - \rho_g)}{\partial T_i}\right]_K + \pi_c + \left(\frac{\partial \ln a}{\partial T_i}\right)\right\}$ $+\frac{1}{1-n}\left\{+\frac{\left(\frac{\partial n}{\partial T_i}\right)_K}{\left(\frac{\partial n}{\partial T_i}\right)_P}\left[\sigma_P - \left(\frac{\partial \ln a}{\partial T_i}\right)_P\right]\right\}$
Cohen and Flanigan[4]	$\frac{\sigma_{P_1} + \sigma_{P_2}}{2}$	$\bar{\sigma}_P\left[\frac{2\ln\left(\frac{a_{22}}{a_{11}}\frac{P_2^{n_{22}}}{P_1^{n_{11}}}\frac{c_{22}^*}{c_{11}^*}\right)}{\ln\left(\frac{a_{22}}{a_{12}}\frac{a_{21}}{a_{11}}\frac{P_2^{n_{22}-n_{12}}}{P_1^{n_{11}-n_{21}}}\right)}\right]$
Komai[16] and Frederick	$\alpha + \beta \ln$	$\frac{1}{1-n_s-\beta(T_i-T_{i,s})}(\alpha + \beta \ln P + \pi_c)$

The Nonlinear Burn Rate Equation

A nonlinear burn rate equation is proposed in the form of

$$\ln(r) = \Sigma_{j=1}^{k}\left\{a_j[\ln(P)]^{j-1}\right\} \qquad (7)$$

where k will be denoted as the order of the equation and

$$a_j = a_{j,s} + \alpha_j(T - T_s) \qquad (8)$$

The burn rate, chamber pressure and initial motor temperature are assumed to be given by way of strand burner tests. The remaining constants $(a_{j,s}; \alpha_j)$ will be determined using the least-squares multiple polynomial regression.

Least-Squares Multiple Polynomial Regression

An example of the multiple polynomial regression will be developed using k = 3. Thus, Equation 7 will take the form of

$$\ln(r) = a_{1,s}[\ln(P)]^0 + a_{2,s}[\ln(P)]^1 + a_{3,s}[\ln(P)]^2$$

$$+\alpha_1\Delta T[\ln(P)]^0 + \alpha_2\Delta T[\ln(P)]^1 + \alpha_3\Delta T[\ln(P)]^2 \qquad (9)$$

which reduces to

$$\ln(r) = a_{1,s} + a_{2,s}\ln(P) + a_{3,s}[\ln(P)]^2 + \alpha_1\Delta T$$

$$+\alpha_2\Delta T\ln(P) + \alpha_3\Delta T[\ln(P)]^2 \qquad (10)$$

To apply the multiple polynomial regression, the equation is rewritten with the following substitutions.

$$\ln(r) = z, \ \ln(P) = x_1 \text{ and } \Delta T = x_2 \qquad (11)$$

Also, an error term, epsilon, is added to the right hand side so that Equation 10 will now describe the difference in the curve fit and the value predicted by the equation.

$$z = a + bx_1 + cx_1^2 + dx_2 + ex_2x_1 + fx_2x_1^2 + \varepsilon \qquad (12)$$

In this equation, epsilon is the residual which is the difference between the known burn rate and that predicted by the right hand side of the nonlinear equation. This equation is solved for the residual.

$$\varepsilon^2 = \left(a + bx_1 + cx_1^2 + dx_2 + ex_2x_1 + fx_2x_1^2\right)^2 \qquad (13)$$

The sum of the square of the error is determined by summing the right hand side over the range of known points.

$$S_r = \Sigma_{j=1}^{m}(z_j - a - bx_1 - cx_1^2 - dx_2 - ex_2x_1 - fx_2 \qquad (14)$$

The derivative of Equation 14 with respect to each unknown coefficient is taken and the results are set equal to zero. The solution to this set of equations represents a minimum sum of the squares of the error,

4

or the "best fit" of a given data set according to the definition of error given in Equation 13.

$$\frac{\partial S_r}{\partial a} = -2\sum_{j=1}^{m}(z_j - a - bx_1 - cx_1^2 - dx_2 - ex_2x_1$$

$$-fx_2x_1^2)_j = 0 \qquad (15a)$$

$$\frac{\partial S_r}{\partial b} = -2\sum_{j=1}^{m} x_1(z_j - a - bx_1 - cx_1^2 - dx_2 - ex_2x_1$$

$$-fx_2x_1^2)_j = 0 \qquad (15b)$$

$$\frac{\partial S_r}{\partial c} = -2\sum_{j=1}^{m} x_1^2(z_j - a - bx_1 - cx_1^2 - dx_2 - ex_2x_1$$

$$-fx_2x_1^2)_j = 0 \qquad (15c)$$

$$\frac{\partial S_r}{\partial d} = -2\sum_{j=1}^{m} x_2(z_j - a - bx_1 - cx_1^2 - dx_2 - ex_2x_1$$

$$-fx_2x_1^2)_j = 0 \qquad (15d)$$

$$\frac{\partial S_r}{\partial e} = -2\sum_{j=1}^{m} x_2x_1(z_j - a - bx_1 - cx_1^2 - dx_2 - ex_2x_1$$

$$-fx_2x_1^2)_j = 0 \qquad (15e)$$

$$\frac{\partial S_r}{\partial f} = -2\sum_{j=1}^{m} x_2x_1^2(z_j - a - bx_1 - cx_1^2 - dx_2 - ex_2x_1$$

$$-fx_2x_1^2)_j = 0 \qquad (15f)$$

The constant outside of the summation can be divided out. The summations are multiplied through and the equations are rearranged to give the following equations.

$$an + b\sum x_1 + c\sum x_1^2 + d\sum x_2 + e\sum\left(x_1x_2\right)$$

$$+f\sum\left(x_1^2x_2\right) = \sum z \qquad (16a)$$

$$a\sum x_1 + b\sum x_1^2 + c\sum x_1^3 + d\sum\left(x_1x_2\right) + e\sum\left(x_1^2x_2\right)$$

$$+f\sum\left(x_1^3x_2\right) = \sum\left(zx_1\right) \qquad (16b)$$

$$a\sum x_1^2 + b\sum x_1^3 + c\sum x_1^4 + d\sum\left(x_1^2x_2\right) + e\sum\left(x_1^3x_2\right)$$

$$+f\sum\left(x_1^4x_2\right) = \sum\left(zx_1^2\right) \qquad (16c)$$

$$a\sum x_2 + b\sum x_1x_2 + c\sum x_1^2x_2 + d\sum x_2^2 + e\sum\left(x_1x_2^2\right)$$

$$+f\sum\left(x_1^2x_2^2\right) = \sum\left(zx_2\right) \qquad (16d)$$

$$a\sum\left(x_1x_2\right) + b\sum\left(x_1^2x_2\right) + c\sum\left(x_1^3x_2\right) + d\sum\left(x_1x_2^2\right)$$

$$+e\sum\left(x_1^2x_2^2\right) + f\sum\left(x_1^3x_2^2\right) = \sum\left(zx_1x_2\right) \qquad (16e)$$

$$a\sum\left(x_1^2x_2\right) + b\sum\left(x_1^3x_2\right) + c\sum\left(x_1^4x_2\right) + d\sum\left(x_1^2x_2^2\right)$$

$$+e\sum\left(x_1^3x_2^2\right) + f\sum\left(x_1^4x_2^2\right) = \sum\left(zx_1^2x_2\right) \qquad (16f)$$

To solve these equations for the constants, they are arranged into a 6 x 6 matrix with a column matrix for the coefficients and a column matrix for the right-hand side.

$$\begin{bmatrix} N & \sum x_1 & \sum x_1^2 & \sum x_2 & \sum (x_1x_2) & \sum\left(x_1^2x_2\right) \\ \sum x_1 & \sum x_1^2 & \sum x_1^3 & \sum (x_1x_2) & \sum\left(x_1^2x_2\right) & \sum\left(x_1^3x_2\right) \\ \sum x_1^2 & \sum x_1^3 & \sum x_1^4 & \sum\left(x_1^2x_2\right) & \sum\left(x_1^3x_2\right) & \sum\left(x_1^4x_2\right) \\ \sum x_2 & \sum (x_1x_2) & \sum\left(x_1^2x_2\right) & \sum x_2^2 & \sum\left(x_1x_2^2\right) & \sum\left(x_1^2x_2^2\right) \\ \sum (x_1x_2) & \sum\left(x_1^2x_2\right) & \sum\left(x_1^3x_2\right) & \sum\left(x_1x_2^2\right) & \sum\left(x_1^2x_2^2\right) & \sum\left(x_1^3x_2^2\right) \\ \sum\left(x_1^2x_2\right) & \sum\left(x_1^3x_2\right) & \sum\left(x_1^4x_2\right) & \sum\left(x_1^2x_2^2\right) & \sum\left(x_1^3x_2^2\right) & \sum\left(x_1^4x_2^2\right) \end{bmatrix}$$

$$\left\{\begin{array}{c} a \\ b \\ c \\ d \\ e \\ f \end{array}\right\} = \begin{bmatrix} \sum z \\ \sum(zx_1) \\ \sum\left(zx_1^2\right) \\ \sum(zx_2) \\ \sum(zx_1x_2) \\ \sum\left(zx_1^2x_2\right) \end{bmatrix} \qquad (17)$$

To solve this equation, the 6 x 6 matrix was inverted and multiplied by the right-hand side column matrix, giving the column matrix of constants. For this paper, a spreadsheet application was used to perform these operations efficiently.

In a similar way, St. Robert's Law and the Komai-Frederick equation can be adapted for use. For St. Robert's Law, start with the original equation.

5

$$r = a_0 \exp\left[\sigma_P(T - T_0)\right] P^n \qquad (18)$$

Following the same derivation technique used earlier, take the natural log of St. Robert's Law, find the sum of the squares of the residuals, take the derivatives with respect to the constants, set the equations up into matrix form and solve them. The resulting matrix is equation is

$$\begin{bmatrix} N & \Sigma(T-T_0) & \Sigma P \\ \Sigma(T-T_0) & \Sigma(T-T_0)^2 & \Sigma P(T-T_0) \\ \Sigma P & \Sigma P(T-T_0) & \Sigma P^2 \end{bmatrix} \times \begin{Bmatrix} a_0 \\ \sigma_P \\ n \end{Bmatrix}$$

$$= \begin{bmatrix} \Sigma \ln(r) \\ \Sigma(T-T_0)\ln(r) \\ \Sigma P \ln(r) \end{bmatrix} \qquad (19)$$

In a similar manner, the matrix equation for the Komai-Frederick equation can be derived and is given to be

$$\begin{bmatrix} N & \Sigma(T-T_0) & \Sigma P & \Sigma P(T-T_0) \\ \Sigma(T-T_0) & \Sigma(T-T_0)^2 & \Sigma P(T-T_0) & \Sigma P(T-T_0) \\ \Sigma P & \Sigma P(T-T_0) & \Sigma P^2 & \Sigma P(T-T_0) \\ \Sigma P(T-T_0) & \Sigma P(T-T_0)^2 & \Sigma P^2(T-T_0) & \Sigma P^2(T-T_0)^2 \end{bmatrix}$$

$$\times \begin{Bmatrix} a_0 \\ \sigma_P \\ n \\ \beta \end{Bmatrix} = \begin{bmatrix} \Sigma \ln r \\ \Sigma(T-T_0)\ln r \\ \Sigma P \ln r \\ \Sigma P(T-T_0)\ln r \end{bmatrix} \qquad (20)$$

Note that the Komai-Frederick equation and the 1st order nonlinear equation produce the same results. The sum of the squares of the residuals equation for the Komai-Frederick equation is listed in Equation 21 while the 1st order nonlinear equation is Equation 22.

$$S_r = \Sigma_{j=1}^m \left[z_j - \ln(a_0) - \sigma_P(T-T_0) - n \ln(P) \right]$$

$$[-\beta(T-T_0)\ln(P)]_j \qquad (21)$$

$$S_r = \Sigma_{j=1}^m \left(z_j - a_1 - a_2 x_1 - \alpha_1 x_2 - \alpha_2 x_1 x_2^2 \right)_i \qquad (22)$$

A visual inspection of these two equations reveals that

$$a_1 = \ln(a_0) \qquad a_2 = n \qquad (23a.b)$$
$$\alpha_1 = \sigma_P \qquad \alpha_2 = \beta \qquad (23c.d)$$
$$x_1 = \ln(P) \qquad x_2 = (T-T_0) \qquad (23e.f)$$

Thus, the two equations are mathematically equal. This leads to the similarities in sum of the squares of the residuals as well as other results, as will be seen later in the paper.

Temperature Sensitivity Coefficients Development

When the nonlinear burn rate expression is given as Equation 7 the temperature sensitivity coefficients can be defined for use with the burn rate data available.

Temperature Sensitivity of Burn Rate at Constant Pressure

The temperature sensitivity of burn rate at constant pressure is defined as

$$\sigma_P = \left(\frac{\partial \ln r}{\partial T}\right)_P \qquad (24)$$

When Equation 7 is applied to Equation 24 the result is simply

$$\sigma_P = \left(\frac{\partial a_1}{\partial T}\right)_P + \left(\frac{\partial a_2}{\partial T}\right)_P (\ln P) + \dots + \left(\frac{\partial a_j}{\partial T}\right)_P (\ln P)^j$$

$$(25)$$

which reduces to

$$\sigma_P = \alpha_0 + \alpha_1 \ln P + \dots + \alpha_j (\ln P)^j \qquad (26)$$

or in summation form

$$\sigma_P = \Sigma_{j=0}^k \left[\alpha_j (\ln P)^j \right] \qquad (27)$$

Temperature Sensitivity of Pressure at a Constant Motor Geometry

The temperature sensitivity of pressure at a constant motor geometry is defined as

$$\pi_K = \left(\frac{\partial \ln P}{\partial T}\right)_K \qquad (28)$$

Adopting a formula that Glick and Brooks use to calculate the temperature sensitivity of pressure gives

$$\pi_K = \frac{1}{1-n}\left(\sigma_P + \pi_c\right) \qquad (29)$$

where the burn rate pressure exponent is defined as

$$n = \left(\frac{\partial \ln r}{\partial \ln P}\right)_T \qquad (30)$$

This leads to the following expression for the temperature sensitivity of pressure at a constant motor geometry in terms of the nonlinear equation.

$$\pi_K = \sum_{j=1}^{k}\left\{ja_j[\ln(P)]^{j-1}\right\} \qquad (31)$$

Summary of Relevant Equations

The nonlinear solid propellant burning rate equation and the temperature sensitivity equations have been developed using a multiple polynomial regression. The equations are

- Burn Rate, a combination of Equations 7 and 8

$$\ln(r) = \sum_{j=1}^{k}\left\{\left[a_{j,s} + \alpha_j(T - T_s)\right]\left[\ln(P)^{j-1}\right]\right\} \qquad (32)$$

- Temperature Sensitivity of Burn Rate at Constant Pressure

$$\sigma_P = \sum_{j=1}^{k}\left[\alpha_j \ln(P)^{j-1}\right] \qquad (27)$$

- Temperature Sensitivity of Pressure for a Constant Motor Geometry

$$\pi_K = \sum_{j=1}^{k}\left\{ja_j[\ln(P)]^{j-1}\right\} \qquad (31)$$

It is apparent that these equations can be solved with sufficient burning rate data at various pressures and initial temperatures. All of these parameters are easily obtained from such tests.

APPROACH

Effect to be Investigated

The Beckstead Derr Price (BDP) multiple flame model was used to predict the burn rate of a solid rocket propellant. The data consisted of points at nine pressures and three temperatures. The data points were determined for four different propellant particle sizes.

The burn rate data will have an uncertainty factor added to it to find out how well the nonlinear equation deals with more realistic data. The number of pressure intervals will be changed from nine to five to see if fewer data points work as well as the nine when modeling the BDP data. Expressions for σ_P and π_K based on the nonlinear equation will be developed. These tests will help determine if a nonlinear burn rate equation is more accurate and just as practical to use as the other equations being used now.

Beckstead Derr Price Multiple Flame Model "Data"

The BDP model was used to predict the burning characteristics of a composite solid propellant. A composite propellant mixes an oxidizer and a fuel binder. The BDP model assumes the combustion of the oxidizer crystal from the composite propellant is made up of three flames: the primary flame, the premixed oxidizer flame and the final diffusion flame. The burn rate is determined by solving the heat balances at the propellant surface.

The propellant from the BDP example was an AP/HTPB propellant. The oxidizer weight percent was 84.4% and the oxidizer density was 1.95 g/cm³. The binder density was 0.90 g/cm³ giving the propellant an overall density of 1.65 g/cm³. The adiabatic flame temperature was 2968 K and the molecular weight equaled 20.78 g/gmole.

The data collected was for a series of chamber pressures ranging from 0.100 MPa to 40.0 MPa. The temperatures modeled were 276 K, 293 K and 310 K. Data was also collected based on the size of the oxidizer particle. This varied from 1.0 micron to 1000.0 microns. Table 2 defines the data for the example case.

Equation Analysis

The uncertainty around the mean, sum of the squares of the residuals, the standard error of the

estimate and the coefficient of determination were calculated for the various equations under different conditions. These terms are explained in the following sections.

Uncertainty around the Mean

The uncertainty around the mean is a calculation based on the test or BDP data. The mean of the data is simply the sum of the burn rates divided by the number of burn rate values. The uncertainty around the mean is the square of the difference between a specific burn rate value and the mean burn rate value. The important value when analyzing the nonlinear burn rate equation is the total sum of the squares around the mean. In equation form it is

$$S_t = \Sigma_{i=1}^{N} \left(y_i - \bar{y}\right)^2 \tag{32}$$

Table 2 BDP Burn Rate Data for a Mean Diameter of 1000.0 Microns

310 K		293 K		276 K	
Pressure (MPa)	Burn Rate (in/sec)	Pressure (MPa)	Burn Rate (in/sec)	Pressure (MPa)	Burn Rate (in/sec)
0.1	0.023	0.1	0.022	0.1	0.022
0.211	0.029	0.211	0.029	0.211	0.028
0.447	0.036	0.447	0.036	0.447	0.035
0.946	0.053	0.946	0.052	0.946	0.051
2	0.089	2	0.087	2	0.085
4.23	0.149	4.23	0.146	4.23	0.143
8.944	0.242	8.944	0.237	8.944	0.232
18.915	0.376	18.915	0.368	18.915	0.361
40	0.588	40	0.575	40	0.563

Sum of the Squares of the Residuals

To get the "best" values of the equation coefficients, the sum of the squares of the residuals was set up in Equation 14. After the coefficients are determined, they are substituted back into Equation 14. The lower the sum of the squares of the residuals is, the better the answer.

Standard Error of the Estimate

The standard error of the estimate is calculated by taking the square root of the sum of the squares of the residuals divided by the difference between the number of data points and the number of coefficients to be

solved for. The standard error of the estimate in equation form is

$$S_{y/x} = \sqrt{\frac{S_r}{N-(m+1)}} \tag{33}$$

The subscript y/x denotes an error predicted for a y value that corresponds to a specific x value. The standard error of the estimate determines the quantity of the spread of the data around the regression line. This differs from the standard deviation which quantifies the spread of the data around the mean. Once again it is seen that the higher the order of the equation, the better the results are.

Coefficient of Determination

The coefficient of determination is a way to show the improvement of one form of the burn rate equation over. This is accomplished by comparing the sum of the squares of the residual of the various equations to the total sum of the squares around the mean. The equation for the coefficient of determination is

$$D^2 = \sqrt{\frac{S_t - S_r}{S_t}} \tag{34}$$

RESULTS

St. Robert's Law, the Komai-Frederick equation and the nonlinear equation at 1st, 2nd and 3rd orders were compared. Areas of interest were (1) equation type effects, (2) burn rate uncertainty effects and (3) pressure interval effects. Since the Komai-Frederick equation and the 1st order nonlinear equation were shown to be mathematically equal, only the 1st order equation will be presented in the results.

Equation Type Effects

In a previous section, the derivation of the nonlinear equation for use with the multiple polynomial regression method was presented. In a similar way, St. Robert's Law and the Komai-Frederick equation can be adapted for use.

Recall that for the form of the equations being used, only chamber pressure, initial temperature and burn rate are required. The standard temperature may

be any temperature. For this study. the standard temperature was one of the temperatures from the BDP data. Specifically, the standard temperature was 273 K.

Consider the BDP data for an average diameter of 1000 microns. This data was shown back in Table 2. The data used in the evaluation process was made up of all nine pressures and two different temperatures. The temperatures were 276 K and 310 K. The data was evaluated by St. Robert's Law. the Komai-Frederick equation and the nonlinear equation up to the 3rd order.

The uncertainty around the mean was defined earlier. It's value, which is based on the BDP data. determines the spread of the data around the mean and is used to measure improvement in modeling the data. The sum of the squares of the residuals was defined in a previous section. Recall that the lower the value. the better the fit. The standard error of the estimate. as defined earlier. is used to determine the quantity of the spread of the data around the regression line. The coefficient of determination is a measure of the improvement in modeling based on the mean of the data. Comparing the different values of this number for the different equation types will show whether one equation is better than another at modeling the data. All of these values are summarized in Table 3 for the nine pressures and two temperatures used in this study.

Table 3 Summary of the Equation Analysis for the Nine Pressures and Two Temperatures

Equation Type	Uncertainty Around the Mean	Sum of the Squares of the Residuals	Standard Error of the Estimate	Coefficient of Determination
St. Robert's Law	0.5792	0.2833	0.1374	0.5108
1st Order	0.5792	0.2869	0.1432	0.5047
2nd Order	0.5792	0.0957	0.0893	0.8348
3rd Order	0.5792	0.0153	0.0391	0.9736

This shows that the traditional St. Robert's Law accounts for 51% of the error associated with the uncertainty around the mean while the 3rd order nonlinear equation accounts for 97%. Based on this, the 3rd order nonlinear equation is a better model of the

solid rocket propellant burn rate. The coefficients acquired during the evaluation can be used with the data for a temperature of 293 K.

Uncertainty and the BDP Data

What happens when random noise is added to the BDP data? It is expected that results similar to those of the previous section would be obtained. To check the equations against data with more fluctuation in the curve. a ten percent noise factor was added to the BDP data. The noise factor could cause a burn rate value to increase or decrease. The object was to make it more difficult to fit the curves. The equation analysis summary table for the noise factor is Table 4.

It can be seen that the 3rd order nonlinear equation still provided the best explanation of the uncertainty around the mean error. Note. however. that only the 2nd order equation had a coefficient of determination that was relatively unchanged from the regular BDP data set calculations. Recall that in the regular BDP data set. St. Robert's Law provided a better fit than the 1st order nonlinear equation. It is observed, however. that the 1st order equation provided a better fit for the data set with the ten percent noise factor.

Table 4 Summary of the Equation Analysis for the Ten Percent Noise Factor at Nine Pressures and Two Temperatures

Equation Type	Uncertainty Around the Mean	Sum of the Squares of the Residuals	Standard Error of the Estimate	Coefficient of Determination
St. Robert's Law	0.6276	0.3666	0.1563	0.4159
1st Order	0.6276	0.3617	0.1607	0.4237
2nd Order	0.6276	0.1041	0.0932	0.8341
3rd Order	0.6276	0.0796	0.0892	0.8732

Pressure Interval Studies

It is seen that the nonlinear equation provides a good fit for the BDP data with nine pressures and two temperatures. What happens if fewer pressures are used to model the burn rate curves? The next check of the nonlinear equation involves five pressures and two temperatures. The same pressure range is used as was

9

used before. only this time the second. fourth. sixth and eighth pressure measurements are removed.

The reference for the set with five pressures and two temperatures is the case with nine pressures and two temperatures. The purpose is to find out if the results from the five pressure case are similar to the results from the nine pressure case. thereby reducing the amount of strand burner data necessary for evaluation. The uncertainty around the mean is based on the mean burn rate value from the nine pressure case. The constants from the nine pressure case were used with the predicted burn rate values from the five pressure case to determine the sum of the squares of the residuals. The standard error of the estimate and the coefficient of determination values are based on the previous two statements.

Table 5 Summary of the Equation Analysis for Five Pressures and Two Temperatures

Equation Type	Uncertainty Around the Mean	Sum of the Squares of the Residuals	Standard Error of the Estimate	Coefficient of Determination
St. Robert's Law	0.5857	0.2914	0.204	0.5025
1st Order	0.5857	0.2957	0.222	0.4952
2nd Order	0.5857	0.0988	0.1572	0.8313
3rd Order	0.5857	0.0202	0.1005	0.9655

CONCLUSIONS

The primary objective of this work was to test and verify a nonlinear solid propellant burn rate equation to be used in the performance prediction of a boost motor of a DRE. The research began with a review of temperature sensitivity theory. Then the nonlinear expression was identified. This expression was analyzed using a new least-squares multiple polynomial regression method. The conclusions are stated below.

It was observed that

- using a nonlinear equation improves the correlation to the model data up to the third order in all cases.
- using higher order equations are more effective than running more tests to improve the correlation coefficient. and

- uncertainty lowers the correlation coefficients.

REFERENCES

1 Brooks. W. T. and Glick, R. L. "Computational Aspects of Temperature Sensitivity." *22nd JANNAF Combustion Meeting*, CPIA Publication 432, Vol. II, Oct. 1985.

2 Brooks. W. T. and Miller. R. R. "Relationships Among Solid Propellant Temperature Sensitivity Parameters." *18th JANNAF Combustion Meeting*, CPIA Publication 347, Oct. 1981.

3 Chapra and Canale. Numerical Methods for Engineers, 2nd Ed., McGraw-Hill, Inc., New York, 1990.

4 Cohen. N. S. and Flanigan, D. A. "A Literature Review of Solid Propellant Burn Rate Temperature Sensitivity," Report AFRPL-TR-83-42, Morton Thiokol, Inc., Huntsville Division, Huntsville, AL, June 1983.

5 Gaunce, M. T. and Osborn. J. R. "Temperature Sensitivity Coefficients," *35th Congress of the International Astronautical Federation*, IAF-84-302, 1984.

6 Gaunce. M. T. and Osborn. J. R. "Temperature Sensitivity Coefficients of Solid Propellant Burning Rate." *Acta Astronautica*, Vol. 13, No. 3, pp. 127-130. 1986.

7 Geckler, R. and Sprenger, D. F. "The Correlation of Interior Ballistic Data for Solid Propellants." *Jet Propulsion*, pp. 22-26, Jan.-Feb. 1954.

8 Glick, R. L. and Brooks, W. T. "Comment on 'Hamke. R. E. and Osborn. J. R., "Relationships for Motor Temperature Sensitivity," *Journal of*

Propulsion and Power, Vol. 8, No. 3, May-June 1992, pp. 723-725.'", Aug. 1992.

9　Glick, R. L. and Brooks, W. T. "On the Determination of Ballistic Properties with Ballistic Test Motors." *20th Joint Propulsion Conference,* AIAA 84-1472, 1984.

10　Glick, R. L. and Brooks, W. T. "Pressure Exponent and Temperature Sensitivity: Comment on Two Previous Articles." *Acta Astronautica,* Vol. 21, No. 10, pp. 733-734, 1990.

11　Glick, R. L. and Brooks, W. T. "Relations Among Ballistic Properties of Solid Propellants." *Journal of Propulsion and Power,* Vol. 1, No. 4, pp. 319-320, July-Aug. 1985.

12　Hamke, R. E.; Gaunce, M. T. and Osborn, J. R. "The Effect of Pressure Exponent on Temperature Sensitivity." *37th Congress of the International Astronautical Federation,* IAF-86-195, 1986.

13　Hamke, R. E.; Gaunce, M. T. and Osborn, J. R. "The Effect of Pressure Exponent on Temperature Sensitivity." *Acta Astronautica,* Vol. 15, No. 6/7, pp. 377-382, 1987.

14　Hamke, R. E. and Osborn, J. R. "Relationships for Motor Temperature Sensitivity." *Journal of Propulsion and Power,* Vol. 8, No. 3, pp. 723-725, May-June 1992.

15　Hill, P. and Peterson, C. Mechanics and Thermodynamics of Propulsion, 2nd Ed., Addison-Wesley Publishing Co., Reading, MA, 1992.

16　Komai, I. "An Analytical Assessment for the Temperature Sensitivity in Ducted Rocket Gas Generators." Thesis, The Department of Mechanical and Aerospace Engineering, The University of Alabama in Huntsville, 1993.

17　Kubota, N. "Survey of Rocket Propellants and Their Combustion Characteristics." Fundamentals of Solid Propellant Combustion, Kuo, K. K. and Summerfield, M. (Eds.), *Progress in Astronautics and Aeronautics,* Vol. 90, pp. 1-52, AIAA, New York, 1984.

18　Kubota, N. "Temperature Sensitivity of Solid Propellants and Affecting Factors: Experimental Results." Nonsteady Burning and Combustion Stability of Solid Propellants, De Luca, L.; Price, E. W. and Summerfield, M. (Eds.), *Progress in Astronautics and Aeronautics,* Vol. 143, pp. 111-143, AIAA, New York, 1992.

19　Matson, J. C. Course notes from A&AE 539, Purdue University, Lafayette, IN, 1983.

20　Sutton, G. P. Rocket Propulsion Elements, 6th Ed., John Wiley & Sons, Inc., New York, 1992.

AIAA-95-2993
IGNITION AND COMBUSTION
OF CARBON PARTICLES

J. V. DEMPSEY, JR. AND D. A. FEIKEMA
THE UNIVERSITY OF ALABAMA IN HUNTSVILLE
DEPARTMENT OF MECHANICAL AND
AEROSPACE ENGINEERING
PROPULSION RESEARCH CENTER
HUNTSVILLE, ALABAMA 35899

D. L. MAY
PROPULSION DIRECTORATE
U.S. ARMY MISSILE COMMAND
REDSTONE ARSENAL, ALABAMA 35898

31st AIAA/ASME/SAE/ASEE
Joint Propulsion Conference and Exhibit
July 10-12, 1995/San Diego, CA

Ignition and Combustion
of Carbon Particles

John V. Dempsey, Jr.* and Douglas A. Feikema[†]
University of Alabama in Huntsville
Department of Mechanical and Aerospace Engineering
Propulsion Research Center
Huntsville, AL 35899

Doug L. May
Propulsion Directorate
U.S. Army Missile Command
Redstone Arsenal, AL 35898

Abstract

Fullerenes (C_{60}/C_{70} molecules) have produced wide interest in many fields because of the many suggested potential applications including high energy fuels, polymers and biomaterials. The current research seeks to expand upon the fundamental knowledge base concerning the ignition and combustion of fullerene particles injected into high temperature combustion gases within an oxygen rich environment. The thermal and chemical environment of the combustion gases are produced by a laminar, premixed methane/air flame stabilized on a porous flat flame burner apparatus. An optical measurement system is used to non-intrusively measure 1) ignition characteristics and 2) the total burnout time under varying oxygen concentrations and flame temperatures.

Introduction

Air breathing rocket technologies having high energy density can provide longer range with lower propellant volume. These capabilities have maintained a continued interest in long range, volume limited propulsion systems.[1] Advances in missile propulsion system technology have provided large increases in missile performance. In the ducted rocket engine (DRE) concept (Figure 1), the oxidizer is air while the fuel is pre-combusted gas produced by a fuel-rich, end burning, Glycidyl Azide Polymer (GAP) solid fuel-gas generator (SFGG). The requirements for improved fuels are guided by three primary goals: 1) increased performance (i.e. longer range, higher velocity, and thrust control); 2) joint service requirements for insensitive munitions; and 3) minimum signature requirements.

* Graduate Research Assistant, Student Member AIAA
† Assistant Professor, Senior Member AIAA

The evaluation and selection of a high energy fuel additive is an important characteristic when investigating combustion efficiency. In practice, this requires that the ignition and combustion times of solid particulate fuel additives match residence times within the combustor. For example, the ignition of carbon is substantially simpler to achieve as opposed to boron which makes carbon an attractive high energy additive.[2,3] This practical difficulty observed with the higher energy density materials (i.e. boron) has lead to the development of thin magnesium[2] and GAP coatings[4] which alter the ignition kinetics and reduces combustion times.

Fullerenes (C_{60}/C_{70} molecules) have produced wide interest because of the many suggested potential applications including super-conductors, lubricants, catalysts, high energy fuels, polymers and biomaterials. Fullerenes were first detected in carbon vapor produced by laser evaporation of graphite in 1985.[5] The spherical nature of the structure, which has no edge atoms vulnerable to reaction, was proposed to explain the observed high stability of certain Carbon clusters relative to that of others at high temperature and in the

presence of an oxidizing gas. The proposed structure remained unconfirmed until 1990[6], when samples large enough for spectroscopy were produced by vaporization of graphite rods with resistive heating under an inert atmosphere. This production method was quickly adopted by several research groups and small companies. The interest rapidly expanded to include fullerene based entities, i.e. fullerenes with metals, hydrogen, oxygen, methyl, phenyl, or other functional groups or cross-links. Physical properties of the novel fullerenes are currently under investigation by various researchers.[5,6]

With this information, propulsion system developers have begun development of DRE technologies which can be deployed as next-generation propulsion systems. Fullerenes may be the best solid fuel additive for air-breathing propulsion systems that require minimum signature. As a pure fuel, carbon has a favorable density range of 1.6 to 1.9 gm/cm^3 and has excellent gravimetric and volumetric heating values of 7.8 kcal/gm and 14 $kcal/cm^3$, respectively. The C_{60} molecule has a density of 1.67 gm/cm^3 and bond energy of 7 eV/atom whereas graphite and diamond are both less than this value. While the heat of formation for carbon black is zero and for diamond it is insignificant, the heat of formation for C_{60} is +757 cal/gm. The complete combustion by-product of a carbon/oxygen fuel/oxidizer system is carbon dioxide-- the epitome of minimum signature with no solids or water vapor to form a condensation trail. Thus, one of the major goals of the carbon/ducted air system is to achieve high combustion efficiency.

Carbon black agglomerates and fullerene particles are investigated as high energy fuel additives for a DRE concept. A SFGG decomposes to supply heated fuel-rich gases and carbon particles to the rocket combustor. Within this combustor the solid carbon particles through their exothermic heat release provide additional thrust to the rocket. The salient parameters which have been identified in the literature to have significant effects on combustion rates are the following: *1) particle size, 2) ambient temperature, 3) oxidant concentration, 4) homogenous versus heterogeneous ignition and combustion, 5) agglomeration, 6) particle surface morphology and porosity, 7) convective environments, 8) chemical kinetic mechanisms, 9) particle surface temperature, and 10) diffusion processes.* Issues one through six are planned for evaluation in the current facility at the

Propulsion Research Center at the University of Alabama in Huntsville.

Experimental Methods

A flat flame burner apparatus has been assembled to approximate the thermal and chemical environment of the conditions of DRE combustor. The flat flame burner method has been selected because the flame is laminar, steady, easily controlled, and approaches chemical equilibrium conditions which can be computed using a chemical equilibrium code.[2,3,7] In the actual propulsion system, a GAP based gas generator provides heated fuel-rich gases[8] and carbon particles. The process is simulated by injecting carbon particles or agglomerates into the premixed laminar flame. Qualitative ignition and combustion results for both carbon black and fullerene (C_{60}/C_{70} molecules) agglomerates are reported. The thermal and chemical environment of the flame can be altered by varying the fuel/air ratio to investigate conditions under which ignition and complete combustion of the particulates can be optimized. An optical imaging system is used to record the flame radiation of the burning particles. Ignition and combustion times are determined from the streak trails recorded by the imaging system. Prior to testing, some candidate carbon particles were previously examined for their size, surface morphology and agglomerate behavior using an Atomic Force Microscope (AFM).[9]

Flat Flame Burner Apparatus

A schematic of the laminar flat flame burner and associated equipment is shown in Figure 2. The flat flame burner is manufactured by McKenna Products, Incorporated, and consists of a 6 cm diameter sintered porous plate, a 1.4 cm wide sintered porous shroud ring, and a 3 mm diameter particle inlet tube in the center. The flat flame burner is used to generate laminar premixed flames with near uniform temperature and uniform species concentrations in the flame region. The flame temperature is known to decrease slightly with height above the burner.[3] The nitrogen shroud flow is used to prevent the diffusion of additional oxidizers from the ambient air into the center of the flame and to prevent flame destabilization. The flow rates and pressures of all gas flows are monitored by rotometers and pressure gauges to regulate known reactant fuel/air ratios and to ensure steady state behavior. Water from standard city water lines cools

the burner. The flat flame burner apparatus is similar to that used by several researchers.[2,3,4,7]

The carbon agglomerates are injected individually into the premixed flame through the centered tube. A fluidized bed is loaded with either carbon black agglomerates (ranging in size from 45 µm to 63 µm) or fullerene particles (mean size of 35 µm) and 100 micron silica spheres. The experimentation is performed with a weight loading ratio of 50:1 of silica to carbon. The fluidized bed consists of a vertical glass tube of 1.5 inches in diameter and 18 inches in length. A low nitrogen gas flow is passed through the bed to adequately levitate the carbon particles; however, the nitrogen flow rate is insufficient to disturb the silica bed particles. An additional nitrogen flow is provided to enable control of the exit carrier gas velocities of the particles as they enter the flame. The convective properties of the ignition attributes and particle burning can thereby be investigated with this design. The fluidized bed is supported between two end flanges and an outer thick-walled plastic tube to ensure safety and rigidity. The nitrogen gas enters the fluidized bed through a glass porous plug in order to ensure cross-sectional uniformity. The silica and carbon particle mixture occupy approximately 1.5 inches at the bottom of the fluidized bed. At the base of the flat flame burner, a hypodermic needle of 275 microns inner diameter has been positioned inside of a tee to further reduce particle supply rates to the flame.

Optical Measurement System

An optical system, shown by Figure 3, is used to accurately measure ignition and combustion times of the particles. The technique is based upon the detection of flame radiation emitted by the burning carbon particles primarily in the visible wavelength. A Princeton Instruments Image Intensified CCD (ICCD) camera and image processing system equipped with a NIKON f/1.4 105 mm Micro lens is used to visualize and record the burning particle streaks inside the laminar flame. Particles are injected into the central tube and detected upon ignition. With the association of the 1:1 ratio image replication lens, the ICCD camera clearly captures the 20.0 mm by 13.2 mm region. Larger fields of interest may be captured by reducing the macro capabilities of the lens. The current image intensifier and array can be gated to a minimum exposure time of 5 milliseconds. With upgrades, the intensifier system can be gated to 6 nanoseconds. The

system records ignition and combustion distances based upon the exposure time of the intensifier.

Test Conditions

The flame conditions simulate the mixing region in the combustor where the air and SFGG products mix. The SFGG effluent has been estimated using a chemical equilibrium calculation and are summarized in Table 1. The computed adiabatic flame temperature is 1465 K. It is noted that the actual composition could differ from that computed using chemical equilibrium assumptions since chemical equilibrium is rarely observed in actual systems. Upon mixing with air, the solid and gaseous combustibles react and produce heat. For the present study the conditions of Table 1 are not to be reproduced but are to be addressed in subsequent research. A wet gas flame, similar to practical conditions, could be produced with premixed propane, oxygen, and nitrogen flames.[4]

Major Specie	Mole Fraction
N_2	22.30
$C(s)$	28.47
CO	14.95
CO_2	0.13
CH_4	2.15
H_2	32.10
H_2O	0.71

Table 1 Computed Equilibrium Fuel Rich Solid Propellant Combustion Products

Future efforts will focus on examining complete flame conditions which represent the regions where SFGG products and air mix.

For the present research, methane/air flames have been used to evaluate the ignition and combustion of the carbon black and fullerenes. The flow rates of methane, air, shroud nitrogen, and fluidized bed carrier nitrogen gas flows for the flames reported are summarized in Table 2. The flame conditions, as shown by Table 3, have been estimated using chemical equilibrium computations. Actual flame conditions are expected to be different since chemical equilibrium is probably not completely achieved; however, chemical equilibrium is a good first estimate of the representative species concentrations. It is assumed that heat losses

cause the observed flame temperatures, in small scale frame hardware, to be about 200 K less than computed adiabatic flame temperatures. The chemical equilibrium conditions in the flame have been computed using a modified PC version of the NASA Gordon McBride Chemical equilibrium code known as ODETRAN.

Carbon Particle Samples

The high density fuel additives presently being considered for SFGG are carbon black and fullerenes or buckyballs. The carbon black samples have been provided by R. T. Vanderbilt Chemical Company (Product N991) with a reported individual mean size of approximately 270 nm. This was verified using Atomic Force Microscopy (AFM).[9] The individual particles are near spherical, non-porous, and approximately 300 nm, diameter, in agreement with the product data sheet. A fractal surface dimension of the surface represented was taken and was found to be 2.3. A surface fractal dimension of 2.0 corresponds to a flat plane and a surface fractal dimension of 3.0 corresponds to a completely rough surface. Based upon these dimensions the carbon blacks appear to be smooth. Highly magnified images of a single particle verified that the particles are smooth and non-porous. Agglomerates of these particles were vibration sieve-separated into the size range of 45 to 63 μm, loaded into the fluidized bed and injected into the flame.

The Fullerene sample presently considered is a 85:15 mixture of C_{60} and C_{70} molecules, respectively. The fullerenes have been manufactured and provided by the U.S. Army Missile Command (MICOM). These C_{60}/C_{70} particles have been manufactured by the application of a high intensity voltage and current across a graphite rod in helium. AFM[9] indicated that the C_{60}/C_{70} particles appear to be rougher on the surface and to have a higher degree of scatter in their particle size. The actual size of the particles is inconclusive from the AFM images; however, the manufacturer reports a mean size of 35 μm. High magnification of the surfaces indicated the materials were non-porous.

Results and Discussion

Ignition and combustion times for the fullerene particles are more rapid than the carbon black samples considered. The ignition and combustion of the carbon black and fullerene samples were approximately 2.5

millisecond, and 1 millisecond, respectively. The fullerene combustion process does not resemble classical combustion of solid spheres such as carbon black. The carbon black combustion, as shown by Figure 4, exhibits burning characteristics independent to flame temperature over the given test conditions. The combustion of the fullerene particle exhibits rapid deflagration as shown by Figure 6. The effect of oxidant concentration, i.e.: fuel equivalence ratio, cannot be determined from the present results since both the flame temperature and oxidant, O_2, concentration are not measured independently. Although the oxidant concentration in leaner flames is higher, the lower flame temperature delays the ignition time. Figures 5 and 7 display carbon black and fullerene ignition times, respectively. The combustion time for the carbon black is rather constant over the range of flame conditions;. on the other hand, the fullerene particles combust in an rapid, undirected fashion. The fullerene approximated combustion times for the conditions considered are shown by figure 8.

Summary

This paper describes the ongoing research into the ignition and combustion of particulate carbon, focusing on high combustion efficiency. A test apparatus, including a flat flame burner and optical measurement system, has been constructed to characterize the ignition and combustion of carbon black and fullerenes. This research provides optical data of the reacting particulate carbon forms in an oxidizer rich environment.

Future experiments will focus on laminar, propane/oxygen flames, smaller carbon black agglomerations, and extensive fullerene particle investigations.

Acknowledgment

References

1. King, M. K., " Ignition and Combustion of Boron Particles and Clouds", AIAA-82-4174, *Journal of Spacecraft*, Vol. 19, No. 4, pp. 294-305, 1982.

2. Yeh, C. L., Hsieh, W.H., Kuo, K. K., and Felder, W., " Ignition and Combustion of Mg-Coated and Uncoated Boron Particles", Edited Proceedings of the Third International Symposium on Special Topics in Chemical Propulsion: Non-Intrusive Combustion Diagnostics, Scheveningen, Netherlands, May 10-14, 1993.

3. Hsieh, W., H. and Yeh, C. L, "Measurement of Burning Surface Temperature of Boron", *AIAA-92-3629*, July 6-8, 1992.

4. Shyu, I.-M. and Liu, T.-K., "Combustion Characteristics of GAP-Coated Boron Particles and the Fuel-Rich Solid Propellant", *Combustion and Flame*, 100: pp. 634 - 644, 1985.

5. Kroto, H. W., Heath, J. R., O'Brien, S. C., Curl, R. F., and Smalley, *Nature*, 318, 162, 1985.

6. Kroto, H. W., Fischer, H. W., and Cox, D. E, *The Fullerenes*, Pergamon Press, 1993.

7. Macek, A. and Semple, M., "Combustion of Boron Particles at Atmospheric Pressure", *Combustion Science and Technology*, Vol. 1, pp. 181-191, 1969.

8. Frankel, M. B., Grant, L. R., and Flanagan, J. E., "Historical Development of Glycidyl Azide Polymer", *Journal of Propulsion and Power*, Vol. 8, No. 3, May-June, 1992.

9. Feikema, D. A., "An Initial Study on the Ignition and Combustion of Carbon Particles", *AIAA-94-3270*, June, 1994.
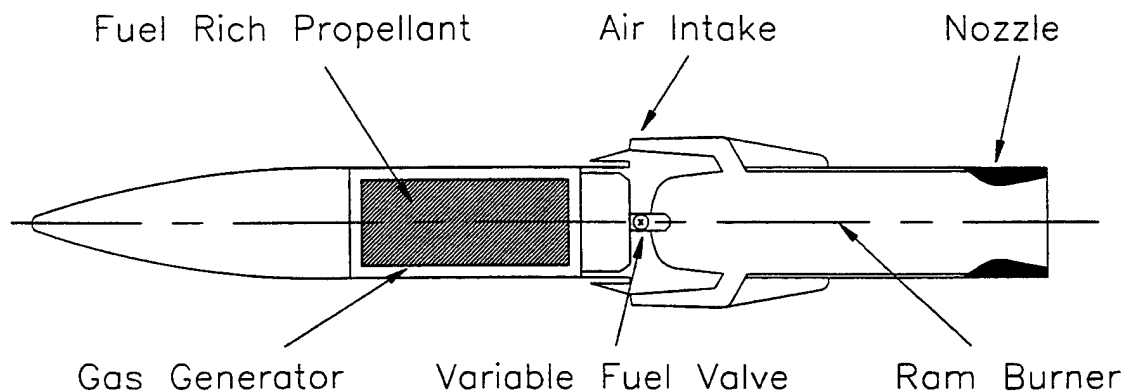
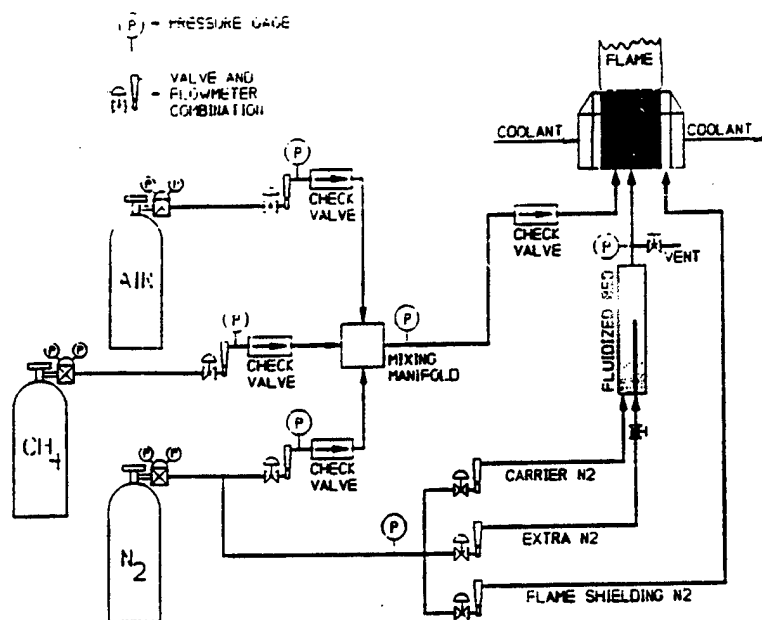Figure 1. Schematic of the Ducted Rocket Engine.

Figure 2. Schematic of Flat Flame Burner Apparatus.
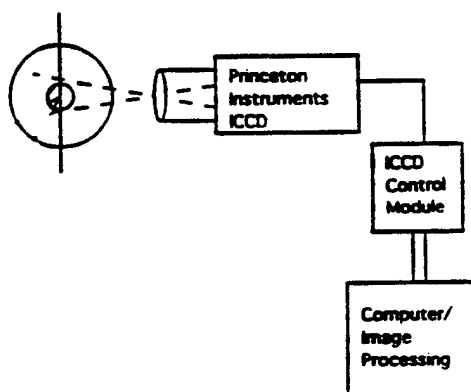
Figure 3. Schematic of Optical Measurement System
for Ignition and Combustion Times.

Fuel Equivalence Ratio	Adiabatic Flame Temperature (°K)	Methane Flow Rate (Standard cm³/sec)	Air Flow Rate (Standard cm³/sec)	Guard Nitrogen Flow Rate (Standard cm³/sec)	Nitrogen Fluidized Bed Flow Rate (Standard cm³/sec)
074	1896	21.6	308.3	98.3	98.3
0.85	2074	25.1	308.3	98.3	98.3
0.97	2203	28.4	308.3	98.3	98.3
1.07	2226	31.5	308.3	98.3	98.3

Table 2. Summary of the Gas Flow Rates for each Premixed Flame.
Standard Flow Rate refers to Atmospheric Pressure and Temperature.

Equiv. Ratio	T exit Eqbm	Moles CO_2	Moles H_2O	Moles N_2	Moles O_2	Moles CO	Moles NO	Moles OH	Moles O	Moles H	Moles H_2
0.74	1896	0.0716	0.1424	0.7233	0.0498	0.0002	0.0028	0.0010	0.0001	0.0000	0.0001
0.85	2074	0.0811	0.1623	0.7140	0.0265	0.0012	0.0033	0.0023	0.0002	0.0001	0.0005
0.97	2203	0.0860	0.1788	0.7043	0.0084	0.0057	0.0025	0.0031	0.0003	0.0003	0.0023
1.07	2226	0.0791	0.1882	0.6907	0.0008	0.0204	0.0008	0.0019	0.0001	0.0006	0.0091

Table 3. Chemical Equilibrium Conditions for the Flames Investigated.

Figure 4. Streak photograph of carbon black in methane-air flame.
$\Phi = 0.85$ Particle velocity: 617 cm/s
Photograph is rotated 90° CW Actual trajectory is vertical upward.

American Institute of Aeronautics and Astronautics

Carbon Black Agglomerates
Size: 45-66 microns
Equivalence Ratio vs. Ignition & Combustion Times

Figure 5. Equivalence Ratio vs. Ignition and Combustion Times.
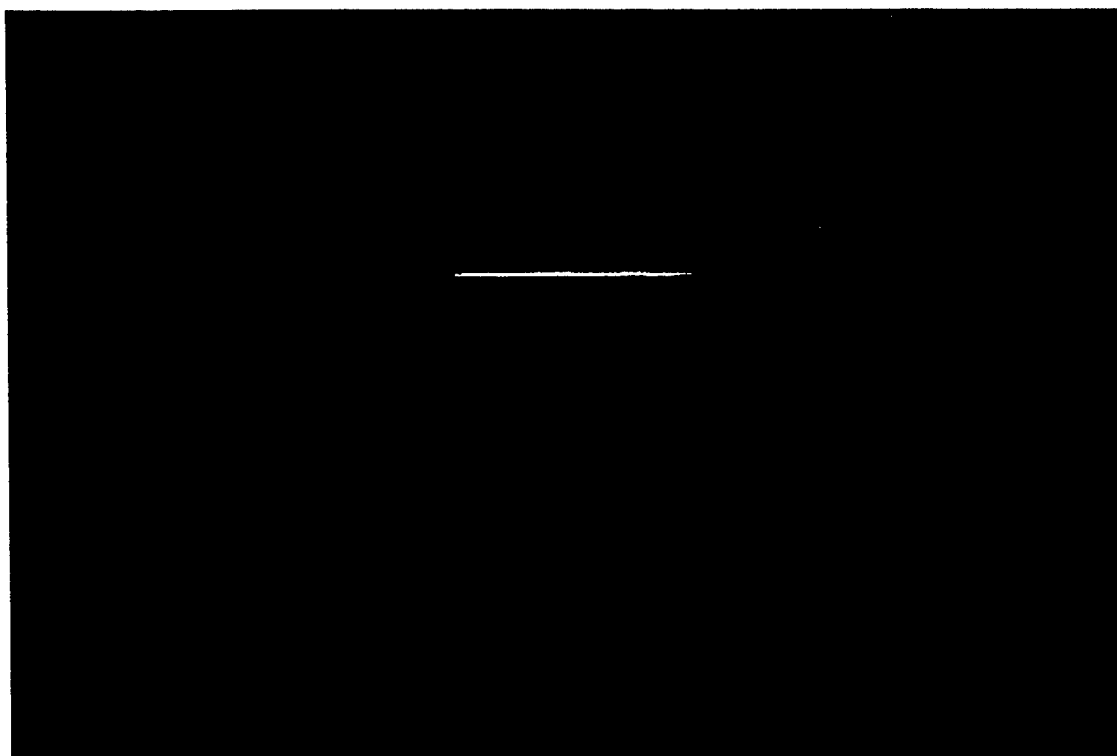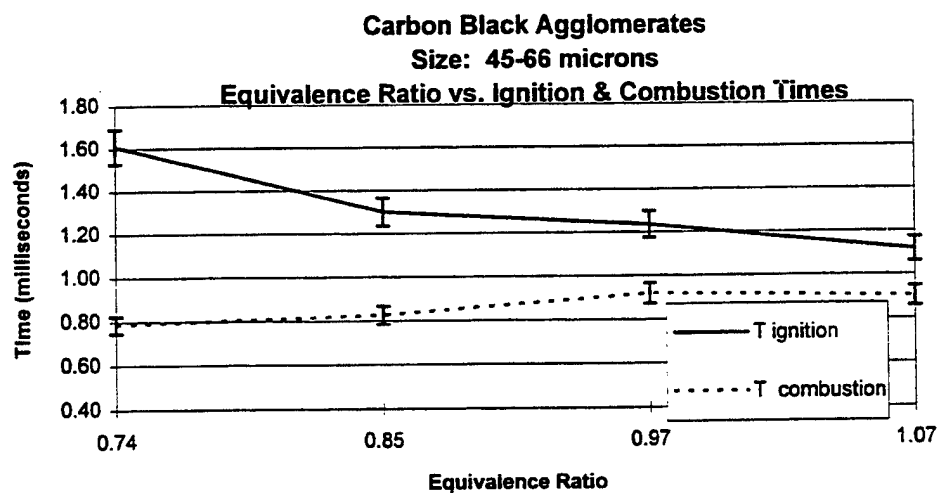Carbon Black Agglomerations Size: 45-66 microns.
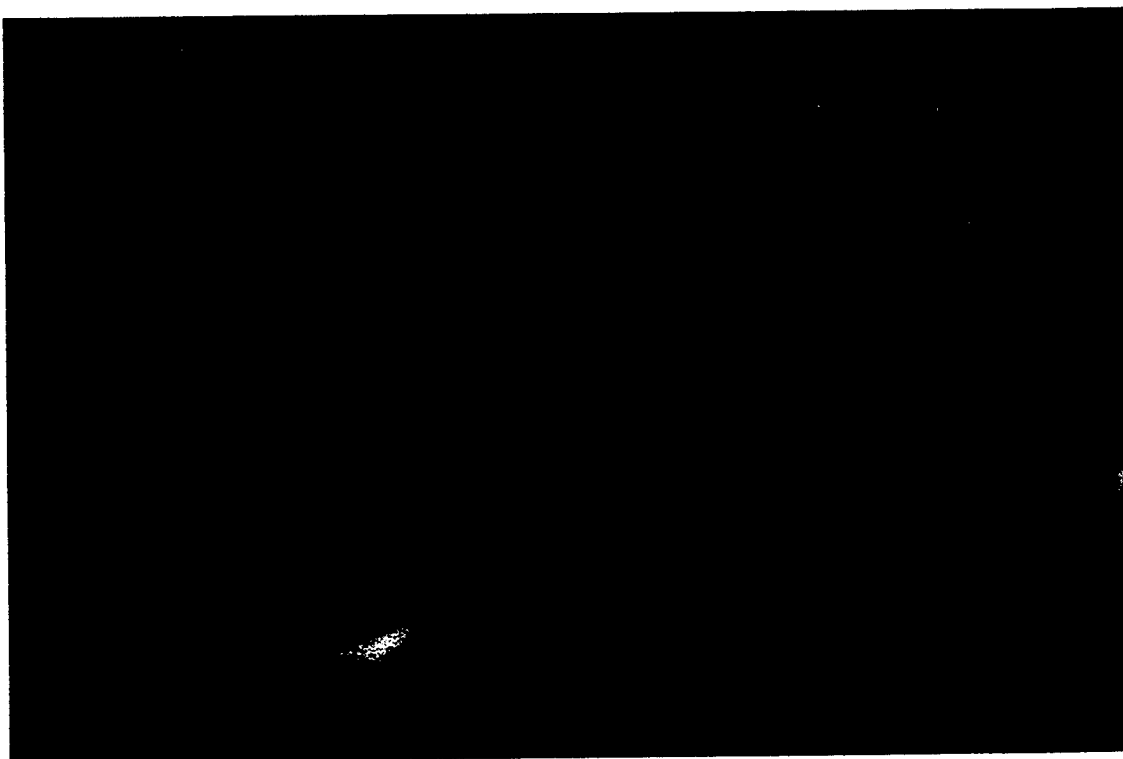
Figure 6. Streak photograph of fullerene in methane-air flame.
$\Phi = 0.85$ Particle velocity: 1342 cm/s
Photograph is rotated 90° CW. Actual trajectory is vertical upward.

American Institute of Aeronautics and Astronautics

Fullerene Particles
Nominal Size: 35 microns
Equivalence Ratio vs. Ignition Times
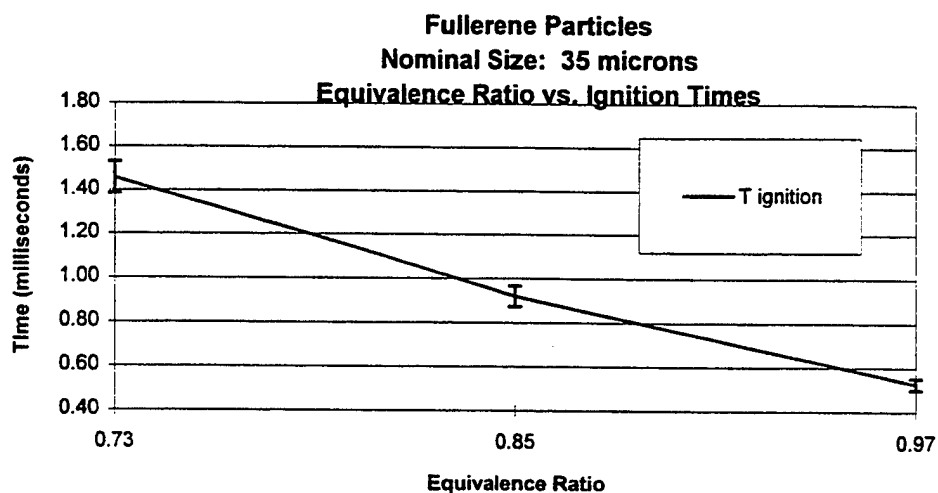
Figure 7. Equivalence Ratio vs. Ignition Times.
Fullerene Particles Nominal Size: 35 microns.
Time Scale: Milliseconds

Fullerene Particles
Nominal Size: 35 microns
Equivalence Ratio vs. Combustion Times
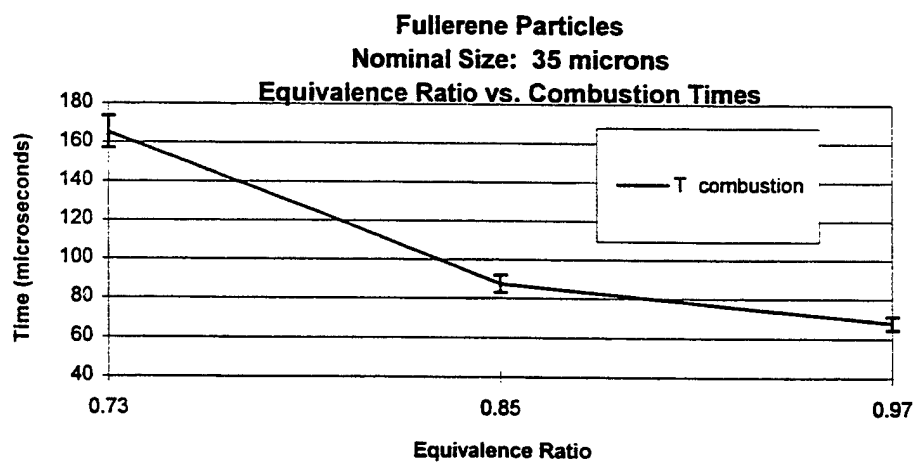
Figure 8. Equivalence Ratio vs. Combustion Times.
Fullerene Particles Nominal Size: 35 microns.
Time Scale: Microseconds

AIAA 95-3074

An Assessment of Connected-Pipe Ramjet Testing

John A. Blevins and Hugh W. Coleman
Propulsion Research Center
Department of Mechanical and Aerospace Engineering
University of Alabama in Huntsville
Huntsville, Alabama 35899

31st AIAA/ASME/SAE/ASEE
Joint Propulsion Conference and Exhibit
July 10-12, 1995/San Diego, CA

AN ASSESSMENT OF CONNECTED-PIPE RAMJET TESTING

John A. Blevins[*] and Hugh W. Coleman[†]
Propulsion Research Center
Department of Mechanical and Aerospace Engineering
University of Alabama in Huntsville, Huntsville, AL 35899

Abstract

The results of an assessment of selected data reduction methods for performance determination in connected-pipe ramjet testing from an uncertainty analysis viewpoint is presented. The study identifies and reviews 4 distinct methods of determining characteristic exhaust velocity (C*), efficiency based on C*, specific impulse (Isp) and efficiency based on Isp, and 16 distinct methods for determining thermal efficiency. The general uncertainty analysis of the performance parameters for a case study is presented for conditions of one percent uncertainties in the input variables and for reasonable estimates of the uncertainty of input variables for a liquid fuel ramjet and a ducted rocket engine. The study shows that a wide range of values and uncertainties for the performance parameters can be calculated using the different data reduction methods with identical input parameters. Also, the relative influence of the uncertainty of each input parameter on the result uncertainty is presented for all identified data reduction methods.

Introduction

Connected-pipe testing is used for performance determination and fundamental combustion studies in ramjet and scramjet engines[1,2]. A schematic of a typical connected-pipe facility is shown in Figure 1. In connected-pipe testing, the air supply is connected directly to the ramjet combustor and, therefore, connected-pipe testing considers only the combustor performance and no aerodynamic or inlet effects. By considering only the ramjet combustor, the air supply requirement and equipment necessary for testing is minimized making connected-pipe testing the most cost-effective method for evaluation and development of ramjet engines prior to free jet and flight testing[2].

---

[*]Graduate Research Assistant, Student Member AIAA

[†]Eminent Scholar in Propulsion and Professor, Senior Member AIAA

There exist various data reduction methods for each of the performance parameters associated with ramjet testing in connected-pipe facilities. An AGARD working group was tasked to review and report currently accepted methods for performance determination in connected-pipe testing. The subsequent report[3] issued by AGARD included a concise listing of data reduction methods for performance determination that are used by the international technical community. The various data reduction methods yield a range of values for each of the performance parameters (such as thermal efficiency, which ranged from 86% to 96% in the sample case presented in this paper using 16 different data reduction methods). The difference in the performance parameter values that can be determined by the use of the various data reduction methods is the impetus for the assessment of data reduction methods from an uncertainty analysis standpoint as presented in this paper.

The generic combustor shown in Figure 1 includes station designations that have been standardized[3] in order to simplify the reporting of test results. The station identification numbers are used as subscripts in this paper to denote station. Station 2 corresponds to the post compression inlet conditions. Station 3 indicates upstream combustor conditions. Station 4 is used to indicate the downstream combustor conditions. Station 5 corresponds to the nozzle throat and station 6 is used to indicate the nozzle exit plane.

For the appropriate simulation of vehicle flight conditions, the air must be supplied at the stagnation temperatures and pressures that are to be encountered during flight. In order to supply the combustor with the high temperature air necessary to simulate the conditions produced by a supersonic compression inlet, a vitiated heater is used to increase the air temperature. A vitiated heater uses combustion of a fuel added to the air flow to increase the temperature. Also, oxygen is added to the flow field to offset the consumption of oxygen by the combustion of the vitiator fuel. There are two approaches to oxygen replenishment: 1) make-up oxygen is added to

account for the mass of oxygen consumed by the combustion of the vitiator fuel, and 2) make-up oxygen is added to preserve the volumetric content of oxygen in the supply air. Both of these vitiator methods are discussed in reference [3]. By adding the fuel and makeup oxygen, the composition of the oxidizer supplied to the combustion chamber is no longer that of air because it includes combustion products from the vitiated heater. The composition can generally be considered to be all of the constituents (air, vitiator fuel, and makeup oxygen) at equilibrium at the static temperature and pressure of the inlets to the ramjet combustor.

The review and assessment of the data reduction methods presented in this paper include a description of the methods for selected performance parameters, an assessment of the propagation of uncertainty for each input parameter, and a general uncertainty analysis for each of the data reduction methods for the selected performance parameters.

Data Reduction Methodology

The various data reduction methods for selected performance parameters associated with ramjet testing in connected-pipe facilities are discussed in this section. These data reduction methods are taken from the AGARD advisory report previously mentioned.

Chemical Equilibrium Combustion Codes

The majority of methods for performance determination utilize output from chemical equilibrium combustion (CEC) codes. The codes, which were developed for classical rocket motor performance and species determination, are based on a zero velocity combustion model since the Mach number in classical rocket motors is very small. To account for velocity in the combustion chamber of a ramjet, the accepted practice is to consider stagnation flow properties as inputs to the code instead of static flow properties[3].

There are several different CEC codes in use. The two most frequently used codes are NASA CET89[4,5] and the PEP code[6]. Previous investigations have shown no significant difference in the performance values calculated using the NASA CET89 and PEP codes[3].

Performance Determination

Use of the different recommended[3] data reduction methods with identical inputs produces different values for the performance parameters. The

variation in these determined values using the same input parameters is one of the primary reasons for the undertaking of this study to assess the different methods of performance determination.

The performance parameters chosen as the subject of the uncertainty analysis assessment presented in this article are characteristic exhaust velocity (C*), efficiency based on C* (η_{C*}), vacuum specific impulse (Isp), efficiency based on Isp (η_{Isp}), and thermal efficiency ($\eta_{\Delta T}$). In this study, 4 distinct methods are identified for the determination of each of the parameters C*, η_{C*}, Isp, and η_{Isp}. The thermal efficiency ($\eta_{\Delta T}$) can be determined from 4 different equations, two using C* as input and two using Isp as input, resulting in 16 distinct data reduction methods for the determination of $\eta_{\Delta T}$.

The different C* and Isp methods are based on different methods for determining the total pressure at station 4 (p_{t4}). A diagram illustrating the relationship between p_{t4}, C*, Isp, and $\eta_{\Delta T}$ is shown in Figure 2.

The 4 methods for determining p_{t4} identified in this study are

Method 1:
$$p_{t4} = p_{t4CEC} \qquad (1)$$
where p_{t4CEC} is determined by a CEC code using the isentropic flow relations.

Method 2:

$$p_{t4} = p_4 \left(1 + \frac{\gamma - 1}{2} \cdot M_4^2\right)^{\frac{\gamma}{\gamma - 1}} \qquad (2)$$

where p_4 is the measured static pressure at station 4, M_4 is the Mach number at station 4, and γ is the isentropic exponent which relates the properties of station 4 and station 5 as an isentropic process. The value of γ is obtained through the relation[3]

$$\gamma = \frac{\ln(p_4/p_5)}{\ln(p_4/p_5) - \ln(T_4/T_5)} \qquad (3)$$

where p_5, T_4 and T_5 can be found as output from the CEC codes.

The difference in method 1 and method 2 is that in method 1 the code uses an isentropic exponent that is not the same as the process isentropic exponent, γ, used in method 2. The use of the process γ as

defined in Equation (3) is the recommendation of the AGARD working group report since it exactly relates the properties of the end states (combustor exit and nozzle throat) by an isentropic process.

The process γ defined above is not calculated directly by all codes. The value of the process γ lies within the range of values for the isentropic exponent based on frozen flow and the isentropic exponent based on equilibrium flow. For simplicity, in this paper γ always refers to the process isentropic exponent based on the flow properties at station 4 and station 5 as defined in Equation (3).

Method 3:

$$p_{t4} = \frac{F_5 + p_{amb}A_5}{(1 + \gamma CD_5)A_5} \left(\frac{\gamma + 1}{2} \right)^{\frac{\gamma}{\gamma-1}} \quad (4)$$

where p_{amb} is the ambient pressure, A_5 is the nozzle throat area (station 5), CD_5 is the nozzle discharge coefficient, and F_5 is the stream thrust as determined by

$$F_5 = F_{LC} - F_{PL} - A_b(p_b - p_{amb}) \quad (5)$$

where F_{LC} is the load cell measurement, F_{PL} is the preload on the load cell, A_b is the nozzle base area, and p_b is the base pressure.

Method 4:

$$p_{t4} = \left(\frac{C_{th}^*}{Isp_{th}} \right) \frac{F_5 + p_{amb}A_5}{CD_5 A_5} \quad (6)$$

where C_{th}^* is the maximum theoretical C^* calculated by the chemical equilibrium code and Isp_{th} is determined by the code from

$$Isp_{th} = \frac{\dot{m}_5 c_5 + p_5 A_5}{\dot{m}_5} \quad (7)$$

where $\dot{m}_5$ is the mass flow rate at the nozzle throat and c_5 is the velocity of exhaust gases at the nozzle throat. Assuming that the nozzle is choked, this corresponds to the speed of sound which is an output of the CEC codes.

The determination of C^* is based on the equation

$$C^* = \frac{p_{t4}A_5 CD_5}{\dot{m}_4} \quad (8)$$

where $\dot{m}_4$ is the total mass flow rate exiting the combustor and p_{t4} is from one of Equations (1), (2), (4), or (6), thus giving four ways to determine C^*.

The efficiency based on C^* is determined from

$$\eta_{C^*} = \frac{C^*}{C_{th}^*} \quad (9)$$

where C^* is determined from Equation (8).

The determination of Isp is based on the equation

$$Isp = \frac{p_{t4}A_5}{\dot{m}_5} \left(\frac{2}{\gamma + 1} \right)^{\frac{\gamma}{\gamma-1}} \cdot (1 + \gamma CD_5) \quad (10)$$

where $\dot{m}_5$ is the mass flow rate at the nozzle throat (assuming that the mass flow in the combustor is expanded through the nozzle, $\dot{m}_5 = \dot{m}_4$), and p_{t4} is from one of Equations (1), (2), (4), or (6), thus giving four ways to determine Isp. It should be noted that, when using Equation (10) for determining the Isp based on the total pressure, p_{t4}, determined by using Equation (4), the influence of p_{t4} is actually eliminated resulting in

$$Isp = \frac{F_5 + p_{amb}A_5}{\dot{m}_5} \quad (11)$$

The efficiency based on Isp is determined by

$$\eta_{Isp} = \frac{Isp}{Isp_{th}} \quad (12)$$

where Isp_{th} is the theoretical maximum value for Isp determined by Equation (7) and Isp is determined from Equation (10) or (11).

The determination of thermal efficiency is based on the equation

$$\eta_{\Delta T} = \frac{T_{t4,exp} - T_{t2}}{T_{t4,th} - T_{t2}} \quad (13)$$

where $T_{t4,exp}$, the total temperature at station 4, is calculated using experimental measurements and $T_{t4,th}$ is the theoretical total temperature at station 4 (adiabatic flame temperature based on stagnation flow properties) as determined by the use of a CEC code. Direct measurements to determine the cross-section average value of $T_{t4,exp}$ are generally not performed due to the difficulty in obtaining good results[3]. For this reason, the direct measurement of $T_{t4,exp}$ is not considered in this paper. $T_{t4,exp}$ can be

determined from four equations, two using C* as inputs and two using Isp as inputs. Therefore, each equation for $T_{t4,exp}$ represents four different data reduction methods for $\eta_{\Delta T}$ as shown in Figure 2. The equations for the determination of $T_{t4,exp}$ are

$$T_{t4,exp} = \gamma \left(\frac{2}{\gamma+1}\right)^{\frac{\gamma+1}{\gamma-1}} \cdot \left(\frac{C^{*2}_{exp}}{R_4}\right) \quad (14)$$

and

$$T_{t4,exp} = \left(\frac{C^*_{exp}}{C^*_{th}}\right)^2 \cdot T_{t4,th} \quad (15)$$

and

$$T_{t4,exp} = \frac{\gamma}{2(\gamma+1)} \cdot \left(\frac{Isp^2_{exp}}{R_4}\right) \quad (16)$$

and

$$T_{t4,exp} = \left(\frac{Isp_{exp}}{Isp_{th}}\right)^2 \cdot T_{t4,th} \quad (17)$$

where R_4 is the gas constant as determined by the use of a CEC code.

The diagram provided in Figure 2 illustrates the relationship between the various data reduction methods. Each method for C* and Isp corresponds to a method to determine p_{t4}. The methods for $\eta_{\Delta T}$ use the four different methods to determine p_{t4} in each of the four different equations for $T_{t4,exp}$ resulting in 16 methods for $\eta_{\Delta T}$. The subscripts used in the uncertainty analysis section correspond to Figure 2 and are provided for the identification of specific data reduction methods for each performance parameter.

Uncertainty Analysis of Data Reduction Methods

In order to assess the uncertainty behavior associated with the different data reduction methods, an uncertainty analysis of a nominal case was performed. The nominal values of the case study used in this uncertainty analysis were taken from the case presented for example calculations in reference [3] and are presented in Table 1.

In this study, a general uncertainty analysis[7] was performed, and therefore, the uncertainties of the input variables are not considered separately in terms

of bias and precision uncertainty components. Consider the uncertainty of a result, r, of a data reduction method with J input variables x_i, such that

$$r = r(x_1, x_2, ..., x_J) \quad (18)$$

The overall uncertainty in r can be determined by

$$U_r = \left[\sum_{i=1}^{J}\left(\frac{\partial r}{\partial x_i}\right)^2 U^2_{x_i}\right]^{1/2} \quad (19)$$

where U_{x_i} is the uncertainty in the input variable x_i, and where the partial derivatives are sometimes referred to as "sensitivity coefficients." The interval $r \pm U_r$ contains the true (but unknown) value of r about 95 times out of 100.

An uncertainty analysis was performed considering the equations for C*, η_{C*}, Isp, η_{Isp} and $\eta_{\Delta T}$ to be of the form of Equation (18). The required sensitivity coefficients were numerically approximated by perturbing each input variable, in sequence, by 1% and determining the perturbed value of the result. This allowed determination of $\Delta r/\Delta x_i$ for each result and each input variable for the particular nominal values in this study. The PEP code was used to perform all CEC code runs.

The results of the study include the values of performance parameters determined using the different data reduction methods, sensitivity coefficients presented in the form of an "uncertainty magnification factor" (UMF), an uncertainty in r based on a 1% uncertainty in all input parameters, and an uncertainty in r based on "reasonable" estimates of uncertainties in input parameters.

The sensitivity coefficients are presented in the form of an "uncertainty magnification factor" (UMF) defined as

$$UMF = \frac{x_i}{r} \cdot \frac{\Delta r}{\Delta x_i} \quad (20)$$

where r represents the result (performance parameter) and x_i represents an input variable. The usefulness of the UMF value is that it illustrates the influence of the uncertainty in the input variable x_i as it propagates through the data reduction method into the result. If the magnification factor is less than 1, this indicates that the influence of the uncertainty in the input variable diminishes as the uncertainty is propagated to the result. If the UMF value is greater

than 1, the influence of the uncertainty of the input variable is magnified as it is propagated to the result (a one percent uncertainty in the input variable accounts for greater than 1% uncertainty in the final result). In this study, all UMF values are presented as positive numbers. Since the overall uncertainty equation (Equation (19)) uses the square of the sensitivity coefficient, sign has no impact on the propagation of uncertainty to the result for the general uncertainty analysis considered in this case.

The results of the uncertainty analysis are summarized in Tables 2-6. Each table corresponds to a specific performance parameter and affords evaluation of the different methods used in the determination of the performance parameter. In the upper row of values in these tables, the calculated values for the performance parameter are given illustrating the range of values that can be attained by simply using the different methods. The UMF values fill the body of the tables and can be cross-referenced to the input variable and the performance parameter method to which they apply.

Also included in the tables of the uncertainty analysis are three uncertainty values for the result. The uncertainty value designated by Ur(1%) is an uncertainty value for the result based on an assumed 1 percent uncertainty in all of the input variables. The other uncertainty values presented are based on reasonable estimates for the overall uncertainty in the input variables for the cases of a liquid fuel ramjet and a ducted rocket engine and are designated by Ur(LFR) and Ur(DRE), respectively. The estimated uncertainties in the input variables are shown in Table 7. The only difference in estimates of the uncertainties of the input variables is the estimated uncertainty in the enthalpy of formation of the fuel. The larger uncertainty estimate for the ducted rocket engine case is due to the range of values reported for the enthalpies of formation for gas generator fuel formulations. For example, for fuels based on glycidyl azide polymers reported values that vary by up to ±50 kcal/kg.

Figures 3 through 7 show a graphical summary of the results of this study. The uncertainties used to construct the uncertainty bands were the Ur(LFR) values presented in Tables 2 through 6.

The case study presented in this paper represents that of a ramjet under a single set of nominal operating conditions. The results of the uncertainty analysis presented in this case do not necessarily indicate the behavior of the uncertainty under different regimes of operating conditions. Furthermore, the uncertainty assessment of data reduction methodologies in this study did not consider uncertainties based on assumptions in the different methods or in the internal computations of the CEC codes (such as γ, c_5, R_4, etc.).

Summary and Conclusions

There exist numerous data reduction methods for performance determination of ramjet connected-pipe testing. Identified in this study are 4 distinct methods for C*, 4 distinct methods for Isp, and 16 distinct methods for thermal efficiency ($\eta_{\Delta T}$). The results in Figures 3-7 indicate that the methods of determination of $\eta_{\Delta T}$ produce a larger range of values than do the methods for determining the other performance parameters and that $\eta_{\Delta T}$ has the largest uncertainty of all of the performance parameters. It should be noted that the other efficiency performance parameters (η_{C*} and η_{Isp}) are limited to a range of values that cannot approach a lower limit near zero since the air flow in the combustor always produces values of C* and Isp that do not approach zero. Therefore, while the uncertainties of η_{C*} and η_{Isp} for the sample case in this study are lower than that of $\eta_{\Delta T}$, the resolution of reasonable values of η_{C*} and η_{Isp} is less than that of reasonable values of $\eta_{\Delta T}$.

The data reduction methods reviewed in this study can be divided into the categories of thrust-based calculations and non-thrust calculations as shown in Figure 2. The uncertainty values determined (subject to the assumed uncertainties in the input variable) showed that the thrust based methods typically provided results with lower values of uncertainty than the non thrust calculations. This conclusion is particularly true for the $\eta_{\Delta T}$ values in Table 6.

The different uncertainty calculations for the liquid fuel ramjet and ducted rocket case illustrate the insensitivity of the result uncertainty to the uncertainty in the fuel enthalpy of formation for the case study (a result that is not intuitively obvious). This can also be illustrated by the UMF values in the table for the fuel enthalpy of formation. The UMF values provide insight to which parameters will influence the overall uncertainty of the result the most. This can be viewed as an indication of where to focus efforts to decrease or minimize the input variable uncertainty such that the result uncertainty may be decreased.

References

[1]Timnat, Y. M., "Recent Developments in Ramjets, Ducted Rockets and Scramjets," Prog. of Aerospace Sci., Vol. 27, 1990, pp. 201-235.

[2]Dunsworth, L. C. and Reed, G. J., "Ramjet Engine Testing and Simulation Techniques," Journal of Spacecraft and Rockets, Vol. 16, No. 6, pp. 382-388, 1979.

[3]AGARD Advisory Report 323, *Experimental and Analytical Methods for the Determination of Connected-Pipe Ramjet and Ducted Rocket Internal Performance*, August, 1994

[4]McBride, B. J., *Computer Program for Calculation of Complex Chemical Equilibrium Compositions, Rocket Performance, Incident and Reflected Shocks, and Chapman-Jouguet Detonations*, NASA-SP-273, Revision July 15, 1986.

[5]McBride, B. J., *CET89 - Chemical Equilibrium with Transport Properties*, Lewis Research Center, 1989.

[6]Cruise, D. R., *Theoretical Computations of Equilibrium Compositions, Thermodynamic Properties, and Performance Characteristics of Propellant Systems*, Naval Weapons Center, China Lake, CA, April 1979, NWC-TM-5164.

[7]Coleman, H. W. and Steele, W. G., *Experimentation and Uncertainty Analysis for Engineers*, John Wiley & Sons, 1989.

Table 1. Nominal Values for Case Study

Input Variable	Nominal Value
$\dot{m}_{air}$ (air flow rate)	6.692 kg/s
$\dot{m}_{fuel}$ (fuel flow rate)	0.311 kg/s
p_4 (static press. at station 4)	568800 Pa
p_2 (static press. at station 2)	650200 Pa
P_{base} (nozzle base pressure)	78065 Pa
P_{amb} (ambient pressure)	101300 Pa
T_{t2} (total temp. at station 2)	606 K
H_{fuel} (fuel enthalpy of formation)	-482 kcal/kg
A_4 (combustor exit area)	0.022698 m^2
A_5 (nozzle throat diameter)	0.012668 m^2
A_{base} (nozzle base area)	0.004304 m^2
CD_5 (nozzle discharge coef.)	1.0
F_{LC} (load cell measurement)	13400 N
F_{PL} (preload measurement)	5000 N

Table 2. UMF values for C*

Input Variables	C*(m/s)	METHOD			
		1	2	3	4
		1112	1110	1119	1137
$\dot{m}_{air}$		0.95	0.94	0.95	0.68
$\dot{m}_{fuel}$		0.04	0.05	0.03	0.35
p_4		0.98	1.00	0.01	0.37
p_2		0.00	0.00	0.00	0.00
p_{base}		0.00	0.00	0.03	0.02
p_{amb}		0.00	0.00	0.18	0.18
T_{t2}		0.00	0.00	0.00	0.05
H_{fuel}		0.00	0.00	0.01	0.00
A_4		0.33	0.00	0.01	0.14
A_5		1.16	1.44	0.13	0.29
A_{base}		0.00	0.00	0.01	0.01
CD_5		1.00	1.00	0.45	1.00
F_{LC}		0.00	0.00	1.37	1.37
F_{PL}		0.00	0.00	0.51	0.51
Ur(1%) (%)		2.1	2.2	1.8	2.0
Ur(LFR) (%)		2.0	2.1	1.2	1.5
Ur(DRE) (%)		2.0	2.1	1.2	1.5

Table 4. UMF values for Isp

Input Variables	Isp(Ns/kg)	METHOD			
		1	2	3	4
		1389	1387	1397	1419
$\dot{m}_{air}$		0.94	0.94	0.95	0.67
$\dot{m}_{fuel}$		0.05	0.06	0.04	0.34
p_4		0.97	0.99	0.00	0.38
p_2		0.00	0.00	0.00	0.00
p_{base}		0.01	0.01	0.03	0.02
p_{amb}		0.00	0.00	0.18	0.18
T_{t2}		0.00	0.00	0.00	0.04
H_{fuel}		0.01	0.01	0.00	0.00
A_4		0.33	0.01	0.00	0.13
A_5		1.16	1.44	0.13	0.29
A_{base}		0.00	0.00	0.01	0.01
CD_5		0.56	0.56	0.00	0.56
F_{LC}		0.00	0.00	1.37	1.37
F_{PL}		0.00	0.00	0.51	0.51
Ur(1%) (%)		1.9	2.1	1.8	1.8
Ur(LFR) (%)		1.8	1.9	1.1	1.2
Ur(DRE) (%)		1.8	2.0	1.1	1.2

Table 3. UMF values for η_{C*}

Input Variables	η_{C*} (%)	METHOD			
		1	2	3	4
		95.1	94.9	95.6	97.1
$\dot{m}_{air}$		0.67	0.66	0.67	0.40
$\dot{m}_{fuel}$		0.57	0.58	0.56	0.18
p_4		0.96	0.98	0.01	0.39
p_2		0.00	0.00	0.00	0.00
p_{base}		0.02	0.02	0.05	0.04
p_{amb}		0.00	0.00	0.18	0.18
T_{t2}		0.10	0.10	0.10	0.06
H_{fuel}		0.00	0.00	0.01	0.00
A_4		0.34	0.02	0.01	0.12
A_5		1.16	1.44	0.13	0.29
A_{base}		0.00	0.00	0.01	0.01
CD_5		0.00	0.00	0.56	0.00
F_{LC}		0.00	0.00	1.37	1.37
F_{PL}		0.00	0.00	0.51	0.51
Ur(1%) (%)		1.8	2.0	1.8	1.6
Ur(LFR) (%)		1.6	1.8	1.2	1.0
Ur(DRE) (%)		1.6	1.8	1.2	1.0

Table 5. UMF values for η_{Isp}

Input Variables	η_{Isp} (%)	METHOD			
		1	2	3	4
		96.6	96.4	97.1	98.7
$\dot{m}_{air}$		0.39	0.39	0.40	0.12
$\dot{m}_{fuel}$		0.19	0.19	0.18	0.20
p_4		0.58	0.60	0.39	0.76
p_2		0.00	0.00	0.00	0.00
p_{base}		0.01	0.01	0.04	0.02
p_{amb}		0.00	0.00	0.18	0.18
T_{t2}		0.06	0.06	0.06	0.02
H_{fuel}		0.00	0.01	0.00	0.00
A_4		0.21	0.11	0.12	0.25
A_5		0.73	1.01	0.29	0.72
A_{base}		0.00	0.00	0.01	0.01
CD_5		0.56	0.56	0.00	0.56
F_{LC}		0.00	0.00	1.37	1.37
F_{PL}		0.00	0.00	0.51	0.51
Ur(1%) (%)		1.2	1.4	1.6	1.9
Ur(LFR) (%)		1.1	1.3	1.0	1.4
Ur(DRE) (%)		1.1	1.3	1.0	1.4

Table 6. UMF values for $\eta_{\Delta T}$

C* Methods	METHOD							
Input Variables $\eta_{\Delta T}$ (%)	1,1	1,2	1,3	1,4	2,1	2,2	2,3	2,4
	86.4	85.9	87.8	91.9	86.4	85.9	87.8	92.0
$\dot{m}_{air}$	1.99	1.99	1.99	1.16	2.01	2.01	2.01	1.17
$\dot{m}_{fuel}$	0.98	1.00	0.95	0.16	1.65	1.66	1.62	0.50
p_4	2.86	2.93	0.03	1.11	2.85	2.92	0.03	1.12
p_2	0.00	0.00	0.00	0.00	0.00	0.00	0.00	0.00
p_{base}	0.04	0.05	0.13	0.09	0.05	0.06	0.14	0.10
p_{amb}	0.00	0.00	0.52	0.51	0.00	0.00	0.52	0.51
T_{t2}	0.37	0.38	0.36	0.21	0.36	0.36	0.34	0.20
H_{fuel}	0.01	0.00	0.02	0.02	0.00	0.01	0.01	0.01
A_4	1.01	0.06	0.03	0.35	1.01	0.06	0.03	0.35
A_5	3.47	4.31	0.39	0.85	3.47	4.31	0.39	0.85
A_{base}	0.00	0.00	0.03	0.03	0.00	0.00	0.03	0.03
CD_5	2.95	2.95	1.31	2.89	0.00	0.00	1.65	0.00
F_{LC}	0.00	0.00	4.06	4.00	0.00	0.00	4.06	4.0
F_{PL}	0.00	0.00	1.50	1048	0.00	0.00	1.50	1.48
Ur(1%) (%)	5.9	6.4	5.1	5.5	5.3	5.8	5.4	4.7
Ur(LFR) (%)	5.7	6.1	3.2	4.1	4.9	5.3	3.4	2.9
Ur(DRE) (%)	5.7	6.1	3.2	4.1	4.9	5.3	3.4	2.9

Isp Methods	METHOD							
Input Variables $\eta_{\Delta T}$ (%)	3,1	3,2	3,3	3,4	4,1	4,2	4,3	4,4
	86.4	85.9	87.8	91.9	90.6	90.0	92.0	96.3
$\dot{m}_{air}$	1.99	1.99	1.99	1.16	1.17	1.16	1.17	0.35
$\dot{m}_{fuel}$	0.98	1.00	0.95	0.16	0.53	0.54	0.50	0.59
p_4	2.86	2.93	0.03	1.11	1.70	1.76	1.12	2.17
p_2	0.00	0.00	0.00	0.00	0.00	0.00	0.00	0.00
p_{base}	0.04	0.05	0.13	0.09	0.02	0.03	0.10	0.07
p_{amb}	0.00	0.00	0.52	0.51	0.00	0.00	0.51	0.50
T_{t2}	0.37	0.38	0.36	0.21	0.21	0.22	0.20	0.06
H_{fuel}	0.01	0.00	0.02	0.02	0.01	0.02	0.01	0.00
A_4	1.01	0.06	0.03	0.35	0.62	0.32	0.35	0.71
A_5	3.47	4.31	0.39	0.85	2.15	2.97	0.85	2.05
A_{base}	0.00	0.00	0.03	0.03	0.00	0.00	0.03	0.03
CD_5	1.64	1.65	0.00	1.61	1.62	1.62	0.00	1.59
F_{LC}	0.00	0.00	4.06	4.00	0.00	0.00	4.00	3.95
F_{PL}	0.00	0.00	1.50	1.48	0.00	0.00	1.48	1.46
Ur(1%) (%)	5.4	5.9	4.9	5.0	3.5	4.0	4.7	5.5
Ur(LFR) (%)	5.1	5.6	2.9	3.3	3.3	3.8	2.9	4.1
Ur(DRE) (%)	5.1	5.6	3.0	3.3	3.3	3.8	2.9	4.1

8

Table 7. Estimated Uncertainties of Input Variables

Input Variable	Uncertainty, U_{x_i}	
	Liquid Fuel Ramjet	Ducted Rocket Engine
$\dot{m}_{air}$ (kg/s)	0.06	0.06
$\dot{m}_{fuel}$ (kg/s)	0.0016	0.0016
p_4 (Pa)	6900	6900
p_2 (Pa)	6900	6900
p_{base} (Pa)	1000	1000
p_{amb} (Pa)	500	500
T_{t2} (K)	5	5
H_{fuel} (kcal/kg)	5	50
A_4 (m^2)	0.000136	0.000136
A_5 (m^2)	0.00010134	0.00010134
A_{base} (m^2)	0.00005814	0.00005814
CD_5	0.01	0.01
F_{LC} (N)	67	67
F_{PL} (N)	25	25
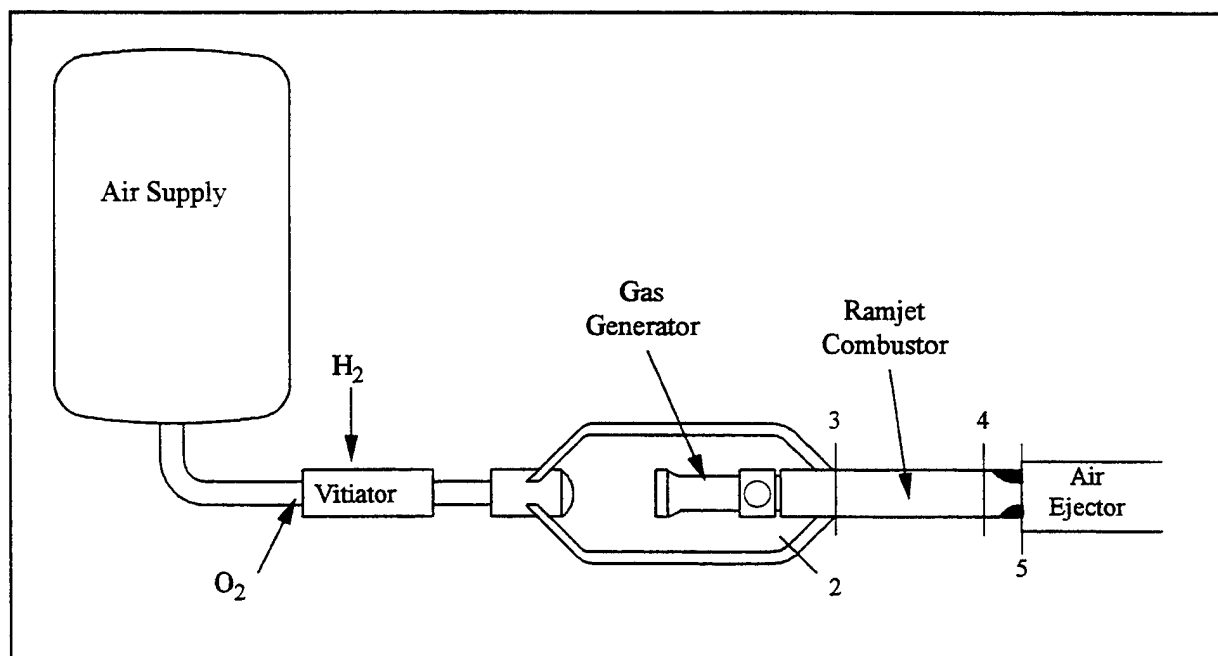
Figure 1. Schematic of Connected-Pipe Testing
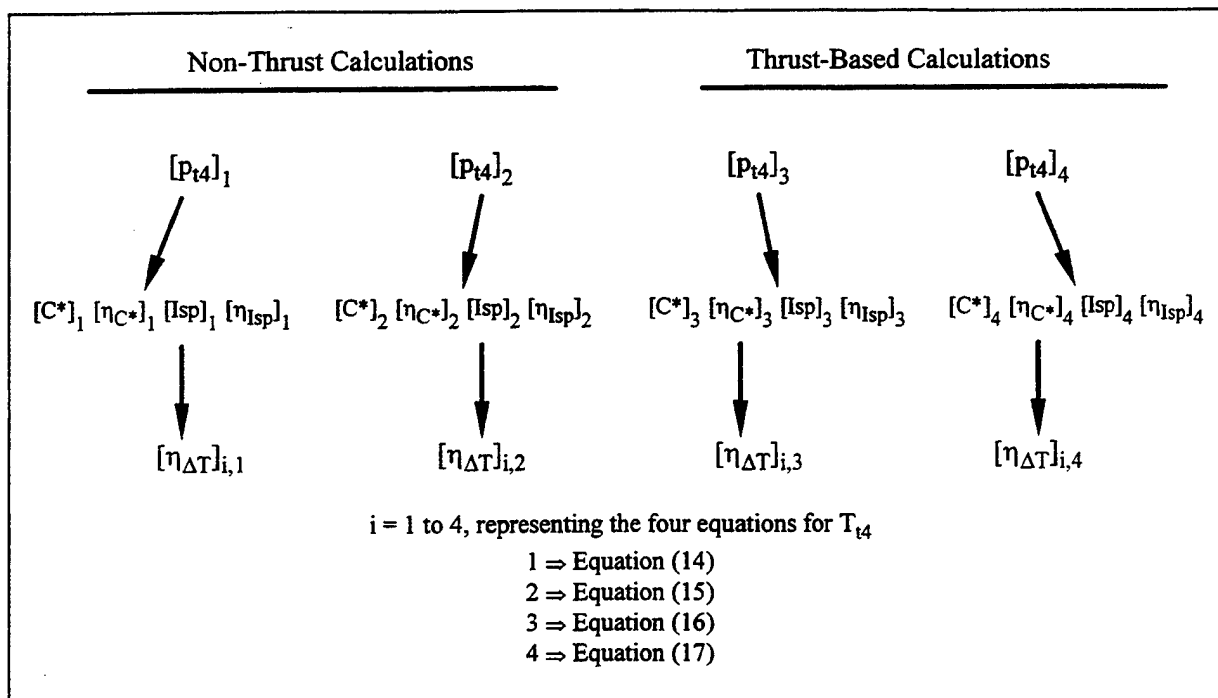
Figure 2. Relationship Between Data Reduction Methods
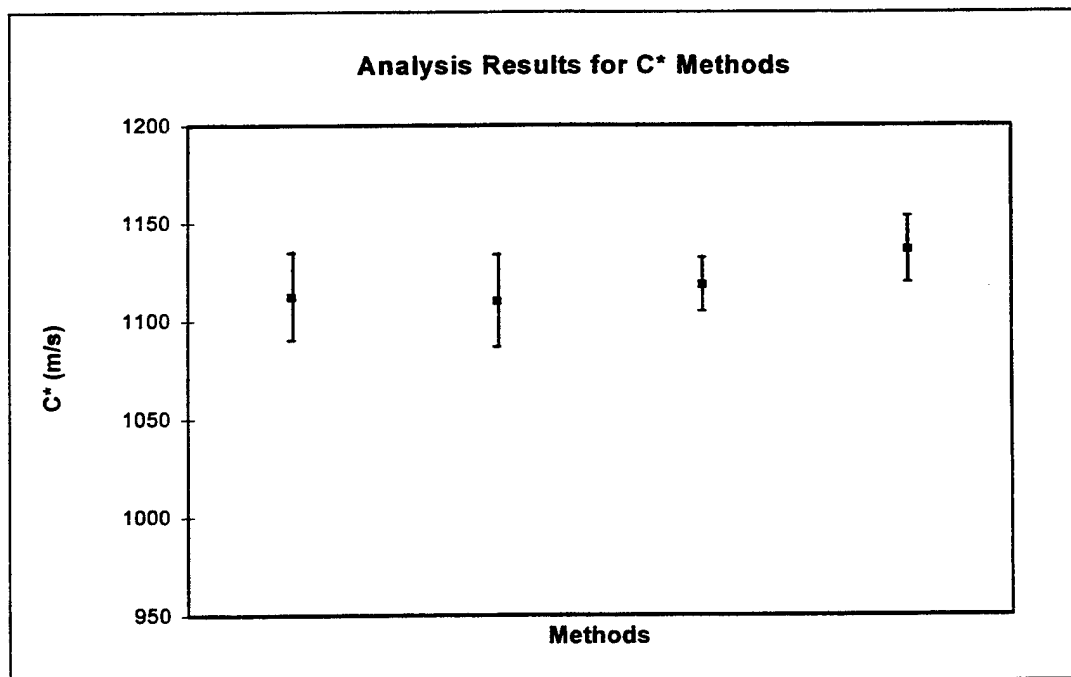
Figure 3. Results for C* Methods
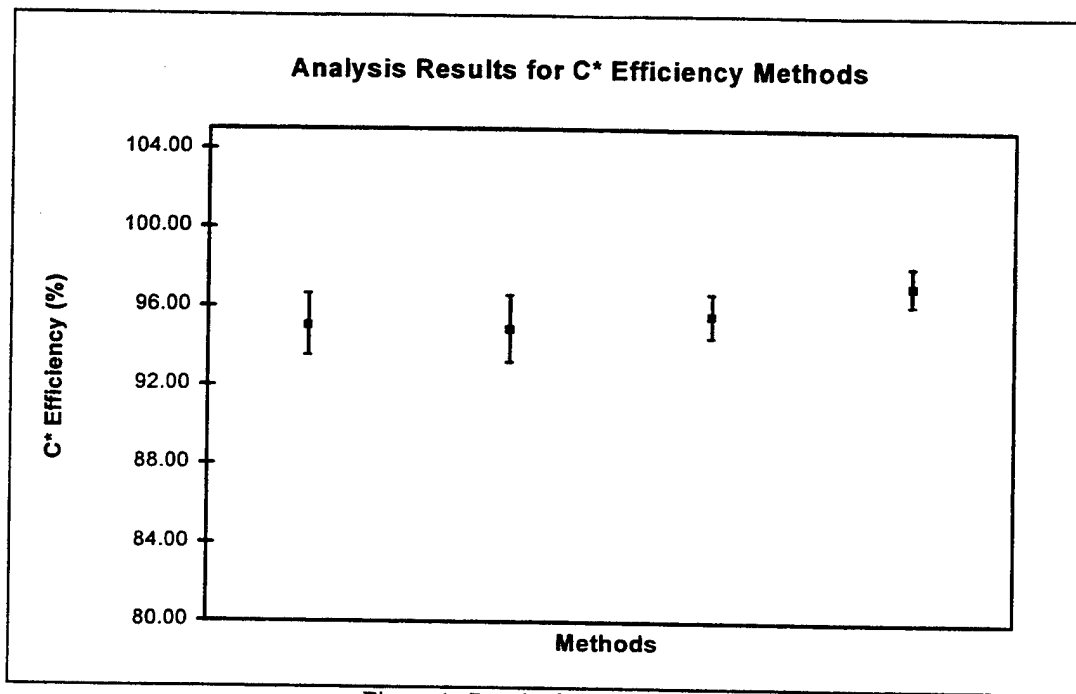
Figure 4. Results for η_{C*} Methods
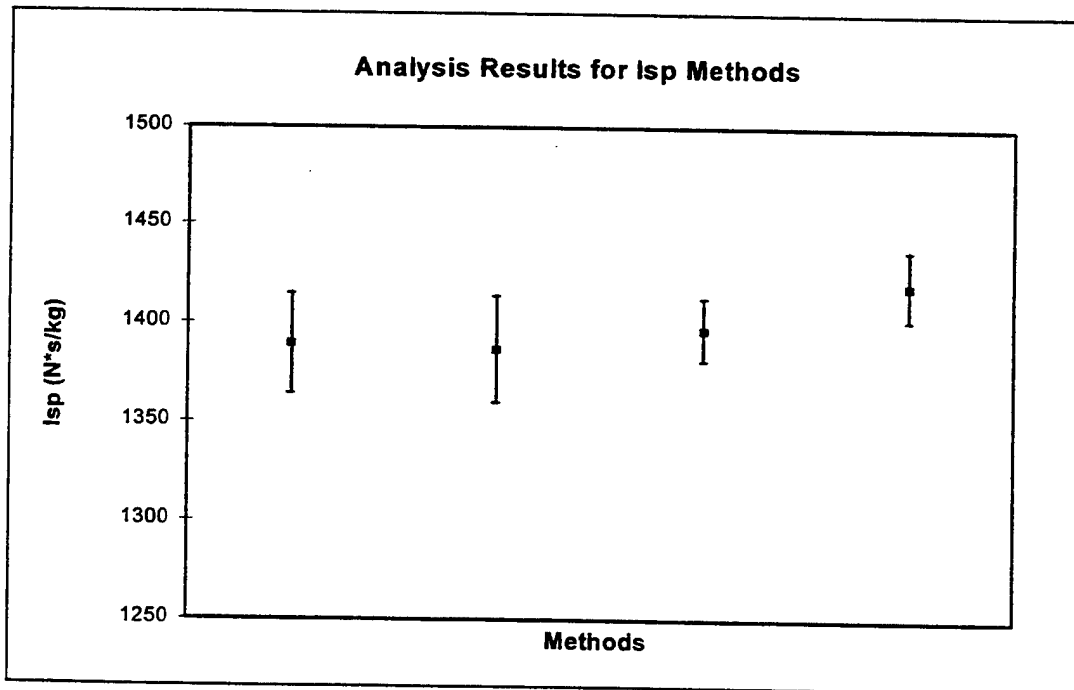
Figure 5. Results for Isp Methods

American Institute of Aeronautics and Astronautics

Analysis Results for Isp Efficiency Methods

Figure 6. Results for η_{Isp} Methods
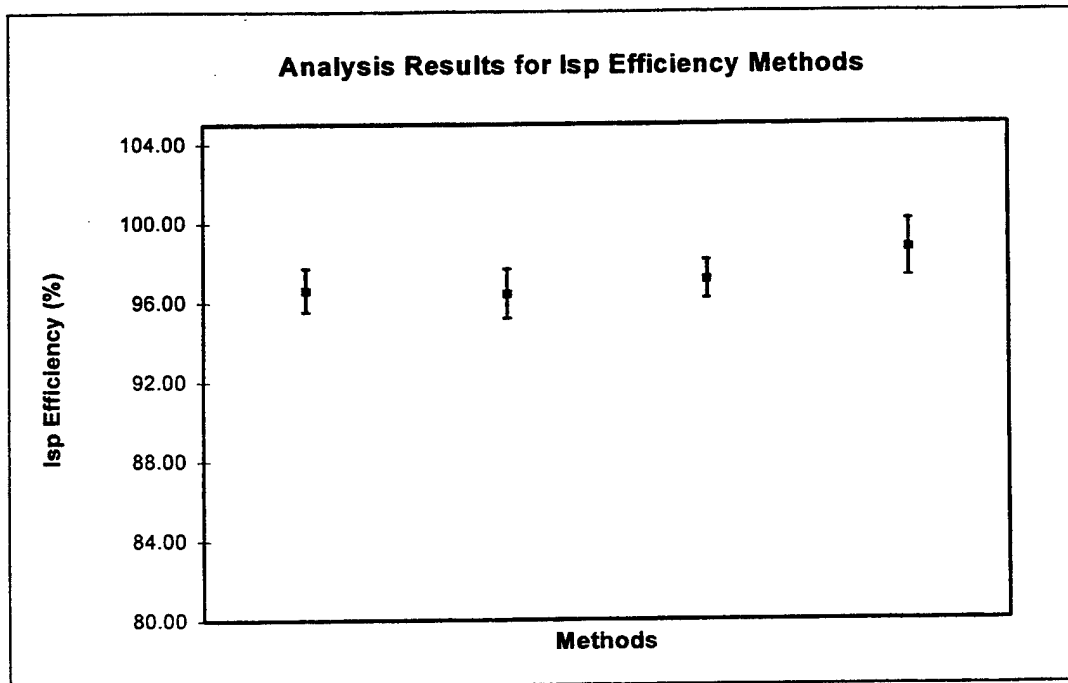
Analysis Results for Thermal Efficiency Methods

Figure 7. Results $\eta_{\Delta T}$

American Institute of Aeronautics and Astronautics
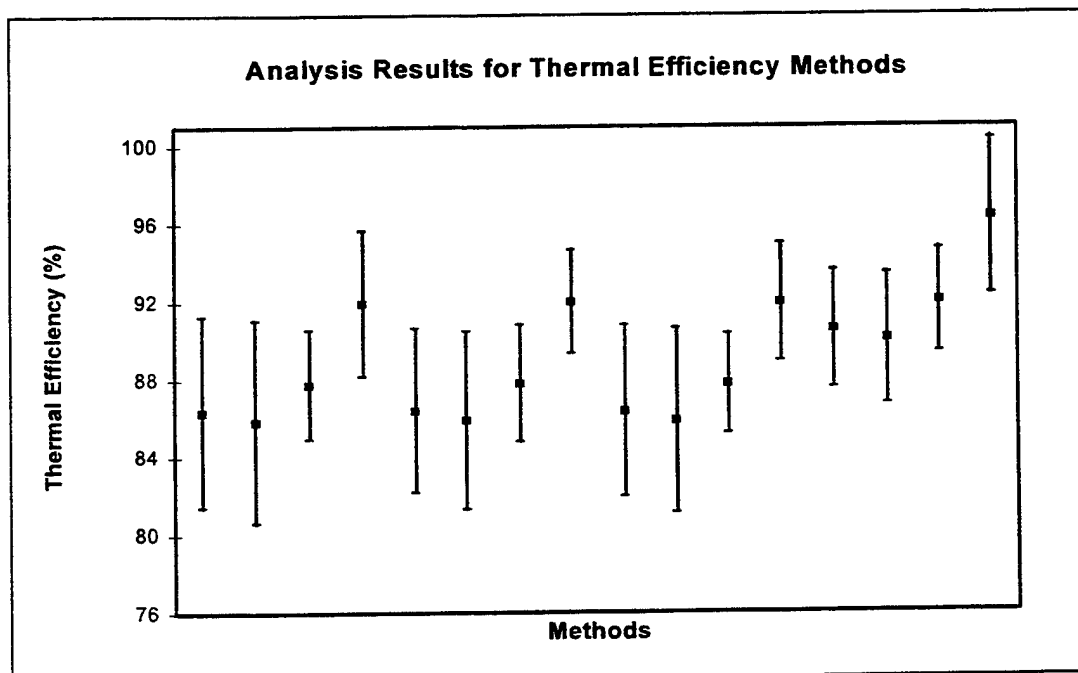
AIAA 95-2937

A Connected-Pipe Facility for the Evaluation of Ducted Rocket Propellants

John A. Blevins and Hugh W. Coleman
Propulsion Research Center
Department of Mechanical and Aerospace Engineering
University of Alabama in Huntsville
Huntsville, Alabama 35899

Robert Milton
Propulsion Directorate
U.S. Army Missile Command
Redstone Arsenal, Alabama 35898

and

Bobby G. Kirkham
Uwohali Inc.
Huntsville, Alabama 35805

31st AIAA/ASME/SAE/ASEE
Joint Propulsion Conference and Exhibit
July 10-12, 1995/San Diego, CA

A CONNECTED-PIPE FACILITY FOR THE EVALUATION OF DUCTED ROCKET PROPELLANTS

John A. Blevins[*] and Hugh W. Coleman[†]
Propulsion Research Center
Department of Mechanical and Aerospace Engineering
University of Alabama in Huntsville, Huntsville, AL 35899

Robert Milton[‡]
Propulsion Directorate
U.S. Army Missile Command
Redstone Arsenal, AL 35898

Bobby G. Kirkham[§]
Uwohali Inc.
Huntsville, AL 35805

Abstract

An experimental program evaluating ducted rocket engine propellant performance in a connected-pipe facility is underway. An overview of connected-pipe testing and the facility used in this study is presented. Sample test results from the current study are reported. Also, further modifications of the facility to enhance ramjet and ducted rocket research and development programs at the U.S. Army Missile Command are discussed.

Nomenclature

$m_{initial}$ Initial mass of gas generator

m_{final} Final mass of gas generator

P_g Gas generator pressure

t Time

Introduction

This article contains an overview of connected-pipe testing, the connected-pipe facility located at the Propulsion Directorate of the U.S.

---

[*]Graduate Research Assistant, Student Member AIAA

[†]Eminent Scholar in Propulsion and Professor, Senior Member AIAA

[‡]Project Engineer

[§]Test Engineer

Army Missile Command (MICOM), Redstone Arsenal, Alabama and sample test results of ducted rocket propellant development studies that are underway.

Connected-Pipe Testing

Connected-pipe testing is used for performance determination and fundamental combustion studies in ramjet and scramjet engines[1,2]. In connected-pipe testing, the air supply is connected directly to the ramjet combustor. Therefore, connected-pipe testing considers only the combustor performance and no aerodynamic or inlet effects. By considering only the ramjet combustor, the air supply requirement and equipment necessary for testing is minimized making connected-pipe testing the most cost-effective method for evaluation and development of ramjet engines prior to free jet and flight testing[2].

For the appropriate simulation of vehicle flight conditions, the air must be supplied at the stagnation temperatures and pressures that are to be encountered during flight. In order to supply the combustor with the high temperature air necessary to simulate the conditions produced by a supersonic compression inlet, a vitiated heater is used to increase the air temperature. A vitiated heater uses combustion of a fuel added to the air flow to increase the temperature. Also, oxygen replenishment is added to the flowfield to offset the consumption of oxygen by the combustion of the vitiator fuel. There exist two methods of oxygen replenishment: 1) make-up oxygen is added to account for the mass of oxygen consumed by the combustion of the vitiator fuel, and 2) make-up oxygen is added to preserve the

volumetric content of oxygen in the supply air. Both of these vitiator methods are discussed in reference [3]. By adding the fuel and makeup oxygen, the composition of the oxidizer supplied to the combustion chamber is no longer that of air because it includes combustion products from the vitiated heater. The composition can generally be considered to be all of the constituents (air, vitiator fuel, and makeup oxygen) at equilibrium at the static temperature and pressure of the inlets to the ramjet combustor.

Data reduction methods for performance determination in connected-pipe facilities vary and are the subject of recent studies[3,4].

Ducted Rockets

Ducted rockets are characterized by a fuel supply to the ramjet combustor from a fuel rich gas generator. Air is supplied through side inlets. A schematic of a generic ducted rocket is shown in Figure 1. In a ducted rocket, the rocket body is boosted to supersonic velocities by using a solid propellant. Upon completion of the boost phase, the inlets are blown open and a nozzle insert ejected allowing use of the boost phase combustion chamber to be the ramjet combustor.

MICOM's Connected-Pipe Facility

The connected-pipe facility located at the MICOM Propulsion Directorate has recently undergone a comprehensive renovation and is currently in use for the evaluation of ducted rocket gas generator fuels. MICOM's connected-pipe facility is a comprehensive air breathing combustion development tool affording the ability to perform ducted rocket fuel comparison studies and other ramjet testing including the ability to perform trajectory simulation runs. A schematic and a photograph of the facility are shown in Figures 2 and 3, respectively.

The facility utilizes a 500 cubic feet air storage system at a maximum pressure of 2500 psi for supply air which can be varied at flow rates up to 10 lbm/second. The large air capacity affords long run times exceeding 6 minutes in duration, even at the largest air flow rate.

The vitiated heater uses gaseous hydrogen as a fuel and can provide inlet temperatures up to 1500 Rankine at the maximum air flow rate of 10 lbm/second. The replenishment oxygen is added

upstream of the vitiated heater in order to promote more complete combustion in the vitiator.

A high pressure air ejector is used to provide subatmospheric exhaust pressure conditions. The high pressure air ejector allows the nozzle base pressure to be maintained at pressures as low as 4 psia.

The resulting flight simulation envelope expressed in terms of altitude and Mach number, based on the temperatures and air flow rates achievable by the facility is shown in Figure 4.

Propellant Comparison Studies

The initial test series for the evaluation of two proprietary candidate formulations of ducted rocket gas generator fuels has been completed and further testing and propellant evaluation studies are underway.

A representative sample of test results from a ducted rocket test is provided in Figures 5, 6, 7, 8, 9 and 10. These figures are from a test simulating conditions 2 kilometers altitude at a Mach number of 2.8. The figures related to propellant performance (gas generator pressure, ramburner pressure, and thrust) are presented without a scale, but are included to illustrate the stability of the gas generator and ramburner combustion during the ducted rocket/ramjet test run. The facility operation is shown in the remaining figures to illustrate the steady operation of the facility during test conditions.

The gas generator pressure profile relates directly to the mass flow rate of fuel in a ducted rocket by

$$\dot{m}_{fuel} = \frac{\left(m_{initial} - m_{final}\right) \cdot P_g(t)}{\int P_g(t)dt} \quad (1)$$

where $m_{initial}$ and m_{final} are the initial and final mass of the gas generator cartridge, $P_g(t)$ is the gas generator pressure at time t and the integral $\int P_g(t)dt$ is evaluated over the time interval of the gas generator burn. Equation (1) is valid assuming the flow is always choked and the characteristic exhaust velocity (C*) from the gas generator remains constant. Therefore, since the change in mass is a constant and the pressure-time integral produces a constant value, the flow rate curve has the same profile as the gas generator curve.

The performance of the ducted rocket burn is evaluated in the form of various performance

parameters such as characteristic exhaust velocity, (C*), specific impulse (Isp) and thermal efficiency (ηth). Due to the proprietary nature of this study, no such parameters are reported in this paper. A comprehensive list of performance parameters and methods of determination are included in references [3] and [4].

Future Facility Modifications and Studies

In order to support the current propellant studies and additional research topics, the connected-pipe facility will be modified by the addition of methane injection and optical diagnostics The methane injection system will provide the unique capability to inject a well known gaseous fuel into the ramjet combustor to evaluate the best case steadiness and repeatability of the facility. This will afford insight into further propellant comparison studies by providing a facility "calibration" of the steadiness of the facility during well known operating conditions and, therefore, the combustion unsteadiness due to gas generator propellant can be better characterized. Also, a comprehensive uncertainty analysis[5] of future experimental work will be aided by the facility history and repeatability information gained from methane testing.

Optical access ports for non-intrusive optical diagnostics to evaluate the reacting flowfield will also be added. The purpose of these studies will be to observe the reacting flow mixing that occurs in these complex combustors.

References

[1]Timnat, Y. M., "Recent Developments in Ramjets, Ducted Rockets and Scramjets," Prog. of Aerospace Sci., Vol. 27, 1990, pp. 201-235.

[2]Dunsworth, L. C. and Reed, G. J., "Ramjet Engine Testing and Simulation Techniques," Journal of Spacecraft and Rockets, Vol. 16, No. 6, pp. 382-388, 1979.

[3]AGARD Advisory Report 323, *Experimental and Analytical Methods for the Determination of Connected-Pipe Ramjet and Ducted Rocket Internal Performance*, August, 1994

[4]Blevins, J. and Coleman, H. W., "An Assessment of Connected-Pipe Ramjet Testing," AIAA 95-3074, 31st Joint Propulsion Conference, 1995.

[5]Coleman, H. W. and Steele, W. G., *Experimentation and Uncertainty Analysis for Engineers*, John Wiley & Sons, 1989.
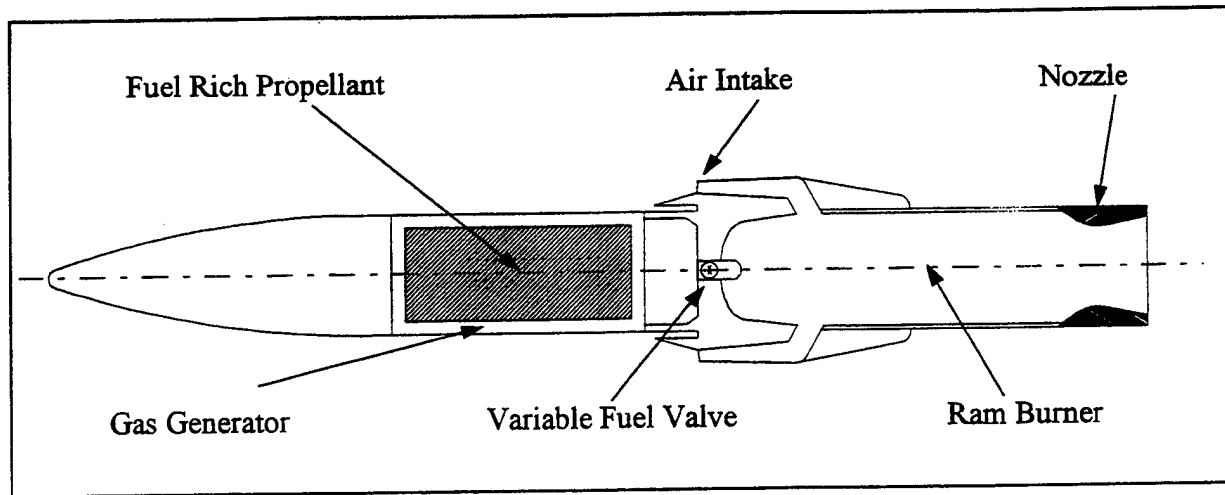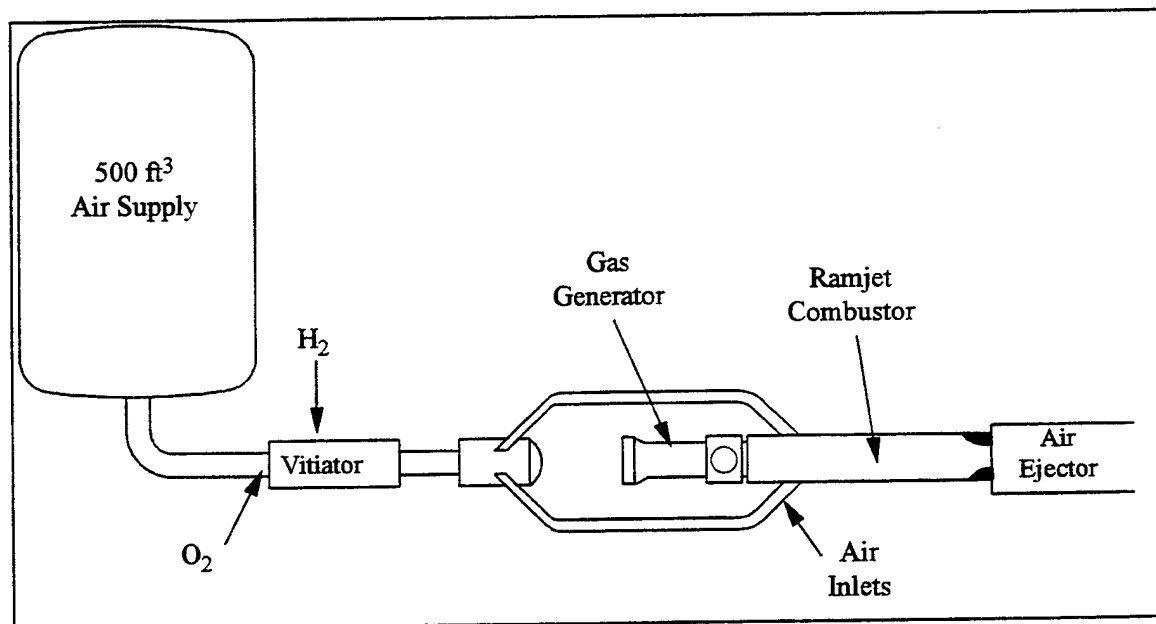
Figure 1. Typical Ducted Rocket Flight Vehicle

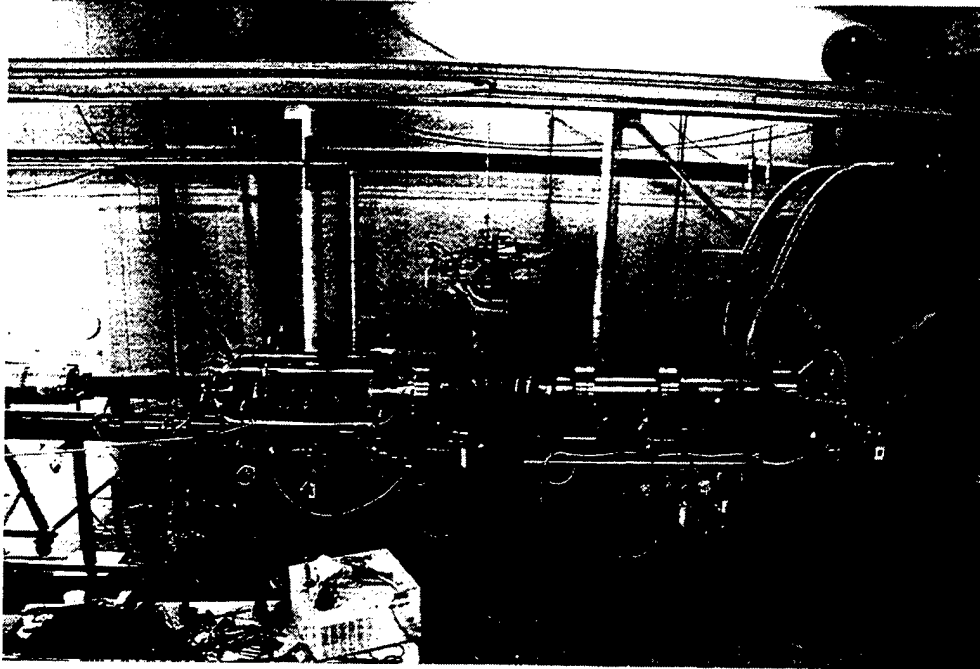Figure 2. MICOM Connected-Pipe Facility
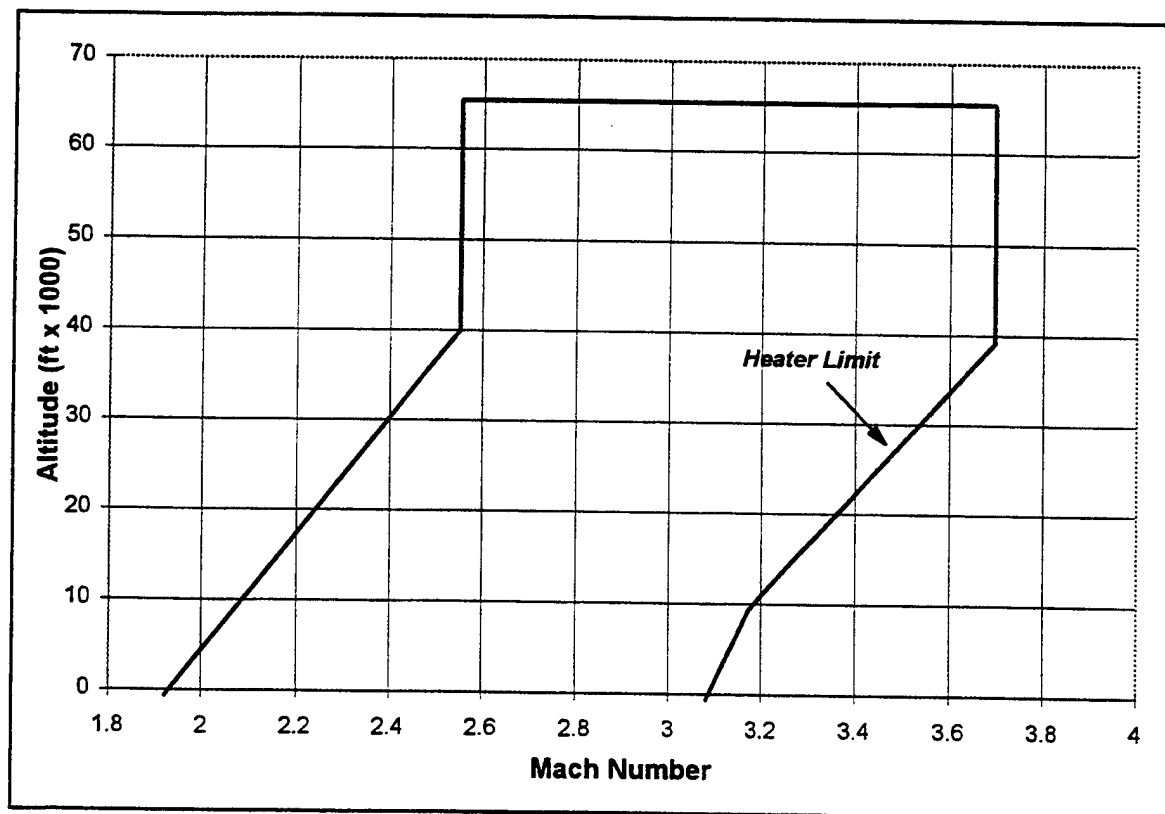
Figure 3. Photograph of MICOM Connected-Pipe Facility

Figure 4. Facility Flight Simulation Envelope

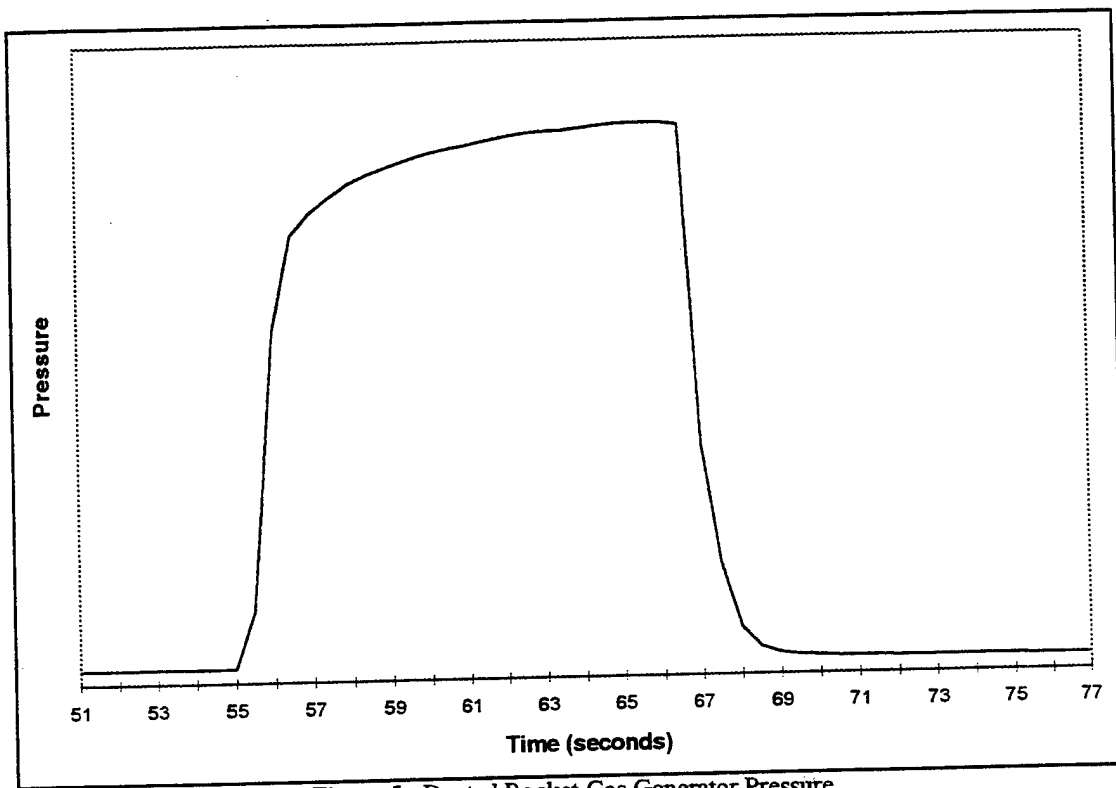American Institute of Aeronautics and Astronautics
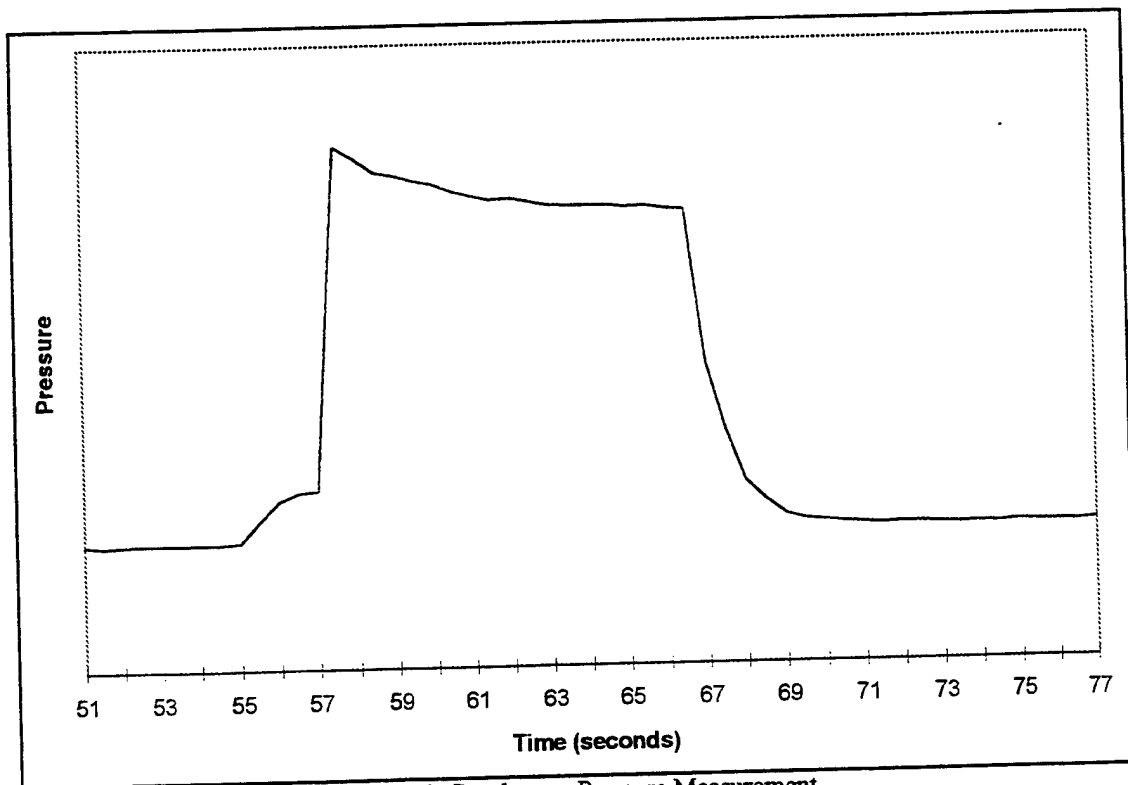
Figure 5. Ducted Rocket Gas Generator Pressure
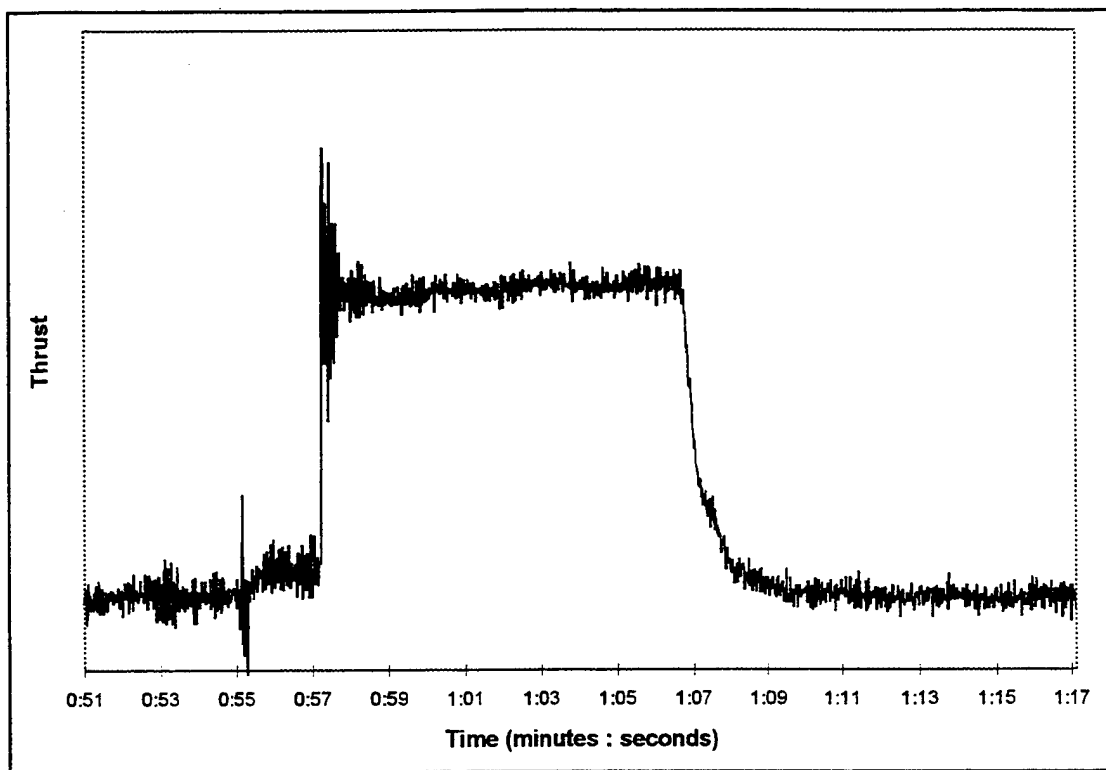

Figure 6. Ramburner Pressure Measurement
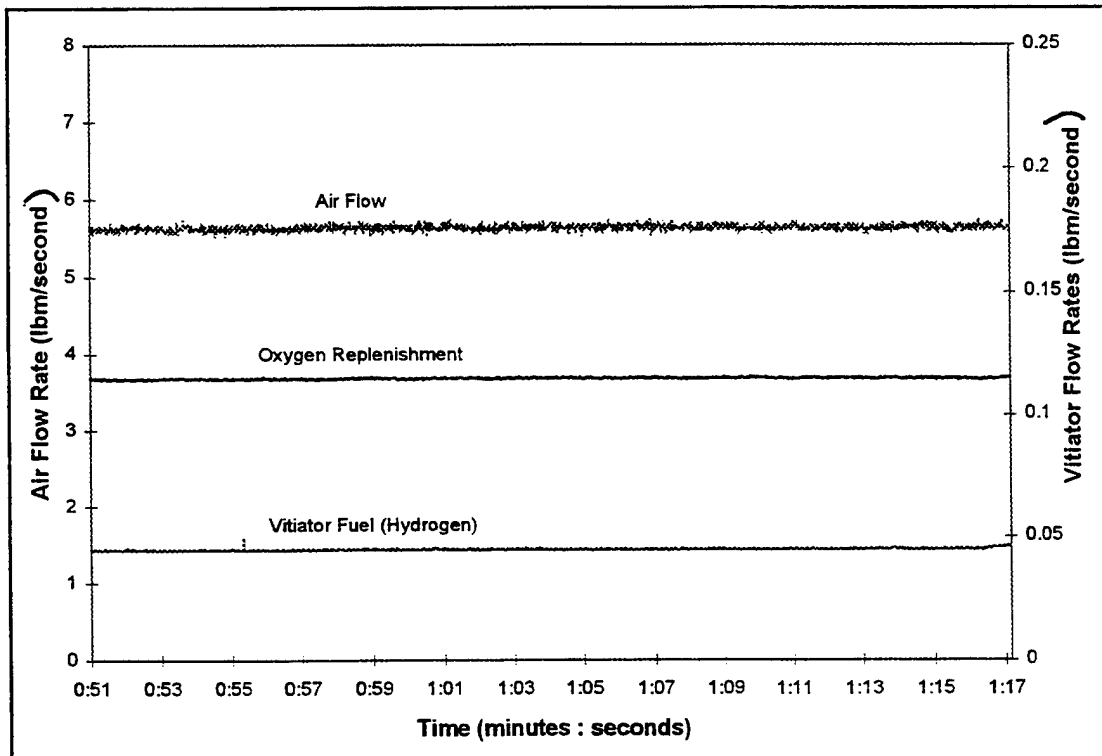
6

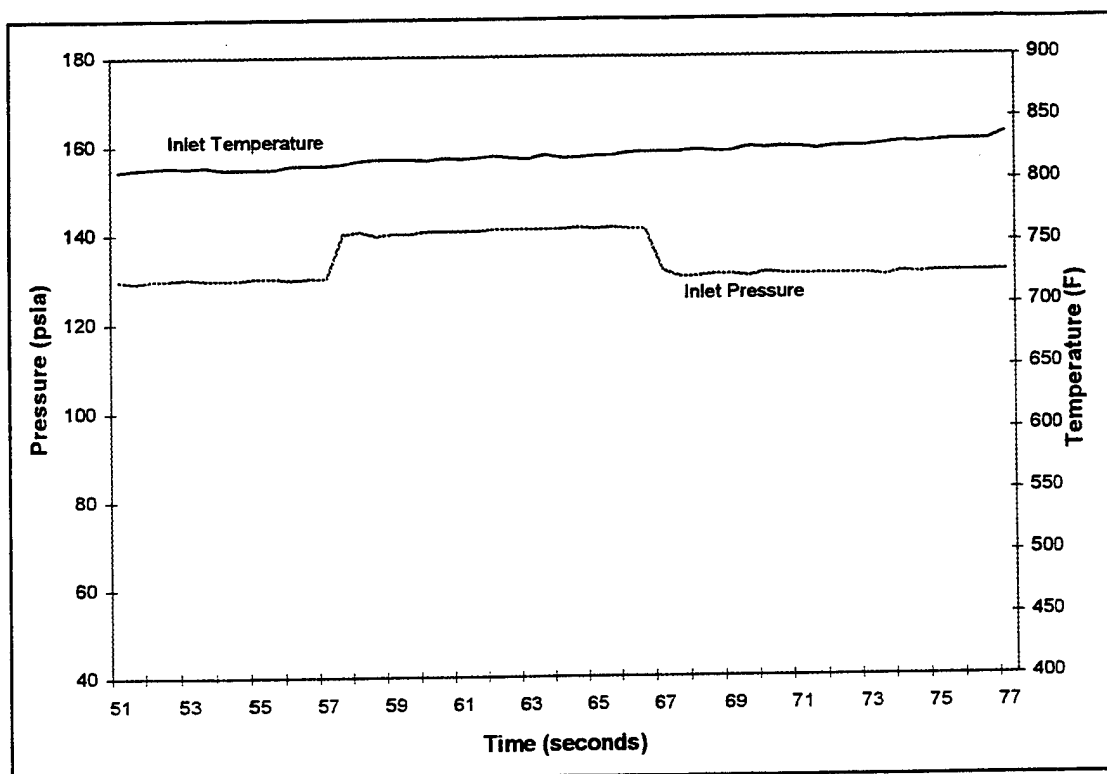Figure 7. Thrust Measurement

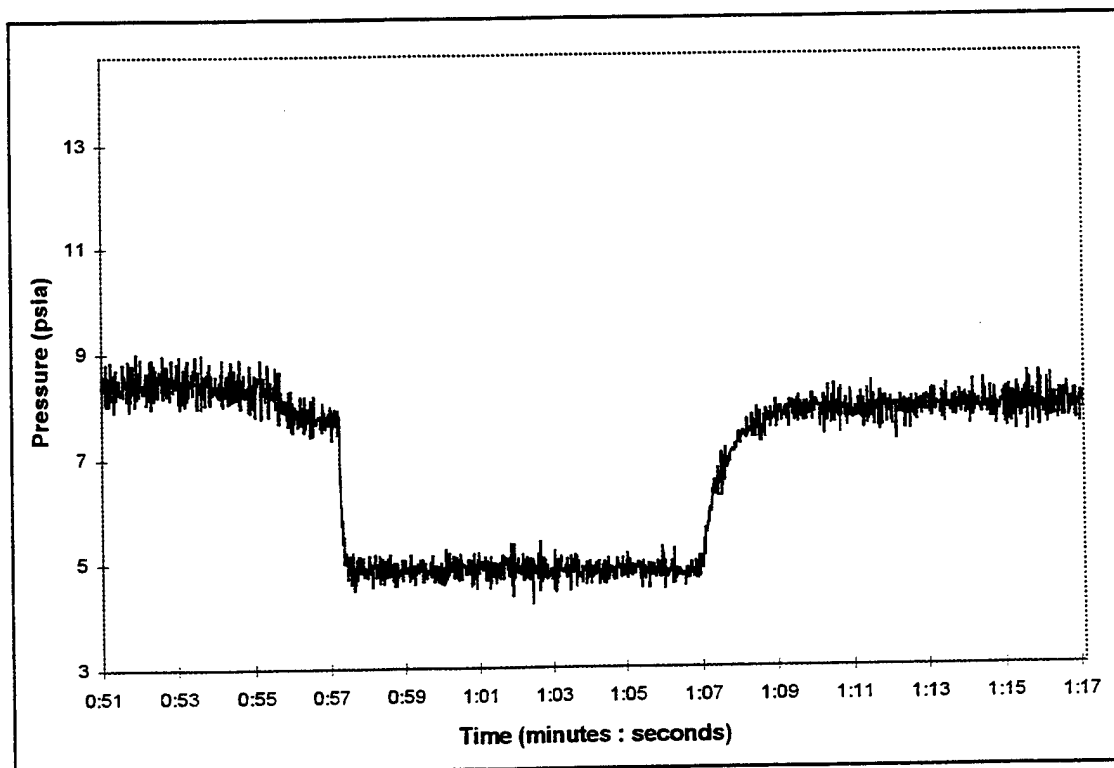Figure 8. Facility Flow Rates

Figure 9. Inlet Temperature and Pressure

Figure 10. Base Pressure Measurement

8

DEFENSE TECHNICAL INFORMATION CENTER
REQUEST FOR SCIENTIFIC AND TECHNICAL REPORTS

Title, *"Flow Visualization of Four-Inlet Ducted Rocket Engine Configurations"*

1. **Report Availability** *(Please check one box)*	2a. **Number of Copies Forwarded**	2b. **Forwarding Date**
☑ This report is available. *Complete sections 2a - 2f.* ☐ This report is not available. *Complete section 3.*	3	02 MAY 2000

2c. Distribution Statement *(Please check ONE box)*

DoD Directive 5230.24, "Distribution Statements on Technical Documents," 18 Mar 87, contains seven distribution statements, as described briefly below. Technical documents MUST be assigned a distribution statement.

☑ DISTRIBUTION STATEMENT A: Approved for public release. Distribution is unlimited.

☐ DISTRIBUTION STATEMENT B: Distribution authorized to U.S. Government Agencies only.

☐ DISTRIBUTION STATEMENT C: Distribution authorized to U.S. Government Agencies and their contractors.

☐ DISTRIBUTION STATEMENT D: Distribution authorized to U.S. Department of Defense (DoD) and U.S DoD contractors only.

☐ DISTRIBUTION STATEMENT E: Distribution authorized to U.S. Department of Defense (DoD) components only.

☐ DISTRIBUTION STATEMENT F: Further dissemination only as directed by the controlling DoD office indicated below or by higher authority.

☐ DISTRIBUTION STATEMENT X: Distribution authorized to U.S. Government agencies and private individuals or enterprises eligible to obtain export-controlled technical data in accordance with DoD Directive 5230.25, Withholding of Unclassified Technical Data from Public Disclosure, 6 Nov 84.

2d. Reason For the Above Distribution Statement *(in accordance with DoD Directive 5230.24)*

2e. **Controlling Office**	2f. **Date of Distribution Statement Determination**

3. This report is NOT forwarded for the following reasons. *(Please check appropriate box)*

☐ It was previously forwarded to DTIC on _____ *(date)* and the AD number is _____

☐ It will be published at a later date. Enter approximate date if known. _____

☐ In accordance with the provisions of DoD Directive 3200.12, the requested document is not supplied because:

_____

Print or Type Name Felecia Troupe	Signature *Per Phone/Conv 5-2-00* Joyce J Chias
Telephone 256-890-6000 Ext 229	*(For DTIC Use Only)* AQ Number M00-08-1886